NUREG/CR—4534
SAND86—0419
R3
Printed August 1987

Analysis of Diffusion Flame Tests

J. E. Shepherd

Prepared by
Sandia National Laboratories
Albuquerque, New Mexico 87185 and Livermore, California 94550
for the United States Department of Energy
under Contract DE-AC04-76DP00789

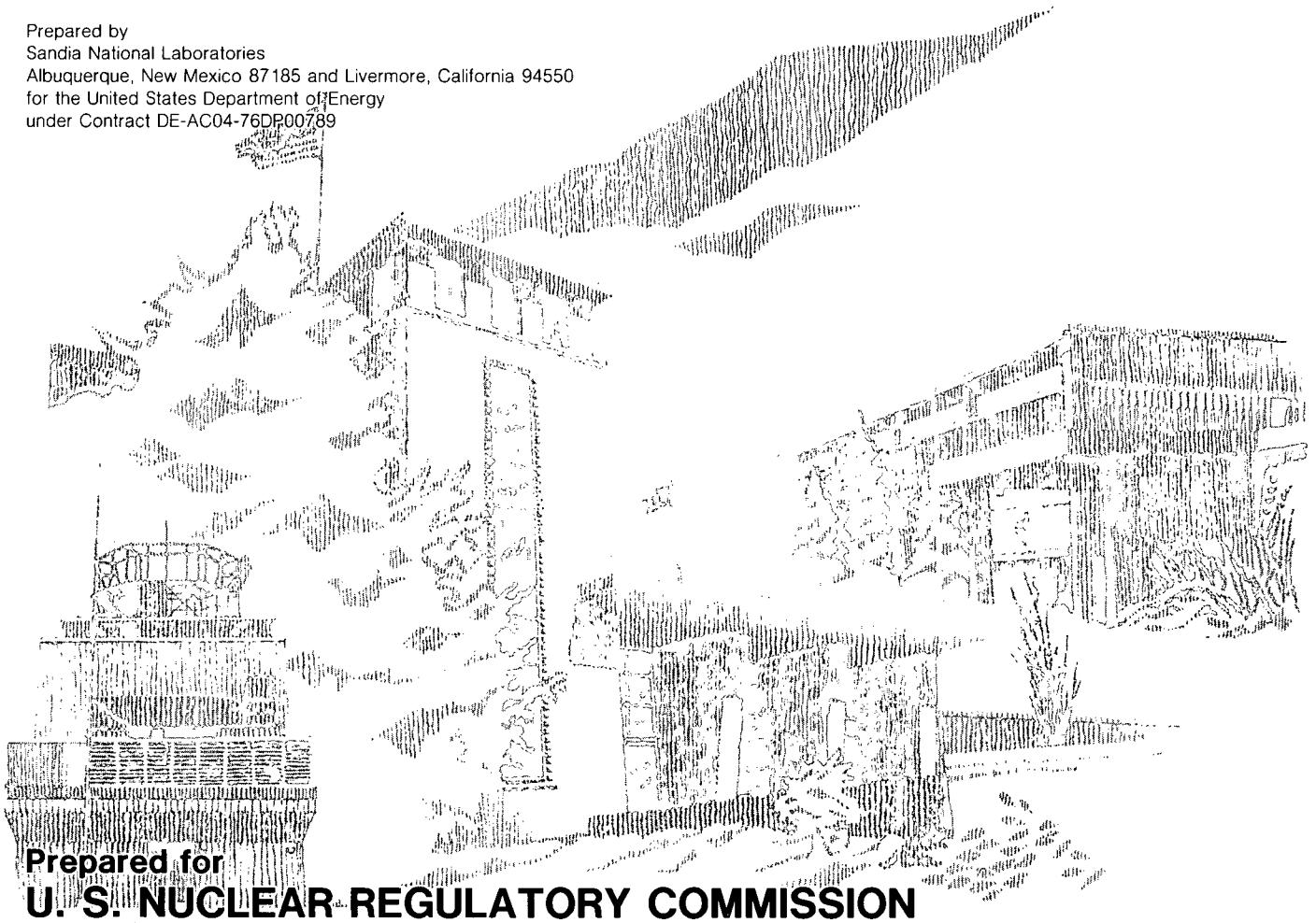

Prepared for
U. S. NUCLEAR REGULATORY COMMISSION

Available from

Superintendent of Documents
U.S. Government Printing Office
Post Office Box 37082
Washington, D.C. 20013-7082

and

National Technical Information Service
Springfield, VA 22161

NUREG/CR-4534
SAND86-0419
R3

ANALYSIS OF DIFFUSION FLAME TESTS

J. E. Shepherd
Printed August 1987

Sandia National Laboratories
Albuquerque, NM 87185
Operated by
Sandia Corporation
for the
U. S. Department of Energy

Prepared for
Division of Reactor Accident Analysis
and
Division of Engineering
Office of Nuclear Regulatory Research
U.S. Nuclear Regulatory Commission
Washington, DC 20555
Under Memorandum of Understanding DOE 40-550-75
NRC FIN Nos. A1246, A1336

Abstract

This report discusses the results and analysis of hydrogen diffusion flame tests conducted at the Nevada Test Site by EPRI and the U. S. NRC. Those tests were designed to simulate the effects of hydrogen combustion inside a nuclear power plant containment following a degraded–core accident. Test initial conditions and sample data plots are given for 16 tests. Mixing and ignition phenomena are discussed in terms of the source parameters and igniter location. A simple model is developed for simulating the heat transfer and computing convective heat transfer coefficients from experimental pressure measurements. Convective heat transfer coefficients are reported for four tests. The effect of stagnation–point heat transfer is estimated.

Contents

List of Figures

List of Tables

Acknowledgment

I would like to thank the personnel of EG&G, particularly Richard Thompson, for their cooperation and for providing an atmosphere that made Sandia participation in these tests successful. O. B. Crump, Jr. (Sandia) was responsible for constructing and installing the Sandia instrumentation in the dewar. Art Ratzel (Sandia) undertook the massive task of organizing and analyzing the data from the premixed tests. Loren Thompson (EPRI) was the program manager and driving force that made the test plan a reality. Jack Haugh (EPRI) has performed the difficult task of completing the analysis and test documentation. Sandia participation was supported by the U. S. NRC Hydrogen Behavior and Mitigation and Prevention research programs; John Larkins (NRC) and Pat Worthington (NRC) were program managers.

Dedication

To the memory of Loren Thompson.

Executive Summary

This report discusses some results and a partial analysis of the diffusion flame tests conducted at the Nevada Test Site by EPRI and the U. S. NRC. Those tests were designed to simulate the effects of hydrogen combustion inside a nuclear power plant containment following a degraded–core accident. Testing was performed during the years 1983–1984 inside a spherical vessel (an abandoned liquid hydrogen dewar) that was 2048 m^3 in volume.

16 tests were performed, 4 tests have been extensively analyzed, 4 more have been examined briefly and the remaining 8 are either not suitable for analysis or insufficient data were available. For the 4 tests that were extensively analyzed, gas pressure, temperature and wall heat flux measurements are presented. Only gas pressure measurements are provided for the other tests.

Mixing and ignition processes have been examined as a function of source parameters and igniter locations. The source Froude number has a profound influence on the degree of mixing during the injection process. The lack of multiple deflagrations and the phenomena of nonignition can be explained on this basis. Tests using a buoyant plume source (low source Froude number) probably have a strongly stratified initial hydrogen concentration and a distinct moving front between mixed and unmixed fluid. As the source Froude number increases, the vessel contents become better mixed. Tests using jet–like sources (large source Froude numbers) will exhibit good mixing and a distinct front will not form.

A control–volume thermodynamic model is used to simulate the tests and also to infer the convective heat transfer coefficients from the measured gas pressures. For tests in which the gas is well stirred, the control volume model yields good agreement with all measurements except wall temperature. Stratification in the vessel atmosphere and stagnation–point heat transfer are examined as possible effects that can explain the nonuniform vessel wall temperatures.

1 Introduction

This report documents some test results and a partial analysis of the continuous injection (CI) or diffusion flame portion of the hydrogen combustion tests performed at Test Cell "C" of the DOE's Nevada Test Site (NTS). These tests were carried out in 1983-84 as part of a program jointly sponsored by the Electric Power Research Institute (EPRI) and the U. S. Nuclear Regulatory Commission (NRC). The program was designed to study hydrogen-air-steam combustion in a large-scale facility under conditions postulated to occur during hypothetical degraded-core accidents in nuclear power plants. The test program and results are described in detail by Thompson *et al.*[1]

Two types of tests were performed. Both were carried out inside a spherical vessel (an abandoned liquid hydrogen dewar) that was 2048 m^3 in volume. The dewar was modified for H_2 and steam injection, water sprays, and an air–purge system. Instrumentation was installed throughout the dewar and four IR-sensitive video cameras were used to observe the combustion events. Gas pressure, gas temperature, wall temperatures, and heat fluxes were recorded as a function of time by a digital data acquisition system. The dewar modifications, instrumentation and test operations were performed by personnel of EG&G, Las Vegas.

A series of 24 separate deflagration tests were performed in which mixtures containing 6-13% H_2, 0-40% steam, and the remainder air were ignited by glowplugs. These tests and the associated analysis performed by Sandia National Laboratories, Albuquerque (SNLA) are described in Ref. 2. Readers interested in a more in–depth discussion of the experiment and instrumentation should consult that report and Ref. 1. The terminology used in the present report is identical to that used in Refs. 1 and 2 for the labeling of instruments and location of key equipment.

Another 16 tests were performed in which a H_2-steam mixture was continuously injected into a vessel initially filled with an air-steam mixture. The present report is concerned with those tests.

Igniters were "powered on" during the injection and usually a propagating flame would be produced that would burn back down to the injection point and form a stable diffusion flame over the jet or plume of H_2-steam. The energy release rate associated with these flames was from 1-4 MW. Nozzles of 0.038, 0.13 and 1.0 m diameter were used in these tests. If the flowrate was held constant, the flame would burn continuously until the O_2 concentration fell below the limiting value of 5-8% required to support combustion. The flame and gas flow configuration inside the vessel is shown schematically in Fig. 1.

Above the flame, there is a plume or jet of hot products that impinges on the top of the vessel at a stagnation point. Heat transfer rates from the gas to the vessel are highest at this point. The impinging gas flows radially outward from the stagnation point as a "wall jet"; heat transfer rates decrease continuously with increasing distance from the stagnation point. Entrainment of the surrounding atmosphere by the flame

and downstream flow induces a general circulation inside the vessel. This circulation (and the stirring motion of the fans in some tests) provides the turbulence level and mean flow that determines the heat transfer rate from the hot combustion products to the vessel surface outside the stagnation flow region.

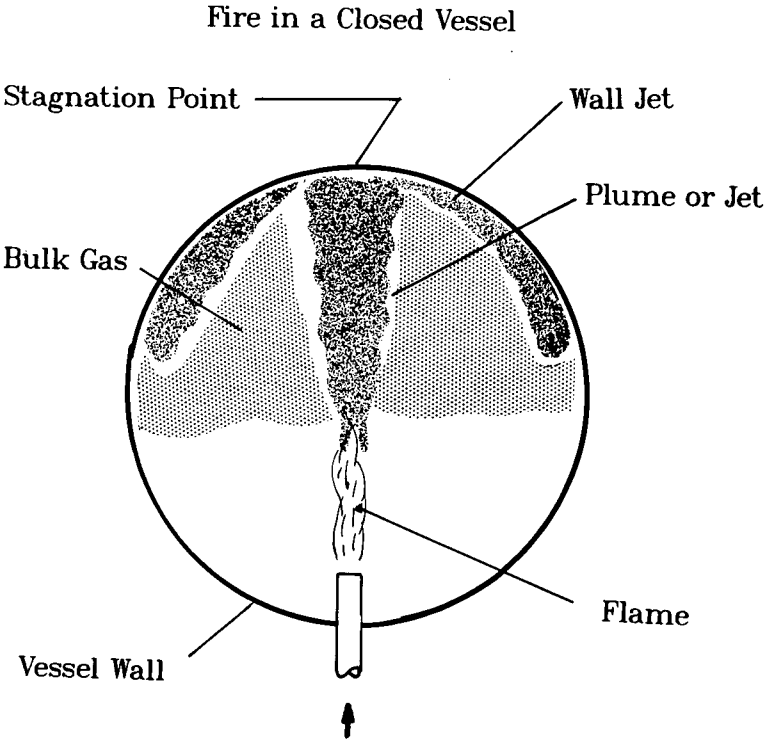

Figure 1. Configuration of flame jet or plume and induced flow inside the vessel

The rate of convective heat transfer is the most significant unknown in the analysis of these experiments. For this reason, the data analysis in this report concentrates on the determination of the convective heat transfer coefficient from the limited measurements that were made. The issue of scaling up to nuclear plant containment building dimensions is briefly addressed.

The structure of the report is as follows. The data are presented in Section 2 and Appendix A. An overview discusses the initial conditions, instrumentation and signal quality for all 16 tests. Individual data plots are presented in Appendix A for selected instruments in each test. Only pressure plots are given for the 12 tests that were not analyzed at SNLA. Injection, mixing and ignition behavior are discussed in Section 3. Heat transfer modeling is discussed in Section 4. Examples of a test simulation and

the inverse method of determining heat transfer rates from data are given using test C3. A summary of the reduced data and convective heat transfer coefficients is given in Section 5. Speculations are made about the possible scaling laws applicable to the heat transfer coefficients. The report is summarized in Section 6.

2 Test Conditions

2.1 Overview

Sixteen CI tests were performed. The source type, flowrates, igniter location(s), and fan/spray options are given for each test in Table 1. Initial conditions, gas pressures, gas temperatures, steam mole fractions, and burn durations are given in Table 2.

The geometry of the vessel and associated equipment is shown in Fig. 2. The H_2- steam mixture was injected at the bottom of the vessel as a jet or plume directed vertically upward. The source was located slightly off the centerline and about 2 m (7 ft) from the bottom of the vessel. The vessel was equipped with a variety of instruments to measure gas pressure, gas temperature, gas concentration, wall temperature, and total and radiative heat flux. These instruments and their placements are described in detail in both the EPRI report[1] and the report[2] on the premixed test data analysis. The locations of the instruments discussed in the present report are given in Table 1 of Appendix A.

In general, there were only a limited number of calorimeters included in the Hydrogen Behavior tests. Further, the data sets provided for each test of this series were limited typically to only the signals from SNLA-provided instrumentation. For the Equipment Survival tests, significantly more calorimeters were included, and Sandia was provided with these data and with additional gas and wall thermocouple data.

An assessment of the instrumentation for which data were provided to Sandia (on computer tapes) from the continuous-injection combustion tests was performed following preliminary data processing. This processing was used to reduce the EPRI-provided data sets from 3000-4000 time-signal pairs to a more reasonable set of 200-600 pairs by elimination of redundant data and some data smoothing. Tables 3 and 4 provide this assessment of signal quality for the tests of the Hydrogen Behavior and Equipment Survival series, respectively. Assessment of radiative calorimetry signals for these tests have been omitted given the problems with processing these data (described in Ref. 2).

In general, there are few data available to SNLA for analysis of the Hydrogen Behavior tests. Wall and gas thermocouple data were provided for only 2 of the 12 tests; only one pressure signal is available for 5 of the 12 tests. The only tests which can be analyzed in any detail are NTSC03 and NTSC08. There are fairly complete data sets available for the 4 tests of the Equipment Survival Series. The two tests, CS1 and CS5, that had constant–flowrate sources have been analyzed.

Plots of the data are given in Appendix A for selected signals from each test. Only a pressure signal is given for most tests.

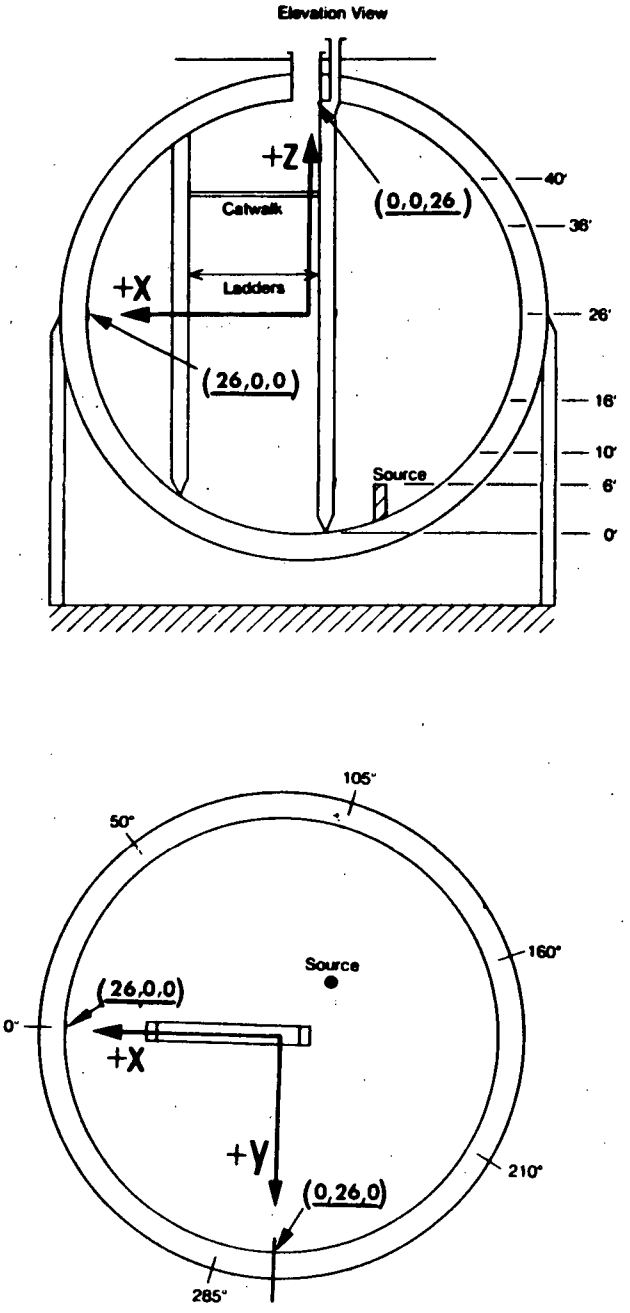

Figure 2. Coordinate system used to define locations in the dewar. These are rectangular cartesian coordinates, (x, y, z), with the origin (0,0,0) at the center of the vessel. The z axis is vertical , x and y axes are in the horizontal plane as shown. These dimensions are given in feet for consistency with Refs. 1 and 2.

Table 1. Test Matrix

Test	Date	Gas Injection Rates H_2 (kg/min)	H_2O (kg/min)	Igniter Location(s)[c]	Fans[a] or Sprays[b]	Source[d]
			Hydrogen Behavior Series			
C1	8-25-83	2.1	28	T,3E		D
C2	8-26-83	2.0	28	T,3E	S	D
C3	8-30-83	1.8	29	3E	F	D
C5	8-23-83	1.6	0.0	T,3E		D
C7	9-8-83	0.4-2.7[e]	0-55[e]	T,C,B		D
C8	9-8-83	1.4	75	T,3E		D
C9	9-12-83	1.9	10.	B		D
C10	9-13-83	1.8	63	3E		D
C11	9-13-83	1.8	63	3E		D
CN1	9-19-83	1.9	27[f]	T,3E		N
CN2	9-20-83	1.8	0-75[e]	T,3E	F,S	N
CN3	9-22-83	1.8	45[f]	B	F,S	N
			Equipment Survival Series			
CS1	1-3-84	1.8	28	T,3E		S
CS2	1-5-84	3.6	0-27[e]	T,3E		S
CS5	1-10-84	1.8	9	1E		S
CS6	1-24-84	0.4-1.30	9-23	B	S	S

[a]Fans operative (F).
[b]Sprays operative (S).
[c]Igniters near top (T), 3 or 1 on wall at Equator (3E, 1E), at center (C) or near bottom below source elevation (B).
[d]Vertical injection through a diffuser (D, diameter 1 m), nozzle (N, diameter 12.7 cm), or sonic nozzle (S, diameter 3.8 cm).
[e]Blowout test, variable flowrates.
[f]Steam flowrate oscillated, mean value given.

Table 2. Initial Conditions

Test	P_o (kPa)	T_o (K)	X_{H_2O}	T_{jet} (K)	t_{on} (s)	t_{off} (s)	Δt (s)
Hydrogen Behavior Series							
C1	120.7	346	0.29	383	170	700	530
C2	100.7	328	0.15	390	210	600[a]	380-980[a]
C3	107.6	346	0.32	393	292	706	414
C5	106.2	344	0.30	348	170	1030	860
C7	100.7	341	0.27	388	145	1220[b]	–[b]
C8	110.4	344	0.29	408	365	720	355
C9	110.4	344	0.29	383	–[c]	–[c]	–[c]
C10	109.0	344	0.29	413	250	600	350
C11	134.5	356	0.39	408	330	650	320
CN1	106.9	344	0.30	398	250	705	455
CN2	100.0	329	0.16	413	140	900[d]	210,400[d]
CN3	110.4	326	0.11	400	390	1240	850
Equipment Survival Series							
CS1	106.9	343	0.29	403	306	900	594
CS2	106.9	343	0.29	393	100	535[e]	135,315[e]
CS5	93.1	325	0.15	403	246	900	654
CS6	91.0	321	0.12	373	–[f]	–[f]	–[f]

[a]Erratic burning after 600 s.
[b]Variable flowrate, erratic burning
[c]Deflagration after 1000 s, see text. Designation changed to P8.
[d]Variable flowrate, two burns.
[e]Variable flowrate, two burns.
[f]Deflagration at 4050 s.

Table 3. Signal Quality for the Hydrogen Behavior test series

Instrument	Test										
	C5	C1	C2	C3	C7	C8	C10	C11	CN1	CN2	CN3
Pressure Transducers[a]											
P102	U	U	U	G	U	G	U	U	U	U	U
P105	G	G	G	M	B	B	B	B	B	B	B
Total Slug Calorimeter											
H104	G	G	G	G	G	G	G	G	G	G	G
Total Thin-Film Gauge											
H232	G	G	G	M	G	G	G	G	G	G	G
Total Gardon Gauge											
H106	G	G	G	U	R	R	R	R	R	R	R
Wall Thermocouples											
T120	U	U	U	G	U	G	U	U	U	U	U
T121	U	U	U	G	U	G	U	U	U	U	U
Gas Thermocouples (3-mil)											
T101	U	U	U	G	U	G	U	U	U	U	U
T105	U	U	U	G	U	G	U	U	U	U	U
Gas Thermocouples (32-mil)											
T114	U	U	U	G	U	G	U	U	U	U	U
T118	U	U	U	G	U	G	U	U	U	U	U

[a] Pressure sensor P104 inoperative for all tests
'U' – Signal not provided by EPRI (*i.e.* "unavailable")
'R' – H106 was reconfigured as a radiative gauge
'G' – Signal quality "good"
'M' – Signal quality "marginal"
'B' – Signal quality "bad"

Table 4. Signal Quality for the Equipment Survival test Series

Instrument	Test			
	CS1	CS2	CS5	CS6
Pressure Transducers[a]				
P101	U	U	U	G
P102	G	G	G	G
P103	U	U	U	G
Total Slug Calorimeter				
H104	G	G	G	G
Total Thin-Film Gauge				
H232	G	G	B	G
Flat-Plate Gauge				
T501	G	M	G	G
T502	G	M	G	G
T503	G	M	G	G
Aluminum Cube				
T504	G	G	G	B
T505	G	G	G	G
Total Schmidt-Boelter Gauges				
H502	M	G	M	M
H503	G	G	G	M
H504	M	M	B	M
H506	M	M	B	B
H507	B	B	B	M
Wall Thermocouples				
T120	M	G	M	G
T121	G	G	G	G
Gas Thermocouples (3-mil)				
T101	G	G	G	G
T102	G	G	G	G
T105	G	G	G	G
Gas Thermocouples (32-mil)				
T118	G	G	G	G
T151	G	G	B	B

[a] P104 and P105 inoperative for all tests
'U' – Signal "unavailable"
'G' – Signal quality "good"
'M' – Signal quality "marginal"
'B' – Signal quality "bad"

3 Injection, Mixing and Ignition

Four distinct types of ignition behavior were observed in the tests. These are: (1) slow ignition and diffusion flame burning; (2) fast ignition (deflagration) followed with diffusion flame burning; (3) deflagration and no diffusion flames; (4) no ignition of any kind. The dominant behavior was of type (1), slow ignition followed by a diffusion flame. The other three behaviors were singular events that were observed in only one test each out of the entire program of testing. Despite the exceptional nature of these events, it is possible to understand these phenomena and the circumstances under which they might occur. The ignition behavior is determined by two factors: the fluid motion induced by the H_2-steam source and the location of the igniter.

The fluid motion in the vessel during injection depends crucially on the source characteristics. For subsonic jets and plumes, the relevant dimensional quantities are the source diameter, fluid density, and velocity. These are listed in Table 5 together with two nondimensional quantities, the Froude number Fr and the Reynolds number Re:

$$Fr = \frac{\rho U^2}{g \Delta \rho D}; \qquad Re = \frac{UD}{\nu};$$

where U is the source velocity; ρ the source density; D the source diameter; $\Delta\rho$ the source-atmosphere density difference; g the gravitation acceleration; ν the kinematic viscosity of the jet fluid.

The Froude number characterizes the most important aspect of these sources, the relative role of inertial and gravitation forces. All tests with the diffuser source (D=1 m) are characterized by very low Froude numbers, $Fr \sim 0.1$, indicating that buoyancy forces dominate the plume flow above the source. The nozzle sources (D=0.13 m) have intermediate Froude numbers, $Fr \sim 5 \times 10^3 - 10^4$, and the gravitational and inertial forces are comparable. The sonic sources ($D = 0.038$ m) have very large Froude numbers, $Fr \geq 10^5$, and the jet flow above the source is dominated by inertial forces. The influence of the Froude number on the mixing is discussed below.

3.1 Slow Ignition and Diffusion Flame Burning

This was the behavior observed in the majority of tests. At the start of all tests, the igniters were turned on and the flow of H_2 and steam started. There was a delay of 100 to 400 seconds between the start of injection and the formation of a diffusion flame at the source. No pressure pulses or deflagrations were observed and the diffusion flame appeared (from IR video cameras inside the dewar) to be ignited by a very weak flame propagating from the igniter(s) back to the source. Depending on the igniter location(s) and the source characteristics, ignition could occur relatively quickly (2-10 s) or take place over a longer time of several minutes.

For this dominant ignition sequence, the gas pressure and temperature rises within the vessel were produced entirely by the diffusion flame. An example of the gas pressure

produced by test C1 is shown in Fig. 3. The slow initial rise in the pressure is due to the compression of the original gas in the vessel by the injected H_2-steam mixture. After a period of 170 s, the hydrogen concentration has increased to the point ($\sim$ 4-5%) where the igniter at the top of the vessel initiates combustion in the surrounding gas. The combusting region then slowly propagates downward toward the source and causes the ignition of the entire plume.

Table 5. Source Parameters

Test	U (m/s)	ρ (kg/m^3)	Fr	Re
		Hydrogen Behavior Series		
C1	1.35	0.456	0.10	4.7×10^4
C2	1.64	0.376	0.15	4.6×10^4
C3	1.55	0.396	0.13	4.5×10^4
C5	0.52	0.074	0.0019	3.9×10^3
C8	4.55	0.535	1.76	1.8×10^5
C9	0.55	0.070	0.0024	4.0×10^3
C10	2.94	0.467	0.60	9.7×10^4
C11	2.36	0.584	0.40	9.8×10^4
CN1	98.4	0.389	4.0×10^3	3.5×10^5
CN3	136	0.233	9.5×10^3	5.7×10^5
		Equipment Survival Series		
CS1[a]	439	-	-	-
CS5[a]	531	-	-	-

[a]Sonic jet.

This burning plume or diffusion flame has a power output of about 3 MW that causes the large increase in gas pressure at this point. As the combustion products are mixed with the vessel contents and the energy is absorbed by the vessel walls, the rate of pressurization decreases. The diffusion flame persists until 700 s when the O_2 concentration in the vessel falls below $\sim$8%. At this point, the flame goes out and the pressure decreases as heat is continually absorbed by the vessel walls. Eventually the pressure begins to rise again due to compression by the injected gas.

This ignition behavior is consistent with the formation of a stable layer of hydrogen at the top of the vessel. The layer is supplied with hydrogen by the jet or plume formed above the source and the depth of the layer increases steadily with time. Although there

were insufficient measurements of hydrogen concentration made to show this in detail, the phenomena of stable stratification is well known and has been observed in many similar types of mixing experiments. The basic sequence of events was first described by Baines and Turner[3] and is illustrated in Fig. 4.

The first phase of the process is the development of the jet or plume above the source. This process has been investigated by Turner[4] for impulsively started buoyant sources with negligible momentum, *i.e.*, $Fr << 1$. He found that the transient flow could be approximated by a vortex flow at the head and a steady plume flow behind. The head travels at a speed equal to about 0.6 of the local centerline velocity for the equivalent steady plume. From the start of injection to impingement on the vessel top, the entire process takes about 10 s for the sources used in the NTS tests.

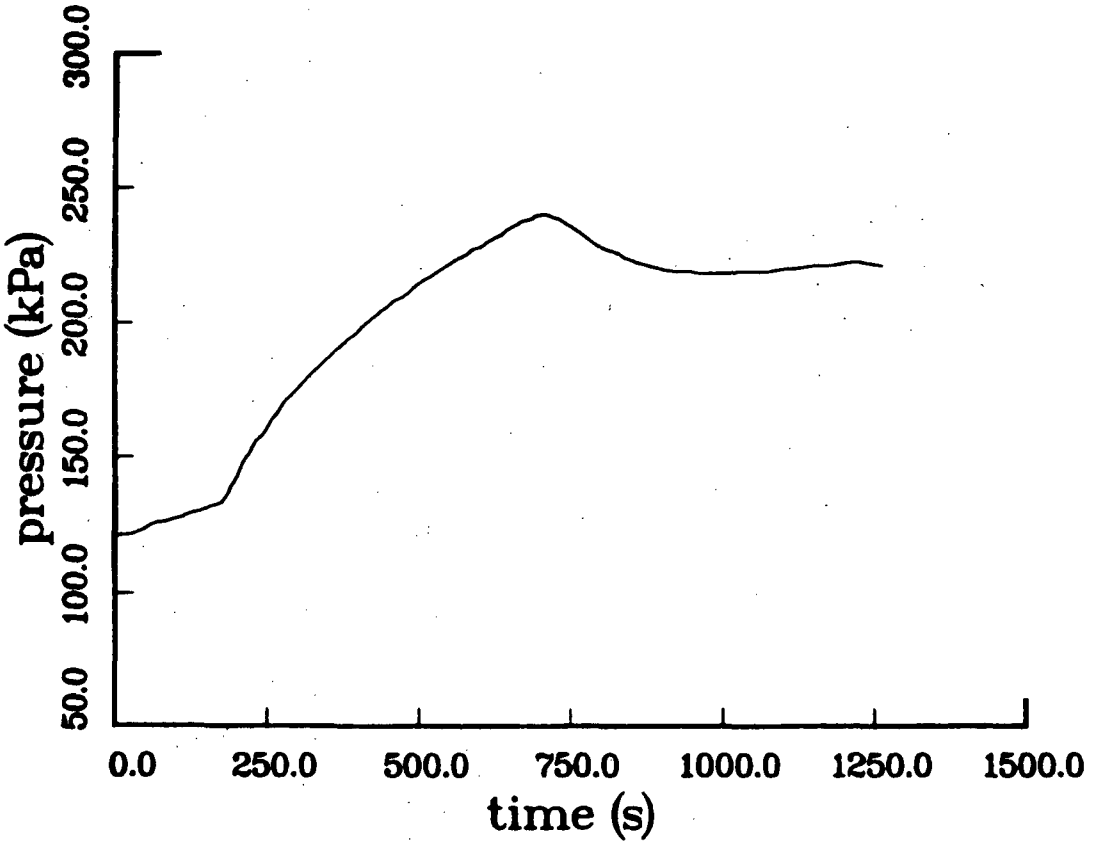

Figure 3. Gas pressure in Test C1. This exhibits the signal characteristic of slow ignition followed by diffusion flame burning.

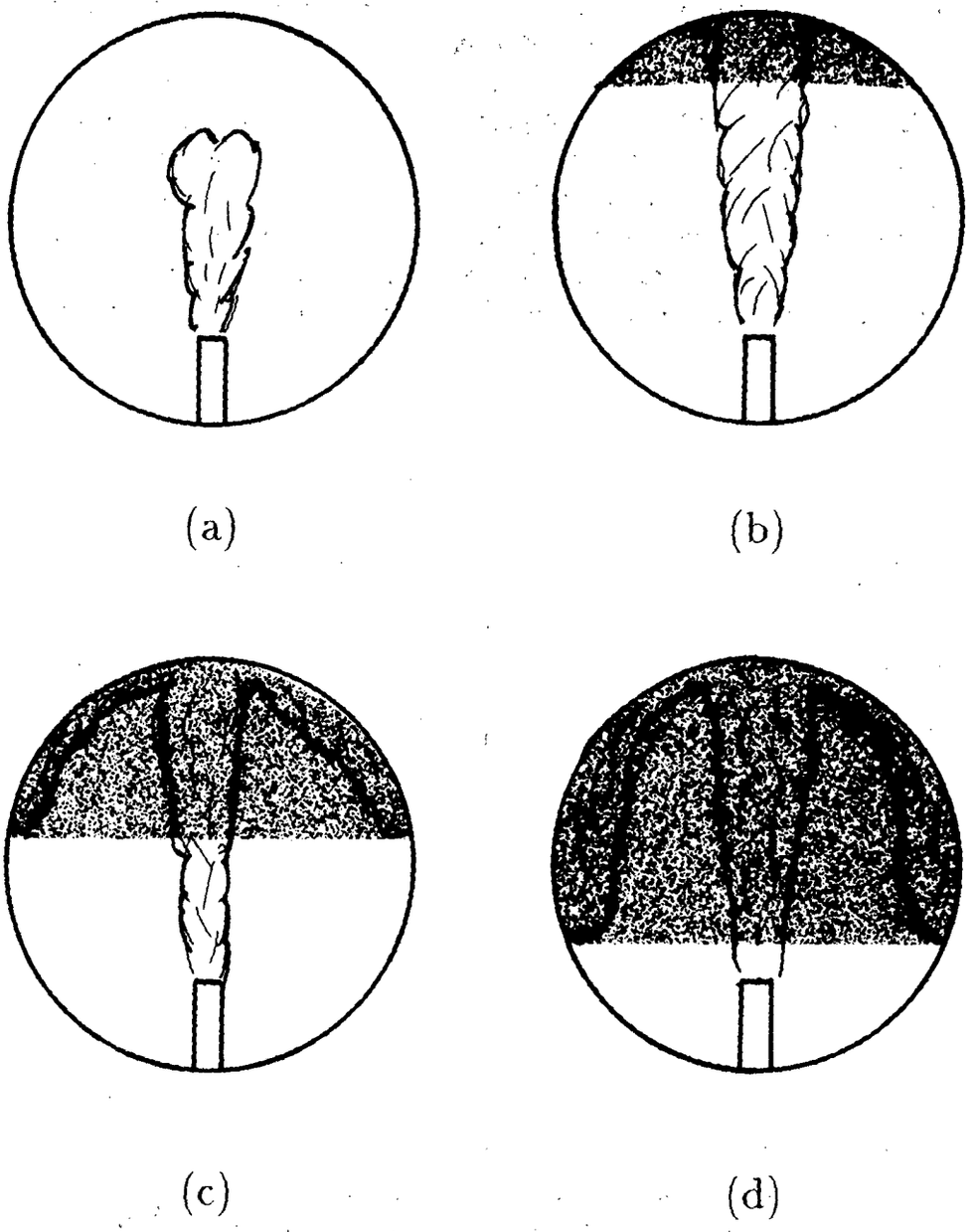

Figure 4. Sequence of events observed in stable mixing. (a) Transient development of the plume or jet flow. (b) Impingement of the jet on the top of the vessel and the formation of a stable layer. (c) Growth of the stable layer. (d) Asymptotic approach of the bottom of the layer to the source level.

The second phase of the process is the impingement of the plume and development of a stable layer. The vertical motion of the fluid in the plume is converted to a radially outward motion along the top of the vessel. This radial motion is frequently referred to as a "wall jet." Since the fluid in the wall jet is lighter than the vessel contents, eventually the fluid will separate from the wall and turn inward toward the jet. This occurs when the momentum of the fluid in the wall jet decreases below a critical level and the upward buoyancy forces dominate.

Fluid separated from the wall spreads out horizontally to form a stably stratified layer. This fluid consists of the original source fluid and vessel fluid entrained by both the plume and the wall jet. A nearly planar horizontal interface separates the lighter fluid at the top of the vessel from the original vessel contents. In the third phase of the process, the interface moves downward toward the source elevation. There is a slow circulation within the stable layer and the motion of the vessel contents below is primarily horizontal due to entrainment into the plume. For a very–low–momentum plume, the circulation within the stable layer can be quite weak and stratification occurs within the layer. In this situation, the interface remains planar and only asymptotically approaches the source elevation; this is the fourth phase.

As discussed in Baines and Turner, a simple solution can be obtained for the interface motion in phases 3 and 4 if the source is a low–momentum plume. This solution neglects the initial mass flowrate in the source and equates the rate at which the original vessel fluid below the interface is being consumed dM_l/dt to the plume mass entrainment rate $\dot{M}_p$.

$$\frac{d}{dt}M_l + \dot{M}_p = 0$$

The first term is computed as

$$\frac{d}{dt}M_l = \rho_v A(z)\frac{d}{dt}Y$$

where the original vessel fluid density is ρ_v, the interface height is Y, and the vessel area perpendicular to the plume is $A(z)$. An idealized similarity solution is used for the plume entrainment

$$\dot{M}_p = C_m \rho_v \left(\frac{W}{\rho_v}\right)^{2/5} (Y - z_o)^{5/3}$$

where $C_m = 0.21$, z_o is the origin of the plume and W is the buoyancy flux, defined as

$$W = \int_0^\infty g\Delta\rho U 2\pi r \, dr$$

This integral is an invariant for a plume in a uniform atmosphere and can be computed at any elevation; it is simplest to do the computation at the source where all the conditions are known.

I have computed the motion of the interface inside a sphere for a point source located 0.7 radii below the center and on the vertical axis of symmetry. This approximates the geometry of the NTS experiments. The results are shown in Fig. 5; these were obtained by numerical integration. The interface motion is described with normalized variables $\tilde{Y} = Y/R_v$ and $\tau = t/T_{BT}$, where R_v is the vessel radius and T_{BT} is the characteristic filling time. The filling time is given by

$$T_{BT} = \frac{\rho_v R_v^3}{\dot{M}_p R_v}$$

which is approximately one-third the time required to entrain the entire contents of the vessel through the plume once. These filling times are given in Table 5 for all tests with low Froude number.

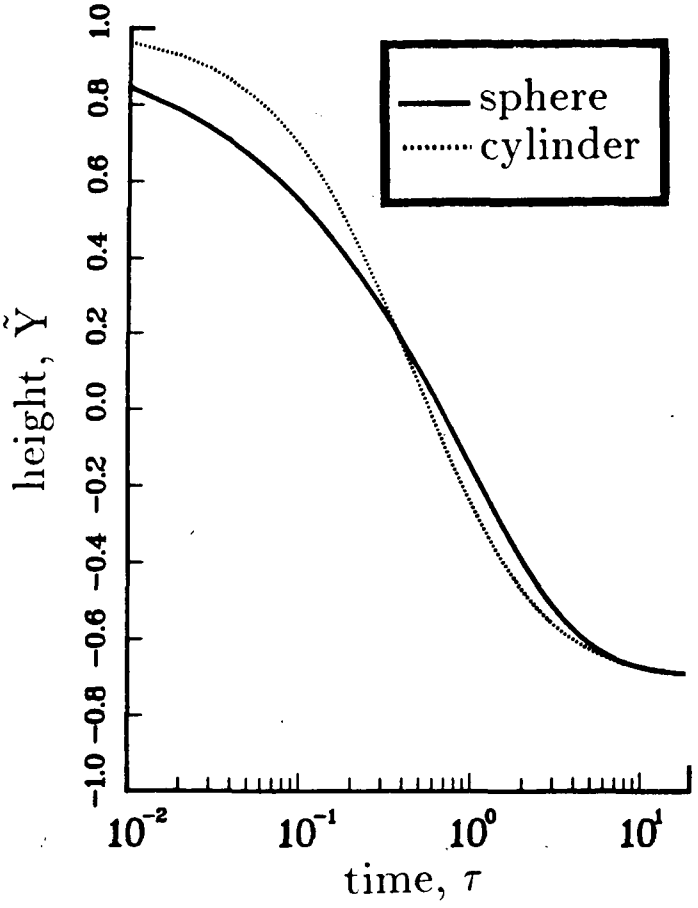

Figure 5. Motion of the interface between mixed and original fluid. Solution for a sphere with the source at -0.7R on the vertical axis. Solution for the equivalent cylinder is also shown.

The simple picture discussed in previous paragraphs changes dramatically with increasing jet Froude number. This has been demonstrated in small-scale experiments[5] using jets of brine into fresh water. As the Froude number is increased, the interface

between mixed and unmixed fluid breaks down and at very high Froude numbers, a large–scale circulation is set up within the vessel. This circulation eliminates any stratification within the mixed layer and efficiently mixes the container fluid with the jet fluid. The mixing occurs throughout the vessel and extends to regions usually not touched in low Froude number flow, *i.e.*, the stagnant region below the source elevation. Experiments in a right circular cylinder suggest that the transition between stable and unstable mixing occurs at a source Froude number of ~ 3000.

3.2 Fast Ignition and Diffusion Flame Burning

This ignition sequence was observed in one test, CN3. The ignition source was near the bottom and a jet with intermediate Froude number was the source. At intermediate Froude numbers, a front is present between the mixed and unmixed fluid. This front moves much more rapidly than in the low Froude number cases and there is much more circulation within the mixed region, *i.e.*, stratification does not develop. When the front reaches the ignition source near the bottom, the resulting flame can propagate through a large portion of the mixed fluid. This produces the pressure spike at the beginning of the burn that is characteristic of a deflagration. This pressure spike can be observed in Fig. 6 at a time of 390 s. Following the spike is an almost linear increase in pressure due to the diffusion flame. The slope is much smaller than in previous examples due to the enhanced heat transfer caused by the fluid motion induced by the fans and sprays and also, the thermal sink effect of the water evaporated from the sprays.

3.3 Deflagration and No Diffusion Flames

Prior to the actual testing, most computations suggested that this behavior was expected to dominate. In fact, a very special set of circumstances had to be arranged to observe this behavior in the last test, CS6; and only one small deflagration was observed near the end of the test. Deflagrations, either multiple or single, were exceptional cases. The pressure trace for CS6 is shown below. Note that the first four spikes in the pressure signal are not burns but rather the result of purging the water from the lines connecting the transducers to the vessel. A single deflagration occurs at 4000 s. A very low flowrate was combined with water sprays and bottom ignition to achieve this effect.

Like test CN3, the source Froude number was in an intermediate regime. This results in a mixed layer above the igniter, although some stratification is still possible. There is a long delay until the hydrogen concentration at the igniter reaches $\sim 4\%$ and then the resulting flame propagates throughout the vessel. This deflagration produces the pressure spike at 4000 s.

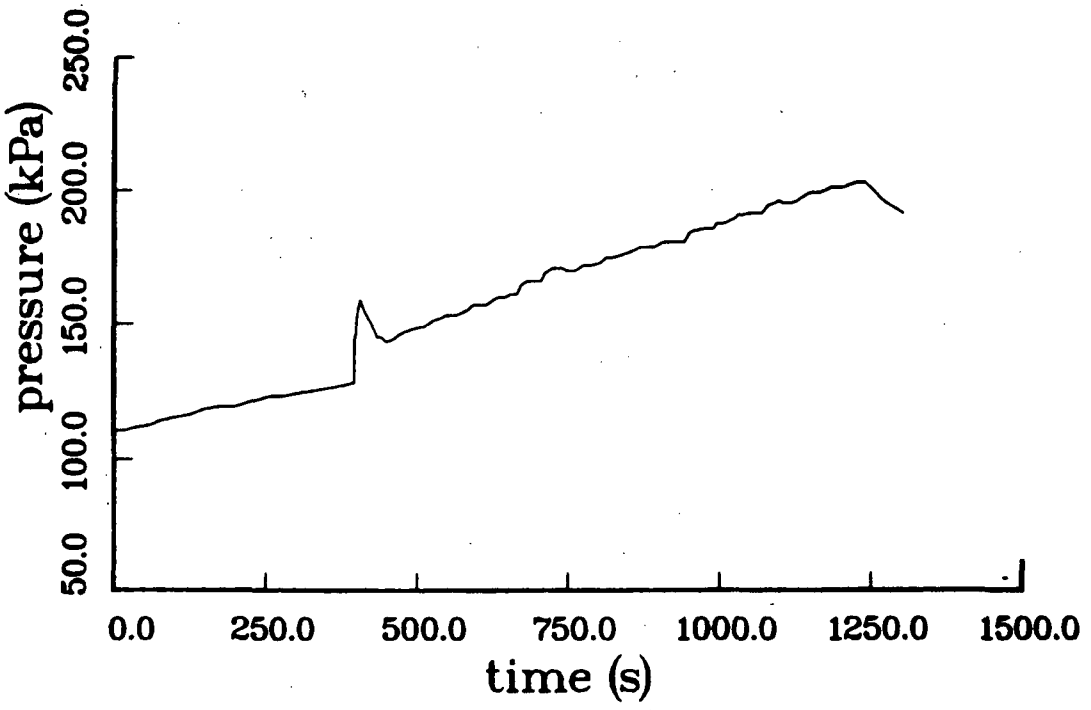

Figure 6. Gas pressure for test CN3. Note the spike due to the deflagration at the beginning of the diffusion flame ignition. Sprays and fans were both on during the test.

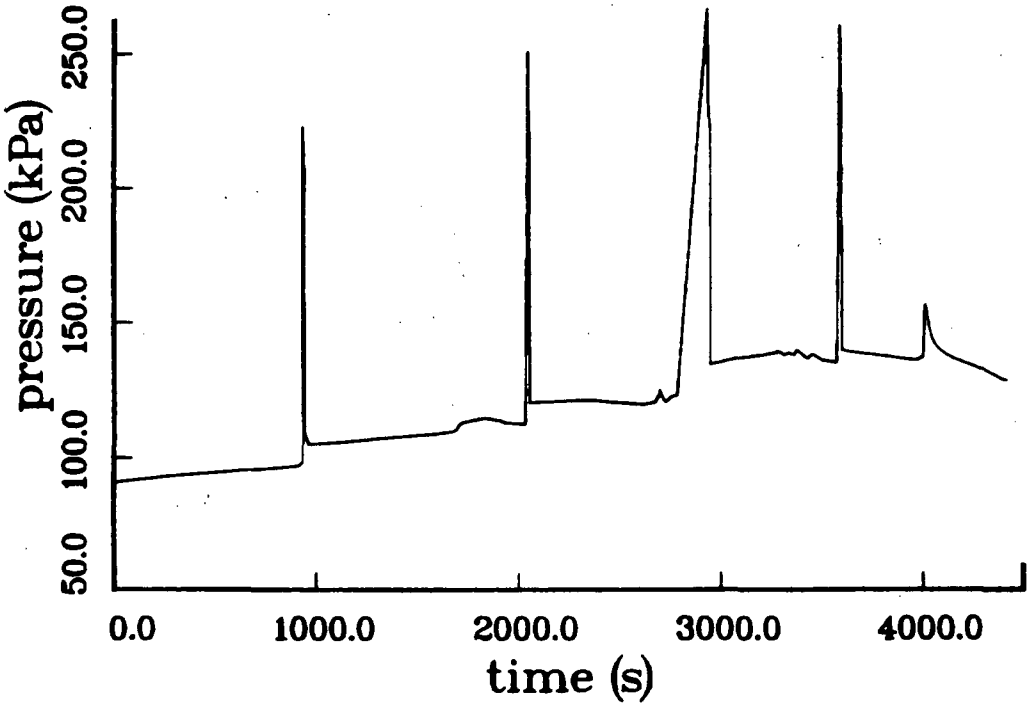

Figure 7. Gas pressure for test CS6. Note that the first four spikes are artifacts. A deflagration occurs at 4500 s. Sprays were on during the test.

3.4 No Ignition at All

This behavior was observed in Test C9 which was later designated P8 after operator intervention resulted in a deflagration. The flow above the source was a plume with very low Froude number, $Fr \sim 0.002$. This flow produced a stable mixing layer which never got any lower than the source elevation. Since the igniter was ~1 m below the source, no ignition was observed as long as the atmosphere was quiescent. Due to concerns about the buildup of hydrogen, the source flow was turned off at about 720 s. Igniters were left on, the fans were turned on at 975 s, and ignition took place at 1060 s. A deflagration propagated through the vessel, producing a peak pressure of ~400 kPa. This pressure is in good agreement with the adiabatic, constant–volume value for a mean hydrogen concentration of 11.1%, the amount computed by integrating the flowrate.

The hydrogen concentration profiles shown in Fig. 8 provide a nice confirmation of the simple Baines and Turner theory of stable mixing. A delay of 300 s is observed between the detection of hydrogen at +10 ft and -10 ft. According to the simple theory, the characteristic filling time is 149 s and the delay should be approximately 250 s.

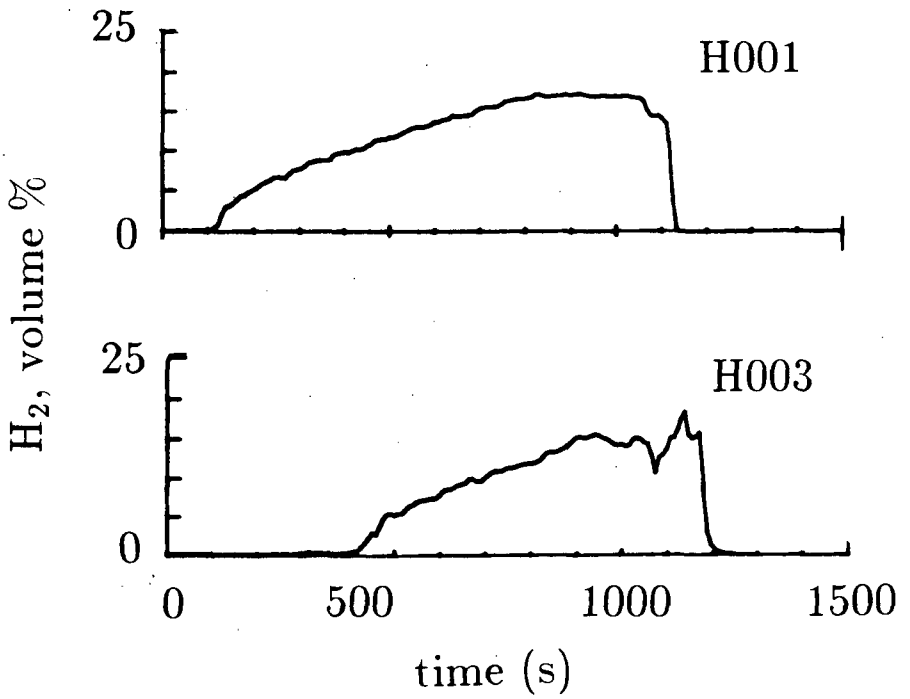

Figure 8. Hydrogen concentration for test C9. Sensor H001 located at +10 ft ($z/R = 0.38$); sensor H003 located at -10 ft ($z/R = -0.38$).

4 Modeling

The modeling and analyses performed for the CI tests are primarily based on thermodynamic considerations and ignore the details of the fluid flow and spatial variation of gas temperature and wall heat flux. The injected fluid and combustion products are also assumed to instantaneously mix with the fluid that is already present in the vessel. This type of treatment is appropriate considering the rather crude nature of the measurements and our lack of knowledge about these processes. For tests in which mixing is strongly driven by a high–momentum jet or fans within the vessel, this type of modeling is very successful. For low–momentum plume fires, we cannot expect as much from the model and as discussed below, the stratification produced by buoyancy can be quite important.

One aspect of these tests that will always require consideration of the local flowfield is the plume or jet flow above the fire and the resulting stagnation point at the ceiling of the vessel. While no specific data on this region were obtained in the NTS tests, the results of other investigations and previously developed models can be utilized. In this manner, the peak heat transfer rates at the stagnation point and the spatial variation of the vessel wall temperature can be estimated.

The plan for this section is to first develop the general model and illustrate the nature of the results with approximate analytical solutions to the model. The application of the model to a single test (C3) will then be given. Following this, the inverse version of the model will be derived and the computation of the convective heat transfer coefficient given for test C3. The problem of stagnation-point heat transfer and wall temperature variation will be examined and methods for estimating the peak fluxes and temperature profiles discussed. Finally, the effects of stratification and buoyancy will be discussed.

4.1 Transport Model

The transport model is based on the integral version of the transport theorem for a single volume fixed in space[6]

$$\frac{d}{dt}\int_V \rho\left(e+\frac{u^2}{2}\right)dV+\int_{A_{jet}}\rho u\left(h+\frac{u^2}{2}\right)dA=-\int_A qdA=-Q \qquad (1)$$

where V is the vessel volume, A is the vessel area available for heat transfer, A_{jet} the area over which injection occurs, e the fluid specific internal energy, h the fluid specific enthalpy, ρ the fluid density, u the fluid velocity, q the heat flux to the vessel and Q the total heat transfer rate from the gas to the vessel.

The flow inside the vessel is subsonic (except possibly near the jet exit) and the kinetic energy $u^2/2$ can be neglected compared to the internal energy, enthalpy and heat transfer terms. In addition, the gas flowing into the vessel will be assumed to be

in a sufficiently uniform thermodynamic state that average values for h can be used, so that

$$\int_{A_{jet}} \rho u h dA = -\sum_{jet} h_j \dot{M}_j \tag{2}$$

where the sum is over all components (species) entering the vessel through the jet or plume and $\dot{M}_j$ is the mass flowrate of species j into the vessel.

The energy integral E can be rewritten in terms of the energies e_i and masses M_i of the individual species of gas within the vessel

$$E = \int_V \rho e dV = \sum_{vessel} M_i e_i. \tag{3}$$

The time derivative of the energy can then be split into two terms

$$\frac{dE}{dt} = \sum_{vessel} \frac{dM_i}{dt} e_i + M c_g \frac{dT}{dt}. \tag{4}$$

where $M = \sum M_i$ is the total mass within the vessel. On the RHS, the first term represents changes in energy due to mass addition and chemical reaction within the vessel. The second term represents the change in energy due to changes in temperature. The symbol c_g denotes the average (mass–weighted) constant–volume specific heat of the gas within the vessel

$$c_g = \sum_i y_i c_{v_i} \tag{5}$$

where y_i is the mass fraction of species i.

With these approximations and definitions, the complete energy equation can then be written as

$$M c_g \frac{dT}{dt} + \sum_{vessel} \frac{dM_i}{dt} e_i - \sum_{jet} \dot{M}_j h_j = -Q. \tag{6}$$

This result can be further simplified by utilizing the thermodynamic identity

$$h = e + \frac{p}{\rho} \tag{7}$$

where p denotes gas pressure. Applying the ideal gas law $p = \rho RT$ and assuming that the jet or plume pressure is identical to the vessel pressure (valid for all but sonic or supersonic jets) we obtain the final version of the energy equation

$$M c_g \frac{dT}{dt} = \sum_{jet} \dot{M}_j e_j - \sum_{vessel} \frac{dM_i}{dt} e_i + \dot{M}_{jet} R T_{jet} - Q \tag{8}$$

where $\dot{M}_{jet}$ is the total mass flowrate of injected gas.

This form of the equation clearly shows the different processes that cause changes in the temperature of the gas within the vessel. The first two terms on the RHS represent energy changes due to either i) differences in the composition and thermodynamic state of the gas in the jet and in the vessel or ii) chemical reaction between the different species within the vessel. Note that if the jet and vessel gas have the same composition and temperature and there is no chemical reaction, the sum of these terms vanishes. The third term represents the compression work done by the injected jet fluid on the gas within the vessel. The fourth term represents the energy change due to the sum of the heat transfer processes that result in a transfer of energy from the gas to the vessel walls.

4.2 Combustion Model

In keeping with the spirit of the transport model, a very simplified description of the combustion process is used. The diffusion flame is treated as an energy source and any hydrogen entering the vessel while the fire is burning is completely consumed. The time periods during which combustion occurs are specified as input data to the computation. The magnitude of the energy release term is determined by assuming that a stoichiometric proportion of oxygen is burned with the incoming hydrogen to produce only water as a product.

One complication that can occur is that hydrogen may be present in the atmosphere inside the vessel. This can be due to the initial transient phase during which injection is taking place but ignition has not occurred or, if the flowrate is varied during the test, the flame may extinguish and later reignite. The concentration of hydrogen in the vessel atmosphere is usually lower than the limit value (4%) for flame propagation when ignition takes place and a deflagration does not occur. One exception to this rule is when a low–momentum (plume) source of hydrogen is used and the ignition source is placed near or below the elevation of the source. This situation and the possibility of stratification and resulting deflagrations was discussed earlier in this report. Deflagrations are not included in the present model but a number of other researchers have considered this problem and many different types of models are presently available.

The combustion model we use assumes that no deflagration occurs and the hydrogen present in the vessel atmosphere is consumed within the diffusion flame only. The rate at which the atmospheric hydrogen is consumed depends on the rate at which the vessel atmosphere is being entrained into the diffusion flame. The entrainment rate is primarily a function of source momentum. For jet–like sources with high momentum, approximately three times the jet mass flowrate will be entrained.[7] For plume–like sources with low momentum, up to 15 times the plume flowrate will be entrained.[8] The actual rate of atmospheric hydrogen combustion will be somewhat lower than the entrainment rate since not all entrained fluid will enter the high–temperature portions of the diffusion flame. The computation simply takes the mass burning rate of atmospheric hydrogen to be some constant α (given as an input parameter) times the source mass

flowrate.

Based on the simple model described above, the combustion analysis reduces to a prescription for computing the time derivatives of the mass of each species within the vessel. These derivatives are then used to evaluate the second term of the energy equation (8) given above. For the simple model in which the fire is either on or off, there are two separate situations.

Fire off:

$$\frac{dM_{H_2}}{dt} = \dot{M}_{H_2}; \tag{9a}$$

$$\frac{dM_{H_2O}}{dt} = \dot{M}_{H_2O}; \tag{9b}$$

$$\frac{dM_{O_2}}{dt} = 0; \tag{9c}$$

$$\frac{dM_{N_2}}{dt} = 0. \tag{9d}$$

Fire on:

$$\frac{dM_{H_2}}{dt} = -\alpha y_{H_2} \dot{M}_{jet}; \tag{10a}$$

$$\frac{dM_{H_2O}}{dt} = \dot{M}_{H_2O} + \frac{W_{H_2O}}{W_{H_2}} \left(\dot{M}_{H_2} + \frac{dM_{H_2}}{dt} \right); \tag{10b}$$

$$\frac{dM_{O_2}}{dt} = -\frac{1}{2} \frac{W_{O_2}}{W_{H_2}} \left(\dot{M}_{H_2} + \frac{dM_{H_2}}{dt} \right); \tag{10c}$$

$$\frac{dM_{N_2}}{dt} = 0. \tag{10d}$$

The symbol W_i represents the molecular weight of the ith species.

A quantity that frequently arises in the course of the computations is the equivalent heat release rate of the fire, Q_f. This is the rate at which energy would have to be added to the gas externally as heat to produce the same gas temperature rise as the combustion process. Since the convention is that Q_f is a positive quantity, it is defined to be the difference of the two terms on the RHS of the energy equation (8)

$$Q_f = \sum_{jet} \dot{M}_j e_j - \sum_{vessel} \frac{dM_i}{dt} e_i. \tag{11}$$

4.3 Thermal Model

Heat transfer from the mixture of hot combustion products and vessel atmosphere fluid occurs through the combined actions of convection, radiation and condensation. In

the NTS tests, the vessel interior surfaces were usually hot enough so that condensation was negligible. For this reason, condensation is not considered in the present model. Models developed for deflagrations usually include a condensation submodel that could be applied to the present problem. The processes of convection and radiation are obviously coupled and a correct treatment of this mixed–mode heat transfer process is a complex undertaking. Consistent with the other simplifications used in this model, the two processes will be approximated as being uncoupled but simultaneously occuring. Standard engineering approximations will be used to compute the rate of heat transfer for each mode and the individual rates will be summed

$$Q = Q_{rad} + Q_{conv}$$

to obtain the Q term on the RHS of the energy equation (8). Each process is discussed separately below.

Convection

Convection is computed using Newton's law of cooling

$$Q_{conv} = \sum_{surfaces} A_m \mathcal{H}_m (T_g - T_m) \tag{12}$$

where the sum is over all the surfaces m that are exposed to the gas inside the vessel. For each surface, a constant value of the convective coefficient $\mathcal{H}_m$ is used. Temperatures used in this formula are T_g, the mean temperature of the gas inside the vessel and T_m, the mean temperature of the front of each surface. For the NTS experiment, the only surface of any importance is the vessel wall itself so that $m = 1$ and the front surface temperature T_1 will be denoted T_v.

Obviously, the success of this approach depends on the appropriate value of $\mathcal{H}$ being chosen. There are a number of existing heat transfer correlations that can be used to estimate $\mathcal{H}$ and comparison of simulation results with measured data can be used to improve these estimates. Estimation formulas have been not been used in the computation directly since no correlations exist for the type of mixed (forced–free) convection that actually exists in the experiments. Unfortunately, many inappropriate textbook correlations have been applied in the past to this problem leading to misleading and erroneous results. By not providing correlations, the user of this model will be forced to contemplate the crudeness of the present technique and will hopefully realize the very approximate nature of the model results.

One technique that can be used to circumvent this ignorance of the correct correlation is to use the experimental data and a variation on the present model to infer the convective heat transfer coefficient for each test. This will be referred to as the "inverse" version of the model and the details are given later. The problem of scaling and extrapolating the limited data from the present tests is also considered in later sections of this report.

Radiation

Radiation heat transfer is handled by an approximate enclosure model using an effective beam length to compute a mean gas emittance. Nonuniformity of the gas composition and temperature are not included since these have not been quantified for the NTS tests. The majority of the radiant exchange is between the combustion products (steam) mixed into the vessel atmosphere and the cooler vessel walls. A small fraction of the radiant exchange is directly from the very hot products in the flame zone itself to the cooler vessel walls with some absorption by the intervening atmosphere. The net radiant heat transfer rate from the gas to the vessel can be expressed as

$$Q_{rad} = A\epsilon_{eff}\sigma\left(T_g^4 - T_v^4\right) + \tau\chi Q_f \tag{13}$$

where σ is the Stefan–Boltzmann constant.

The first term represents the bulk–gas/vessel radiant exchange. The effective emittance ϵ_{eff} is computed using Hottel's furnace model[9]

$$\frac{1}{\epsilon_{eff}} = \frac{1}{\epsilon_g} + \frac{1}{\epsilon_v} - 1 \tag{14}$$

where the ϵ_g is the gas emittance and ϵ_v is the emissivity of the vessel wall. The gas emittance is a function of the gas composition $\mathbf{y}$, thermodynamic state p, T, and the path length $\mathcal{L}$ over which radiative transfer occurs

$$\epsilon_g = \epsilon_g\left(\mathbf{y}, p, T, \mathcal{L}\right). \tag{15}$$

The emittance is computed using the approximate, but fairly accurate exponential wide-band model of Edwards[10] and the known gas composition and thermodynamic state. The path length used for this computation is known as the *mean beam length* $\mathcal{L}$ and is based on the engineering estimate[11] of

$$\mathcal{L} = 3.5\frac{V}{A}.$$

which is $1.17R$ for a sphere of radius R.

The second term in Eq. (13) is the direct exchange between the fire and the wall. This is an empirical expression that has been deduced from experimentation. The fraction of energy radiated directly from the fire is χ which ranges between 0.05 and 0.15 for hydrogen diffusion flames in air.[12,13] The higher values of χ are for plume–like fires, the lower are for jet–like fires.

No data are available for steam–diluted flames so I have assumed that the fraction is unchanged. The transmission by the atmosphere τ is computed with the exponential wide–band model using an adiabatic flame temperature and black body distribution for the radiation source and the bulk gas temperature and properties for the absorbing gas. A typical value of τ is 0.7.

Conduction

In the one–surface model of the NTS vessel, the conduction model is greatly simplified. Since the vessel atmosphere is considered to be well–mixed and spatially uniform, only conduction transverse to the vessel surface has to be considered. In actuality, the assumption of uniform heat transfer to the vessel walls is the least realistic feature of the present model. The disagreement of the model results with the experimental data is discussed more completely in sections to follow.

A crude but greatly simplifying assumption is that the vessel walls are thermally thin and that the temperature within the wall is uniform. In that case, the energy equation for the vessel wall is

$$c_v M_v \frac{dT_v}{dt} = Q \tag{16}$$

where c_v is the heat capacity of the wall and M_v is the total mass of wall material. Unfortunately, the walls of the NTS vessel are made of relatively low thermal conductivity stainless steel. The characteristic conduction time

$$t_{cond} = \frac{\ell^2}{\kappa}$$

is fairly long, about 85 s for the 19 mm thick stainless steel vessel shell. This means that the thermally thin assumption is only valid if the transients occur on time scales much longer than this.

A better model is a one–dimensional transient conduction process in a slab with an insulated back boundary and a given flux at the front surface. The temperature distribution inside the wall is determined by solving the conduction equation

$$\frac{\partial T_v}{\partial t} = \kappa \frac{\partial^2 T_v}{\partial x^2} \tag{17}$$

with the boundary conditions of

$$-k \left.\frac{\partial T_v}{\partial x}\right|_{x=o} = \frac{Q}{A} \tag{18}$$

and

$$-k \left.\frac{\partial T_v}{\partial x}\right|_{x=\ell} = 0. \tag{19}$$

Note that the computation involves an implicit solution for the front surface temperature since it also appears in the expressions for computing the flux. This implicit problem can cause instability of the numerical solution method if not handled properly. This is due to the stiffness of the radiation condition, *i.e.*, the flux is very sensitive to changes in the surface temperature when the system is close to equilibrium. The technique used to avoid this problem is described further below.

Summary

The complete expression for the heat flux from the gas to the vessel wall is

$$Q = A\mathcal{H}\left(T_g - T_v\right) + A\epsilon_{eff}\sigma\left(T_g^4 - T_v^4\right) + \tau\chi Q_f. \tag{20}$$

This expression is used in the energy equation for the gas (8) and the boundary condition (17) for the vessel wall conduction solution. These two equations must be simultaneously solved together with the equations for the mass of each species within the vessel.

The partial differential equation (16) governing the vessel wall temperature is reduced to a set of ordinary differential equations by approximating the spatial derivative by a finite difference expression. If there are N spatial mesh points then the conduction equation reduces to N coupled ordinary differential equations for the temperatures at each mesh point. The details of this solution method are discussed in Appendix A.

The reduction of the conduction equation to a set of N ordinary differential equations allows the use of existing subroutine packages to obtain the solution to the total of $N + 5$ differential equations that make up the complete system. A fully implicit predictor–corrector method based on the Adams-Bashford-Moulton algorithm was used to perform this task. The package implementing this method, subroutine DEABM of the SLATEC mathematical library,[14] uses a built–in step–size selection technique based on maintaining user–specified error tolerances. The implicit nature of the method and the built–in error control eliminate any tendency toward instability and assure a converged solution with minimal computational effort.

A simple FORTRAN program was written to read the input conditions, call the integration routines and output the results. The thermodynamic properties of the gas were evaluated using the CHEMKIN subroutine library[15] which is based on the ideal–gas equation of state and a 4th–order polynomial fit to the specific heats. Gas thermodynamic properties computed by this method are very accurate and represent the smallest source of uncertainty in the model.

4.4 Approximate Solution

Under certain conditions, terms in the model equations can be approximated and an analytic solution found to the approximate set of equations. This analytic solution is very useful in understanding the behavior of the numerical solutions to the full model. The approximations used to simplify the model are:

1. Thermally thin vessel wall. Neglect conduction and treat the wall as a lumped mass. No other heat sinks present.

2. Convection heat transfer only. Neglect radiation.

3. Constant gas specific heat. Neglect differences between species.

4. Neglect the increase of gas mass inside the vessel during the burn. $\dot{M} = 0$.

With these assumptions, the set of model equations becomes:

$$C_g \frac{dT_g}{dt} = \tilde{Q}_f(t) - Q_c; \qquad C_g = Mc_g$$

$$C_v \frac{dT_v}{dt} = Q_c; \qquad C_v = M_v c_v \tag{21}$$

$$\tilde{Q}_f(t) = Q_f(t) + RT_{jet}\dot{M}_{jet}(t); \qquad Q_c = A\mathcal{H}\,(T_g - T_v)\,.$$

This is a pair of coupled, linear ordinary differential equations for T_g and T_v and can be solved by a change of variables that uncouples the equations. In general the equivalent heat release rate $\tilde{Q}_f$ is an arbitrary function of time that will be different for each experiment. The general solution can be written in terms of $\tilde{Q}_f$ as

$$\Delta T = \int_o^t \frac{\tilde{Q}_f(\acute{t})}{C_g} \exp(-\frac{t-\acute{t}}{t_1})\, d\acute{t} \tag{22}$$

and

$$C_g T_g + C_v T_v = \int_o^t \tilde{Q}_f(\acute{t})\, d\acute{t}. \tag{23}$$

If $\tilde{Q}_f$ is described by relatively simple functions of time, the integrals can be evaluated analytically to obtain explicit expressions for T_g and T_v. A practical example that can be used to construct solutions for the NTS tests is the constant–strength fire. The solution for ΔT is

$$\Delta T = \Delta T_{max}\,[1 - \exp(-t/t_1)] \tag{24}$$

where the time constant t_1 is given by

$$t_1 = \frac{C}{A\mathcal{H}}; \qquad \frac{1}{C} = \frac{1}{C_v} + \frac{1}{C_g};$$

the maximum temperature difference is

$$\Delta T_{max} = \frac{\tilde{Q}_f}{A\mathcal{H}} \frac{C}{C_g};$$

and the total energy (gas and vessel) in the system is

$$C_g T_g + C_v T_v = \tilde{Q}_f t.$$

Physically, these solutions indicate that following a transient period of duration t_1, the gas–wall temperature difference reaches a constant value. A constant temperature difference implies a constant convective flux. For vessels like the NTS dewar, the total heat capacity of the wall is much larger than the total heat capacity of the gas and $C/C_g \sim 1$. Therefore, the rate of heat transfer out of the vessel almost exactly balances the heat input from the fire.

From the energy integral, we can see that the gas and wall temperatures will increase linearly with time after the initial transient. The gas is essentially passive and serves primarily to pass the energy released by the fire directly to the wall. Despite the simplistic nature of the approximate model, the solution qualitatively reproduces the test data trends. In comparing this model with the tests, there are three phases of each test that must be considered:

1. **Precombustion.** This is the initial period during which the source is turned on and hydrogen is accumulating in the vessel but not combusting. The hydrogen levels near the igniters are below the flammability limit. The effective heat release rate $\tilde{Q}_f$ is very small and is due only to the compression work by the source. This results in the linearly increasing pressure observed at the beginning of each test performed at NTS. The gradual linear increase can be thought of as a "baseline" level onto which the effects of combustion are superimposed.

2. **Combustion.** A standing diffusion flame exists at the jet or plume exit. The effective heat release rate is the sum of the chemical energy released in combustion and the compression work by the source. The combustion phase can be subdivided into two stages:

   (a) **Transient.** For a time t_1 following ignition, the gas temperature (and pressure) rises faster than the wall temperature until a significant amount of heat transfer begins to occur.

   (b) **Steady–State.** After the transient stage, the gas–wall temperature difference reaches a constant, a constant amount of heat is transferred out of the gas into the vessel and the vessel and gas temperatures rise linearly with time. The rate of temperature increase is much larger in this stage than in the precombustion stage since the chemical energy release by combustion is much larger than the compression work.

3. **Postcombustion.** After the fire has been burning for some time, the oxygen content of the vessel atmosphere will be depleted below some critical level (between 5 and 8% by volume) and the fire will be extinguished. The rate of energy addition and the vessel–wall temperature difference will decrease to the precombustion level. This transient will also occur on a timescale of t_1 and can be observed in the experimental pressure traces as the "tail" at the end of the burn. If injection

is continued after the fire is out, the tail will merge with the gradual increase due to the compression work.

The most unrealistic feature of the analytic model is the neglect of radiative heat transfer. Comparison of numerical solutions of the full model with test data indicate that 40-60% of the heat transfer can be through radiation. The next most unrealistic feature is the assumption of instantaneous mixing that is used in the original model formulation. The actual transient stage of the combustion phase is much longer than predicted because of the finite time required to mix the combustion products with the atmosphere inside the vessel. Finally, as mentioned earlier, the test data indicate a very nonuniform rate of heat transfer depending primarily on the elevation within the vessel. This is due both to the plume or jet impingement and stratification in the atmosphere.

Despite these failings, this sort of analytic approach is very useful to obtain insight into the qualitative behavior observed in CI tests. It is possible to generalize the model to treat thermally thick surfaces, such as the concrete walls in actual nuclear plant containments. The main conclusion that the gas–wall temperature difference reaches a constant following an initial transient remains unchanged. However, the gas and wall surface temperature increase as $\sqrt{t}$ rather than linearly in the quasi–steady stage.

4.5 Example: Test C3

The previously developed model was applied to test C3 of the hydrogen behavior series performed at NTS on Aug. 30, 1983. This test was performed with the fans on and the large diameter (1 m) plume source. Hydrogen and steam injection rates were constant during the entire test. The plume ignited at 292 s after the start of injection and burned continuously until it extinguished at 706 s due to insufficient oxygen. The initial conditions for the test are given in Table 6

Table 6. Initial Conditions for Test C3

H_2 flowrate	$\dot{M}_{H_2}$	0.03	kg/s
H_2O flowrate	$\dot{M}_{H_2O}$	0.45	kg/s
Gas temperature	T_o	344	K
Gas pressure	P_o	107.6	kPa
Steam fraction	X_{H_2O}	0.30	
Jet temperature	T_j	393	K
Burn start	t_{on}	292	s
Burn end	t_{off}	706	s

The vessel itself was modeled using data supplied by EPRI. The vessel was constructed of type 304 stainless steel and consisted of an inner shell 19 mm thick separated

by $\sim$ 1 m of insulation (perlite) from an outer shell. The inner shell was treated as either a lumped mass or a one-dimensional slab with an insulated rear boundary. The approximate nature of the model and poor comparison of measured and computed model temperatures indicates that the lumped–mass thermal model is adequate at the present level of sophistication. Dimensions and thermophysical data used in the computation are given in Table 7.

Table 7. NTS Vessel Parameters

Interior volume	2085	m^3
Interior radius	7.92	m
Shell thickness	19	mm
Shell mass	1.19×10^5	kg
Thermal conductivity	17.3	W/m-K
Specific heat	460.	J/kg-K
Density	8.0×10^3	kg/m^3
Thermal diffusivity	4.7×10^{-6}	m^2/s
Emissivity	0.6	

Model parameters used in or derived from the computation are given in Table 8. Equivalent heat release is computed from the given flowrates and Eq. 11 above. The actual value computed by the numerical model varies slightly during the test as the vessel atmosphere composition changes and the gas heats up; the value given in Table 8 is an average. The convective coefficient shown was determined by trial and error using a natural convection correlation as an initial guess. Gas emittance and transmission were computed from the EWB model using an average gas temperature determined from the data plots. A direct radiation fraction of 0.15 was chosen since that had been previously measured[12,13] for plume fires of hydrogen in air.

Table 8. Model Parameters for Test C3

Equivalent heat release rate	$\tilde{Q}_f$	3.7	MW
Heat transfer coefficient	$\mathcal{H}$	20	W/m-K
Gas emittance	ϵ_g	0.50	
Direct radiation fraction	χ	0.15	
Gas transmittance to fire radiation	τ	0.70	
Transient time scale	t_1	136	s
Steady–state temperature difference	ΔT	212	K

Results of the numerical simulation using the parameter values given in Tables 7-8 are shown in Figs. 9-12. Note that the simulation is compared with actual data for all signals except total heat flux; those gauges were not operational in this test. For the

particular value of λ chosen, 20 W/m-K, there is good agreement between measured and computed gas pressure and temperature. Agreement is much poorer for vessel wall temperature. This is apparently due to both stratification and the stagnation–point heat transfer at the top of the vessel.

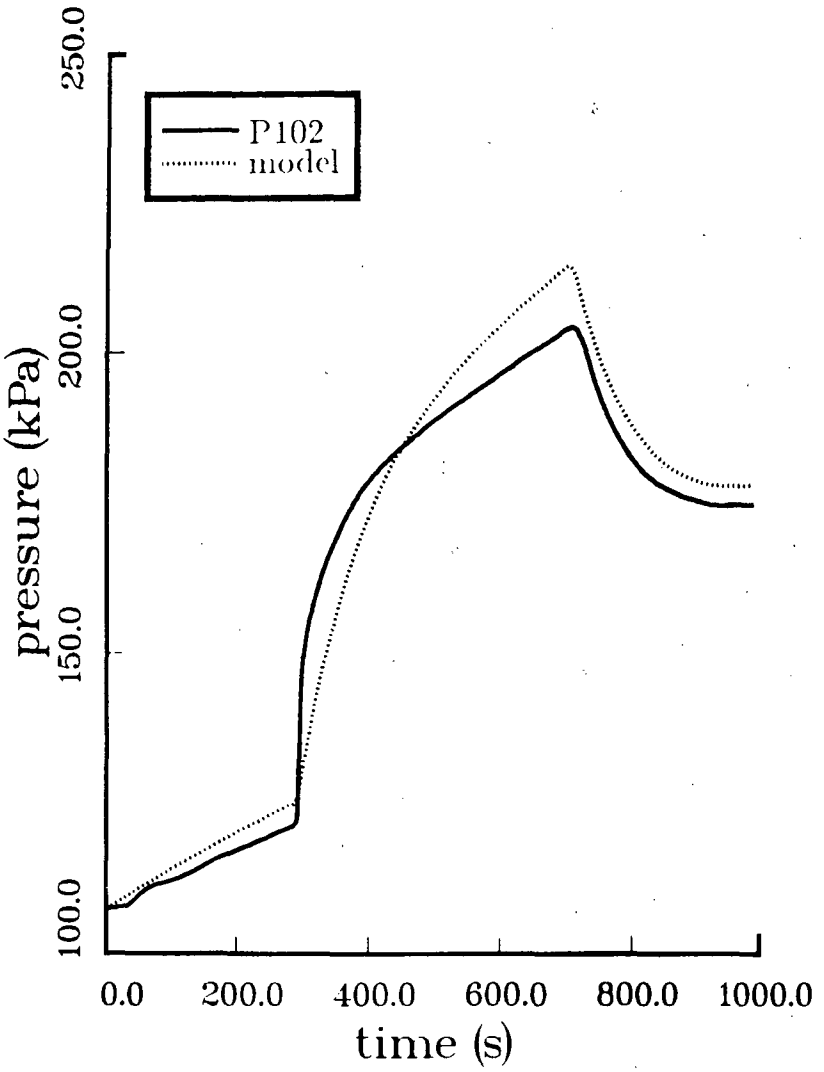

Figure 9. Measured (P102) and computed gas pressure for test C3.

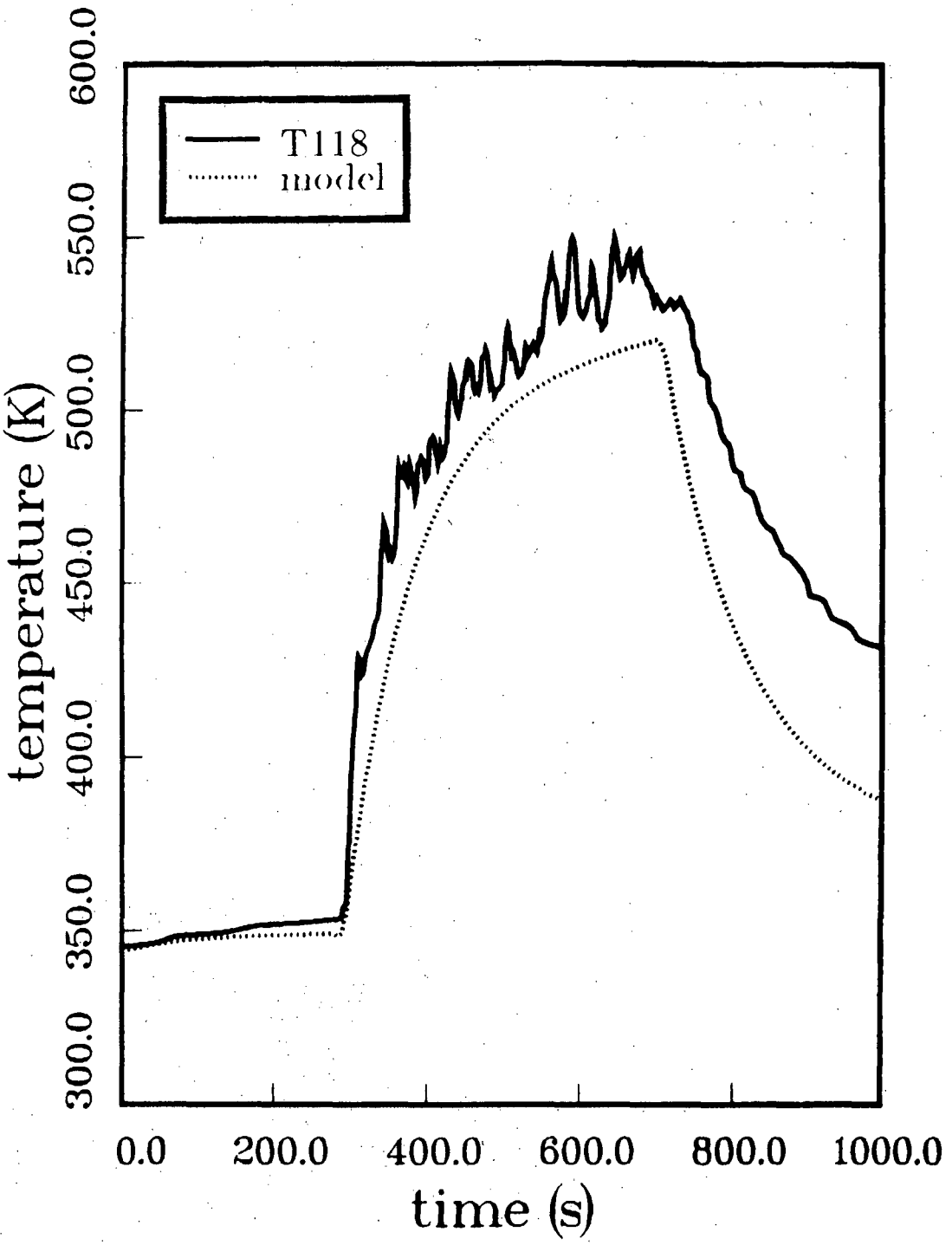

Figure 10. Measured (T118) and computed gas temperature for test C3.

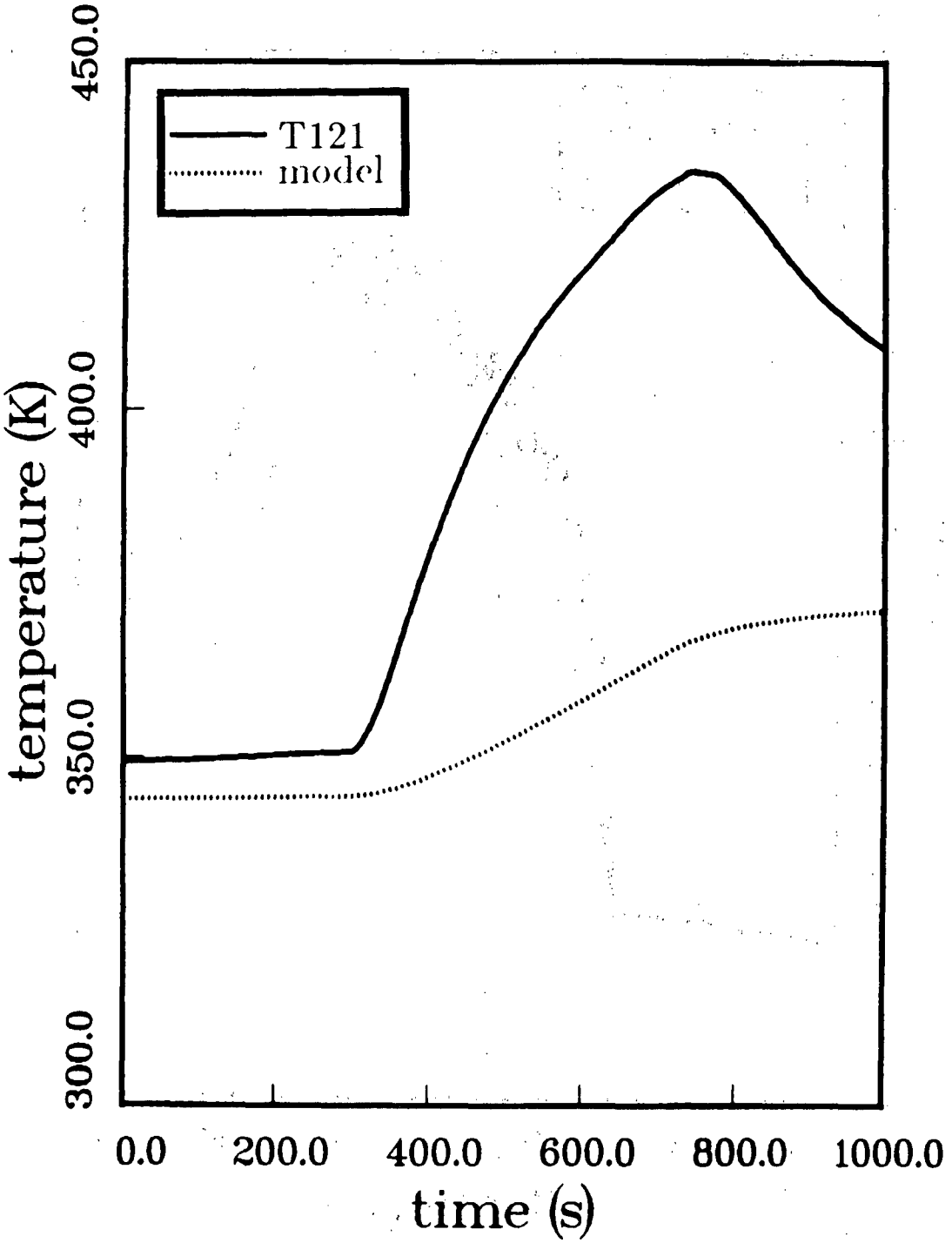

Figure 11. Measured (T121) and computed vessel wall temperature for test C3.

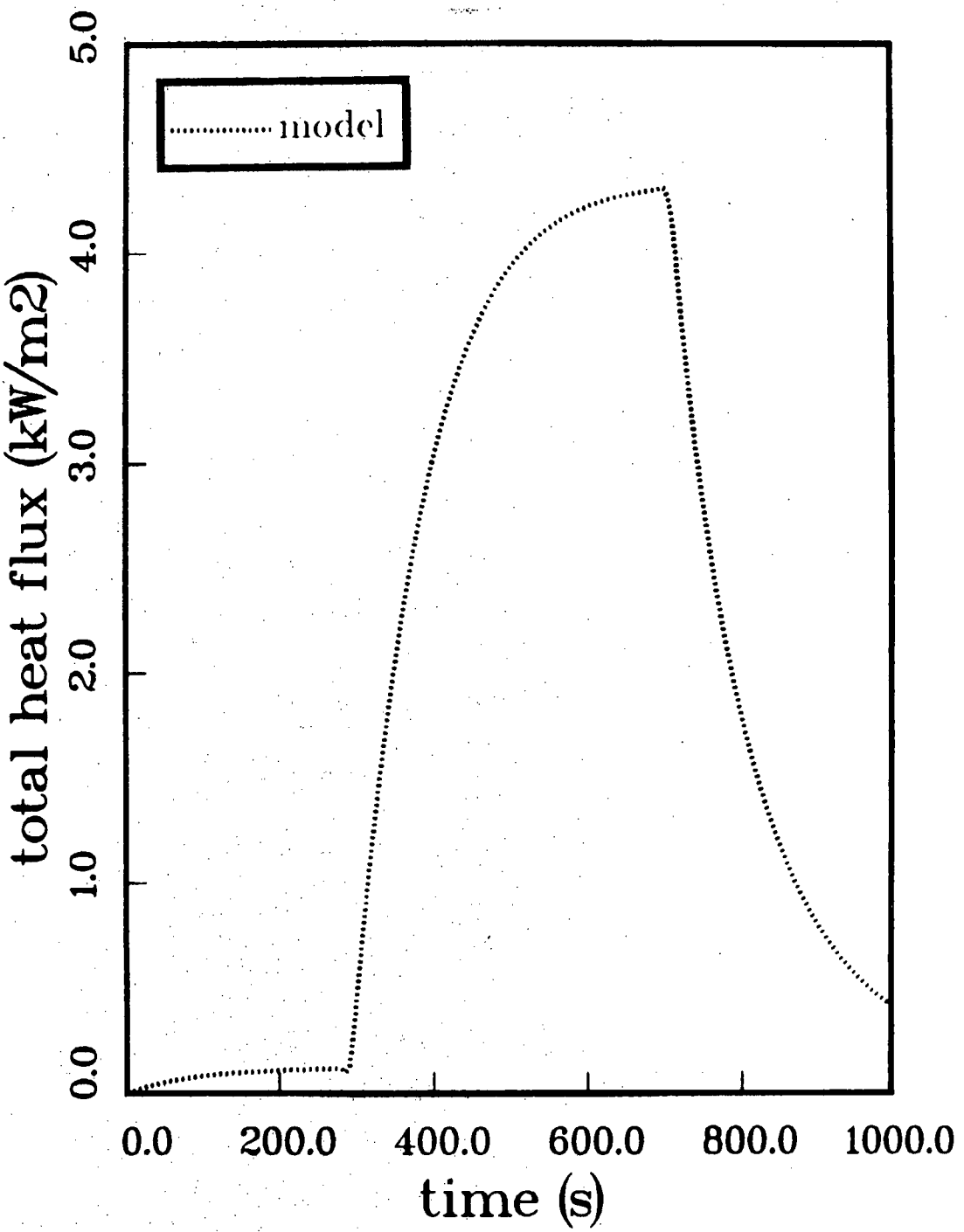

Figure 12. Computed total heat flux for test C3.

4.6 Inverse Model

In the previous section, test C3 was discussed and it was demonstrated that fairly good agreement between the model and data could be obtained if the appropriate value of the heat transfer coefficient $\mathcal{H}$ was used. In order to determine $\mathcal{H}$, a trial and error method was used. While this could be used for all of the tests, a better technique is available.

Previous work on premixed combustion[2,16,17,18] has demonstrated that the measured pressure signals can be used to infer the total heat fluxes. If the total flux is known and the radiative portion can be estimated, then it is possible to compute the convective flux by subtraction. Knowing either the measured or estimated gas temperature, the convective heat transfer coefficient can then be computed. This powerful "inverse" technique has been used to reduce data from numerous experiments including the premixed tests at NTS.

It is possible to extend the inverse method to continuous–injection tests, compute average total fluxes, and estimate convective heat transfer coefficients as a function of time. That extension is discussed below.

4.6.1 Model Formulation

The inverse method is based on using the pressure signal and its derivative to determine the mean gas temperature and temperature derivative. Writing the ideal gas law as

$$pV = N\tilde{R}T$$

where N is the number of moles and $\tilde{R}$ is the universal gas constant (8314 J/kg mol-K). Consequently, the time derivative of gas temperature for a constant–volume system is

$$\frac{dT}{dt} = T\left(\frac{1}{p}\frac{dp}{dt} - \frac{1}{N}\frac{dN}{dt}\right) \tag{25}$$

In terms of the constituent species masses M_i and the molecular weights W_i, the total number of moles can be expressed as

$$N = \sum_{vessel} \frac{M_i}{W_i} \tag{26}$$

and the time derivative is

$$\frac{dN}{dt} = \sum_{vessel} \frac{1}{W_i}\frac{dM_i}{dt}. \tag{27}$$

Using this expression to compute the temperature derivative, the previously derived gas energy equation can be used to compute the rate of heat loss from the gas

$$Q = Q_f - \dot{M}RT_{jet} - Vc_g\frac{dT_g}{dt} \tag{28}$$

The gas thermodynamic state can be used to estimate the radiative heat transfer rate from Eq. 13. Convective heat transfer rates are computed as

$$Q_{conv} = Q - Q_{rad}$$

A convective heat transfer coefficient can then be calculated as

$$\mathcal{H} = \frac{Q_{conv}}{A(T_g - T_v)}$$

In order to estimate Q_{rad} and compute $\mathcal{H}$, the vessel wall surface temperature must be known. This means that the wall energy equation must be solved simultaneously with the gas energy and species equations, just as in the direct version of the model.

4.6.2 Data Handling

The key to successful use of the inverse model is computing sufficiently smooth, but realistic, derivatives of the pressure signals. It is well known that computing derivatives from discrete and possibly noisy data is an ill–posed problem. That is, the answer does not depend on the initial data in a unique and well-behaved fashion. Some care is needed to eliminate this problem without smoothing the initial data excessively.

The data were recorded as a set of time–value pairs at fixed time increments. Quite often the data contained a number of redundant points since the sampling rate was far from optimal for most of the test. The first operation on the data was to remove the redundant points and reduce the size of the data set. Following this step, from 200–700 data points remained. These remaining points were fit to a cubic spline with the least–squares routine EFC from the SLATEC mathematical library.[14]

A spline is a continuous function composed of individual polynomials joined together at points known as knots. Depending on the order of the spline, the function and the first n derivatives of each polynomial on either side of a knot must match when evaluated at the knot point. This insures the "smoothness" of the resulting curve. By using a large number of individual polynomials (*i.e.*, knots), splines can also fit rather arbitrary data quite well. The polynomial coefficients are determined by using a linear least–squares fitting procedure and the given constraints at the knot points.

Using from 20 to 30 knots, the pressure data were fit with a cubic spline, *i.e.*, a spline composed of 3rd–order polynomials. The derivative of the spline was computed analytically and the resulting expression evaluated to obtain the time derivative at any point. Standard B-spline evaluation routines were used to perform this task. In order to obtain a good fit near the beginning and end of the burn, where kinks occur in the pressure signals, a higher concentration of knots was used and multiple knots were placed at the kinks. A multiple knot relaxes the requirement of continuity of the

highest–order derivative at that point and makes sharp changes in the signal derivative easier to fit. A simple interactive program was written to facilitate performing this task and an example of the data together with a spline fit is shown in Fig. 13.

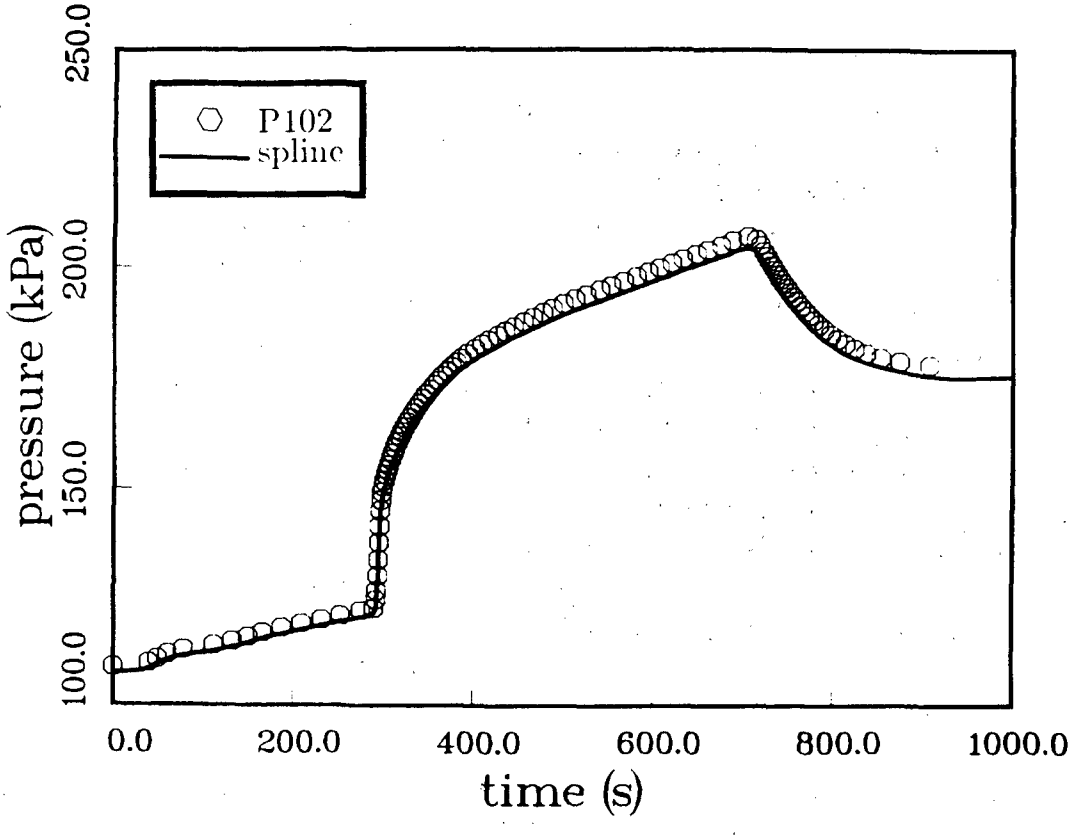

Figure 13. Raw data and spline fit for test C3 pressure signal

4.6.3 Example: Test C3

An example of the application of the inverse method is given for test C3. Model parameters and test conditions are as given above for the direct simulation. Although the main product of the inverse method is the heat transfer rate and convective heat transfer coefficient, the gas thermodynamic state is also computed. Results are shown in Figs. 14-17.

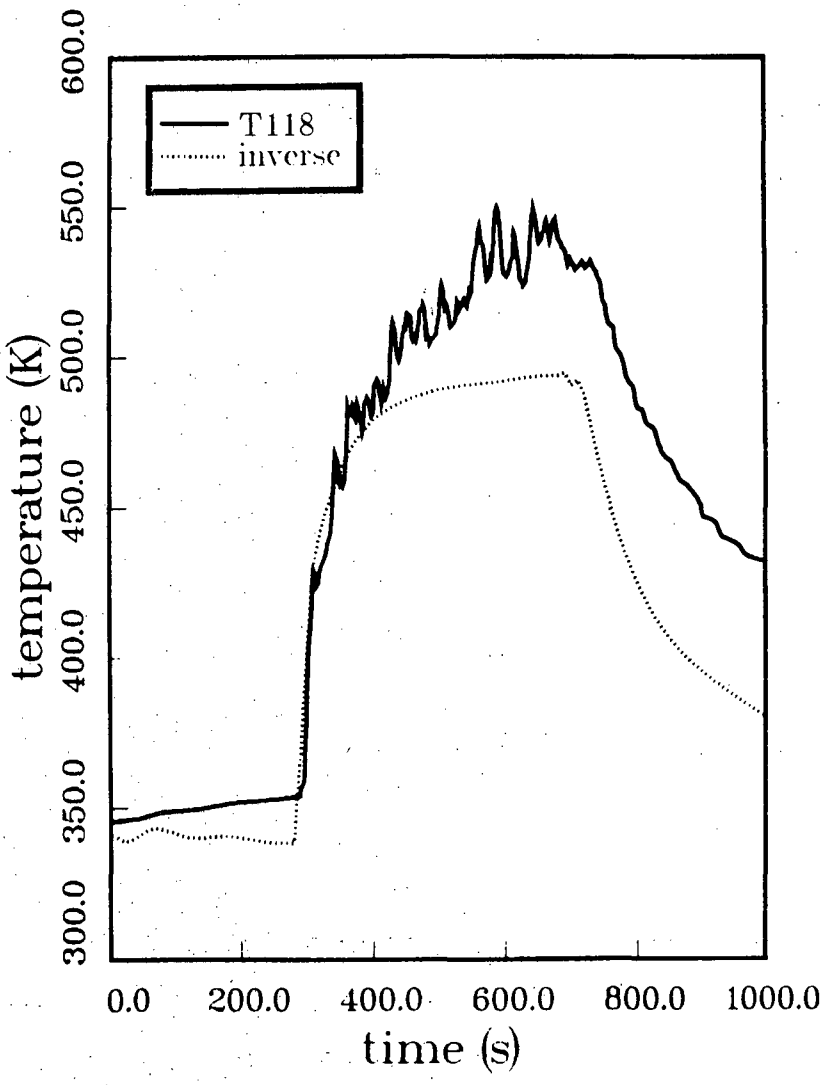

Figure 14. Measured (T118) and computed (inverse method) gas temperature for test C3

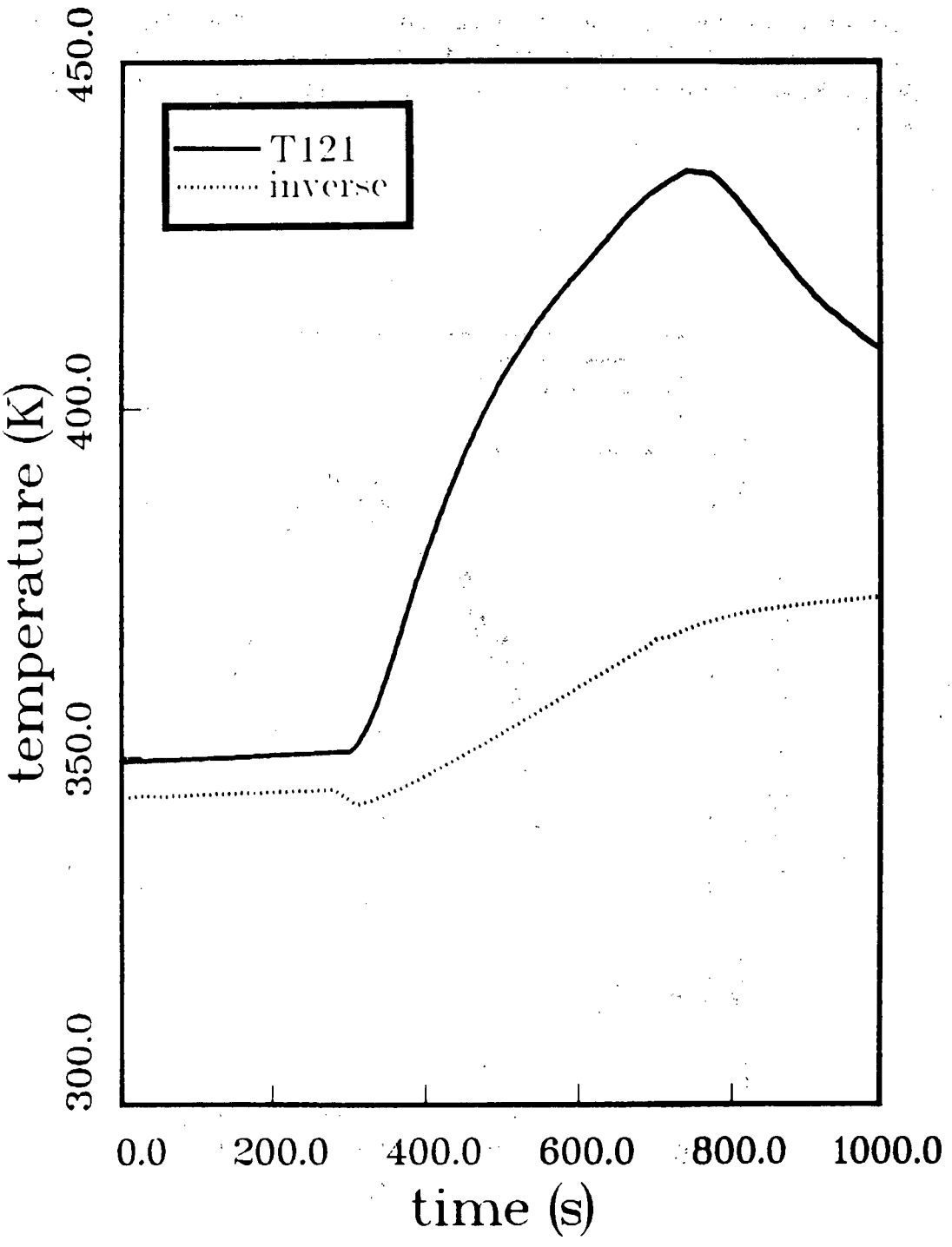

Figure 15. Measured (T121) and computed (inverse method) wall temperature for test C3

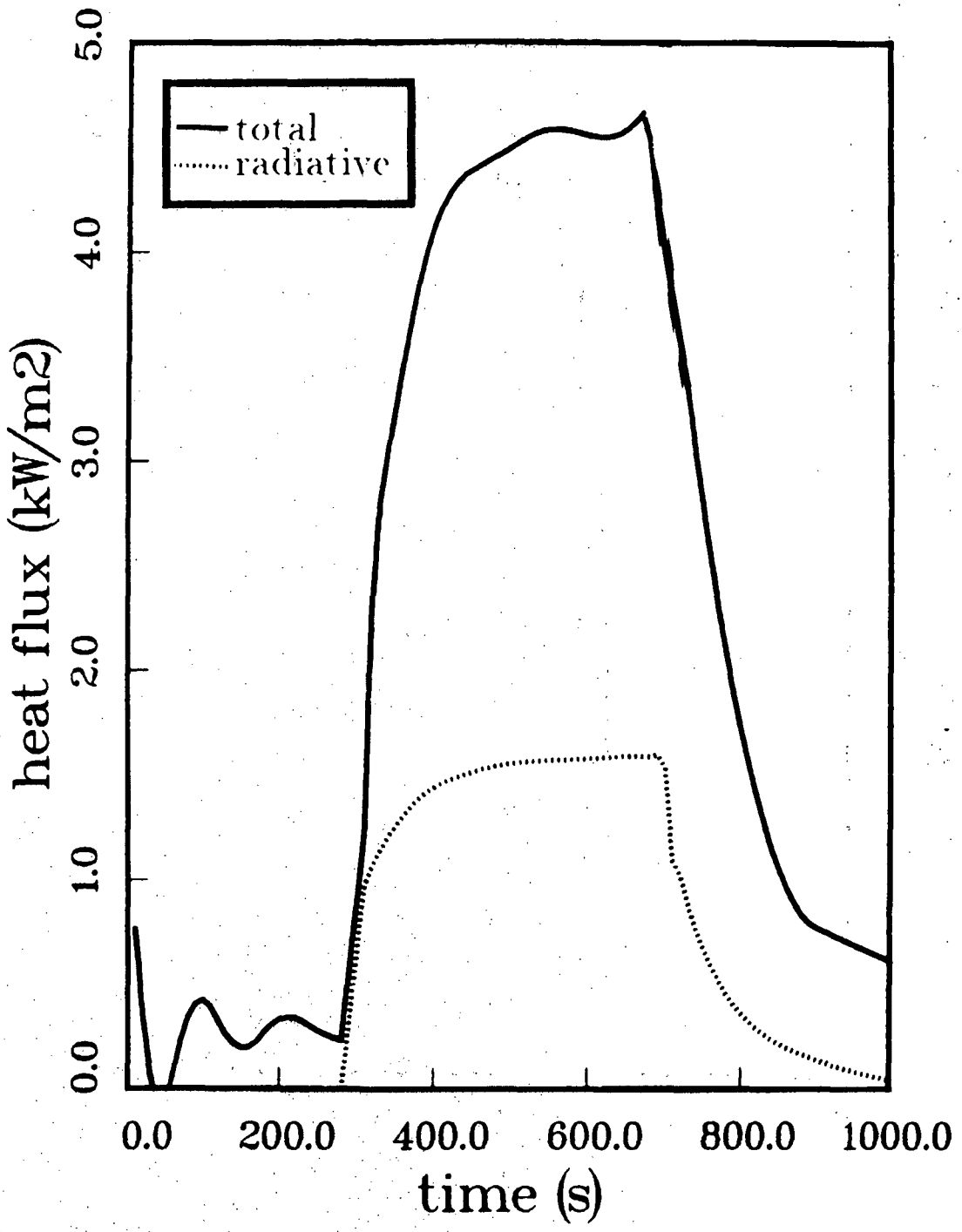

Figure 16. Computed (inverse method) total wall heat fluxes for test C3

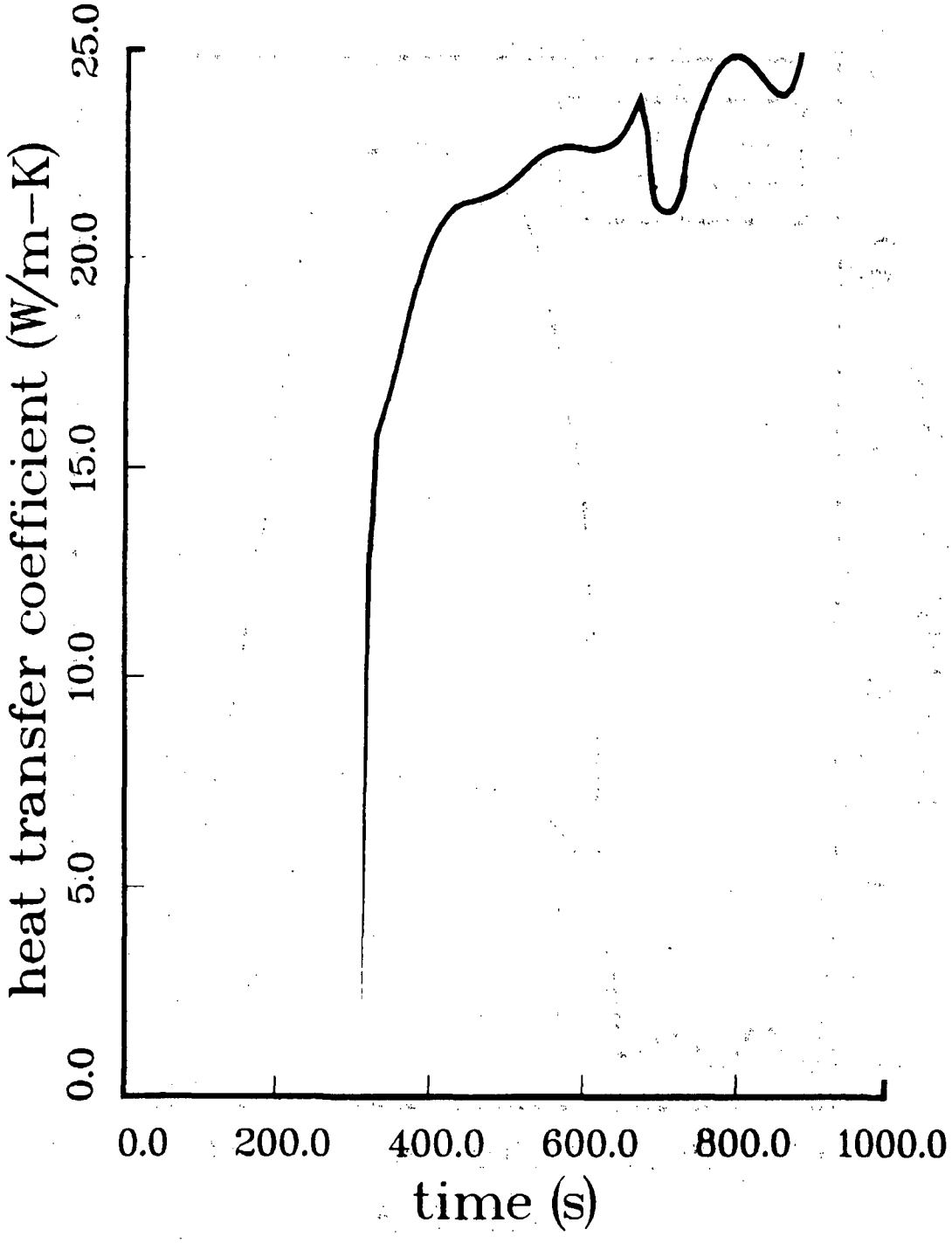

Figure 17. Computed (inverse method) convective heat transfer coefficient for test C3

5 Results

This section compares test results in the framework of the model presented in the previous section and discusses the results of the inverse modeling for heat transfer. First, the effect of fans and sprays are discussed. Second, the effect of varying the nozzle size on the average heat transfer coefficient is discussed. Third, the nonuniformity of the heat transfer is discussed and the magnitude of the stagnation–point heat transfer rate is estimated.

5.1 Sprays and Fans

Three tests were conducted with nearly identical source parameters: C1 is the baseline case, no fans or sprays; C2 is the spray case; C3 is the fan case. All tests were conducted with the 1 m diameter diffuser source and nominal flowrates of 1.8 kg/min hydrogen and 27 kg/min steam. A comparison of the gas pressures for all three cases is shown in Fig. 18.

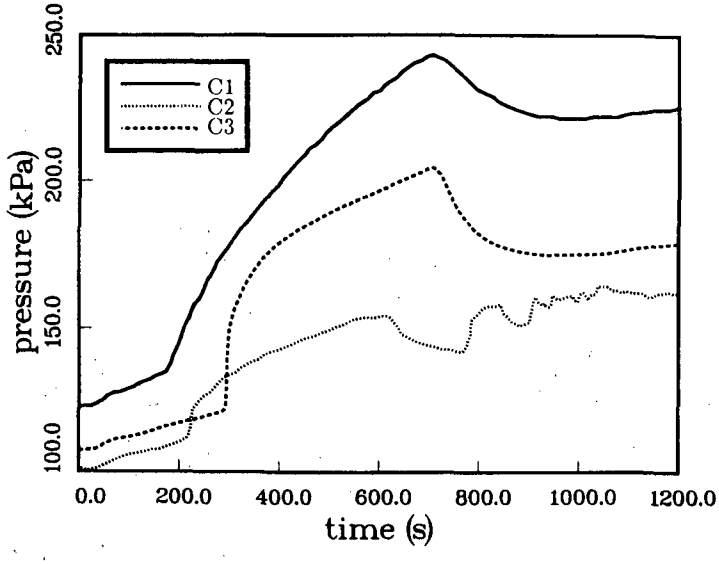

Figure 18. Gas pressures for tests C1, C2, and C3.

Sprays are clearly the most effective in enhancing the heat transfer. Peak pressures and temperatures were lower in test C2 than in either C1 or C3. Fans significantly increase the heat transfer coefficient, consequently the peak temperature and pressure for test C3 are lower than those observed in test C1. A clear region of "quasi-steady" heat transfer is observed in C3, this region does not appear in C1.

5.2 Nozzle Size Effect

Three tests were carried out with almost identical flowrates of hydrogen and steam and three different source diameters D: C1, D = 1 m; CN1, D = 0.13 m; CS1, D = 0.038 m. Flowrates were nominally 1.9 kg/min hydrogen and 28 kg/min steam. The effect of nozzle diameter is quite apparent in the comparison shown in Fig. 19. Decreasing the nozzle diameter at a fixed flowrate has the effect of increasing the heat transfer coefficient. This is due to the increase in the importance of the initial jet momentum as the nozzle diameter decreases, *i.e.*, the Froude number increases. The momentum injected into the vessel by the source results in increased bulk gas motion (circulation) and increased dissipation in the boundary layer regions near the vessel walls. Both processes increase the heat transfer coefficient.

A simple model can be used to predict the change in heat transfer coefficient with source parameter variations. This model uses the extended Reynolds' analogy between Stanton number St and skin friction coefficient C_f:

$$St = \frac{\mathcal{H}}{\rho u c_p}; \qquad C_f = \frac{\tau_w}{\frac{1}{2}\rho u^2}.$$

For laminar flow,[19] the analogy is:

$$St = \frac{C_f}{2Pr^{2/3}},$$

where Pr is the Prandtl number. For turbulent flow,[19] a useful empirical correlation is Kármán's formula

$$St = \frac{C_f}{2Pr^{0.4}\left(\frac{T_w}{T_e}\right)^{0.4}},$$

where T_w is the wall temperature and T_e is the freestream temperature. In order to use these analogies between heat and momentum transfer, I will assume that all of the momentum injected into the vessel is dissipated at the walls of the vessels. Since I am only interested in obtaining a scaling relationship, the simpler laminar formula will be used.

The analysis is particularly simple for jet–like sources which have a constant momentum flux J. Plumes require a more sophisticated analysis since the momentum flux increases due to the effect of buoyancy accelerating the source fluid. For a jet, the initial source momentum is $J = \rho U^2 A_j$ and the shear stress at the wall τ_w can be estimated as J/A_w, where A_w is the heat transfer surface area of the vessel wall. Substitution into the extended Reynolds' analogy yields the following expression for the heat transfer coefficient $\mathcal{H}$

$$\mathcal{H} \sim \frac{c_p J}{u_w A_w}$$

where u_w is the characteristic circulation velocity in the vessel. A simple estimate for u_w is $u_w \sim L/T$ where L is the height of the vessel and T is the turnover time. Turnover time can be estimated as the total mass in the vessel M_v divided by the total plume or jet entrainment rate $\dot{M}_e$, $T \sim M_v/\dot{M}_e$. The value of the time T is typically an order of magnitude smaller than the time T_{BT} computed for a nonburning plume in Section 3 above.

If a jet entrainment law is used, *i.e.*, $M_e \sim L\sqrt{\rho_v J}$, the heat transfer coefficient is approximately

$$\mathcal{H} \sim \frac{c_p}{L}\sqrt{\rho_v J}.$$

For a fixed mass flowrate and vessel size, this implies that the heat transfer coefficient scales as $\mathcal{H} \sim A_j^{1/2} \sim D^{-1}$. While there are not enough data points to confirm the exact power of D in this relationship, a dependence on the inverse power of D is clearly indicated by the data. In order to check the relationship between source momentum and average heat transfer coefficient more closely, I have analyzed additional tests with the inverse model. The results are given in Table 9.

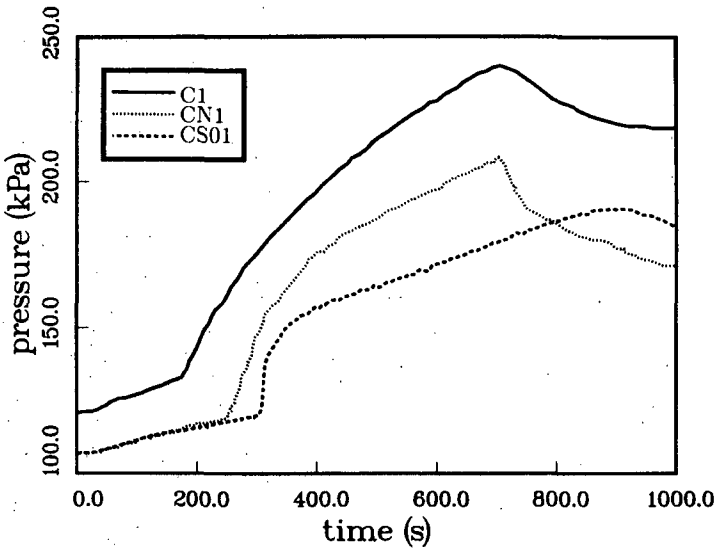

Figure 19. Gas pressures for tests C1, CN1, and CS1.

Table 9. Inverse Model Results

Quantity		Test C3	C8	CS1	CS5
Computed Peak Values					
Q_f	(MW)	3.5	2.8	3.6	3.6
q	(kW/m^2)	4.6	4.5	4.6	4.6
h	(W/m^2-K)	23	60	50	22
T_g	(K)	490	410	440	500
T_w	(K)	375	372	388	370
Measured Peak Values					
q^a	(kW/m^2)	-	-	17	10
T_g^b	(K)	623	490	475	580
T_w^c	(K)	463	425	415	500
T_w^d	(K)	433	398	395	430

[a]Heat flux gauge H503
[b]Gas thermocouple T101
[c]Wall thermocouple T120
[d]Wall thermocouple T121

Notable are the following points: The maximum heat transfer rates predicted by the inverse computations are lower by a factor of two or three than those measured by the Schmidt-Boelter gauge H503. This is an indication of the nonuniformity of heat transfer. This observation is supported by the difference between calculated and measured wall peak temperature. The differences between the two measured wall temperatures are due to the wall jet and its influence on the heat transfer (see the following discussion on stagnation point heat transfer).

The heat transfer coefficients inferred from the inverse technique indirectly support the scaling hypothesis discussed above. Although test CN1 was not analyzed, comparison of the pressure data with those for test C3 (see Fig. 20) show that the results for the two tests are almost identical. Since the source parameters and initial conditions are identical, the heat transfer coefficients should be the same, $\mathcal{H} \sim 23$ W/m^2-K. The coefficient for test CS1, which has corresponding initial conditions and the same source parameters as CN1 except the nozzle diameter is smaller by a factor of 3.3, is 50 W/m^2-K. The ratio of heat transfer coefficients is 2.2 *vs* 3.3 for the inverse source diameter ratio. The agreement is probably satisfactory in view of the idealized nature of the theory.

Comparison of tests CS1 and CS5 yields similar support for the scaling hypothesis. Test CS5 is almost identical to CS1 except the steam flowrate is 3.0 times lower in CS5 than in CS1. For a fixed nozzle diameter, the scaling hypothesis implies that the heat transfer coefficient should vary directly as the mass flowrate. For test CS5, $\mathcal{H} \sim 22$ W/m^2-K, 2.3 times lower than in test CS1. Again the agreement is probably satisfactory. The scaling arguments have not been applied to the plume-like flows such as test C1. Two complications arise in these cases: plume entrainment laws must be used; the role natural convection plays must be assessed.

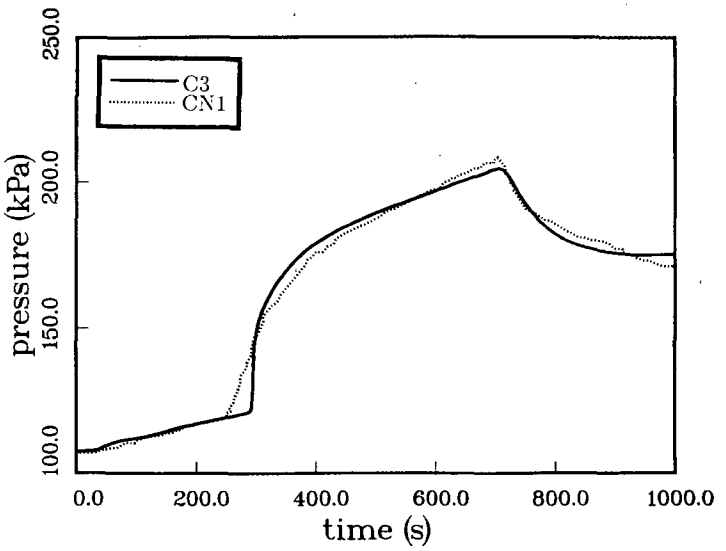

Figure 20. Gas pressures for tests C3 and CN1.

5.3 Stagnation–Point Heat Transfer

As mentioned above, the peak heat transfer rates occur at the top of the vessel where the jet or plume impinges. We have chosen not to include this effect in the present model since few data were obtained in that part of the vessel. It is useful to estimate the peak heat transfer rates that did occur since they represent limiting conditions for equipment survival. This effect could also explain the systematic differences between wall temperature measurements.

Heat transfer above fires, both jets and plumes, has been studied extensively in the last two decades. Most investigations[20,21,22] have been concerned with impingement on flat ceilings; limited data on jet flows[23] and analytical results for laminar flows indicate that the curvature of the surface will affect the results. This will be neglected in the discussion below.

Plume flows have been extensively investigated. The heat transfer coefficient along the wall can be expressed as a nondimensional function of the nondimensional distance X/H where X is the coordinate along the wall and H is the height above the source. The heat transfer coefficient is given as a normalized quantity $\acute{h}_c$ that resembles a Stanton number based on an idealized plume velocity:

$$\acute{h}_c = \frac{\chi}{\rho c_p \sqrt{gH} Q_H^{*1/3}}; \qquad Q_H^* = \frac{Q_f}{\rho c_p T \sqrt{gH} H^2}$$

The variation of $\acute{h}_c$ with X/H is shown in Fig. 21 together with the approximate locations of the wall thermocouples T120 and T121.

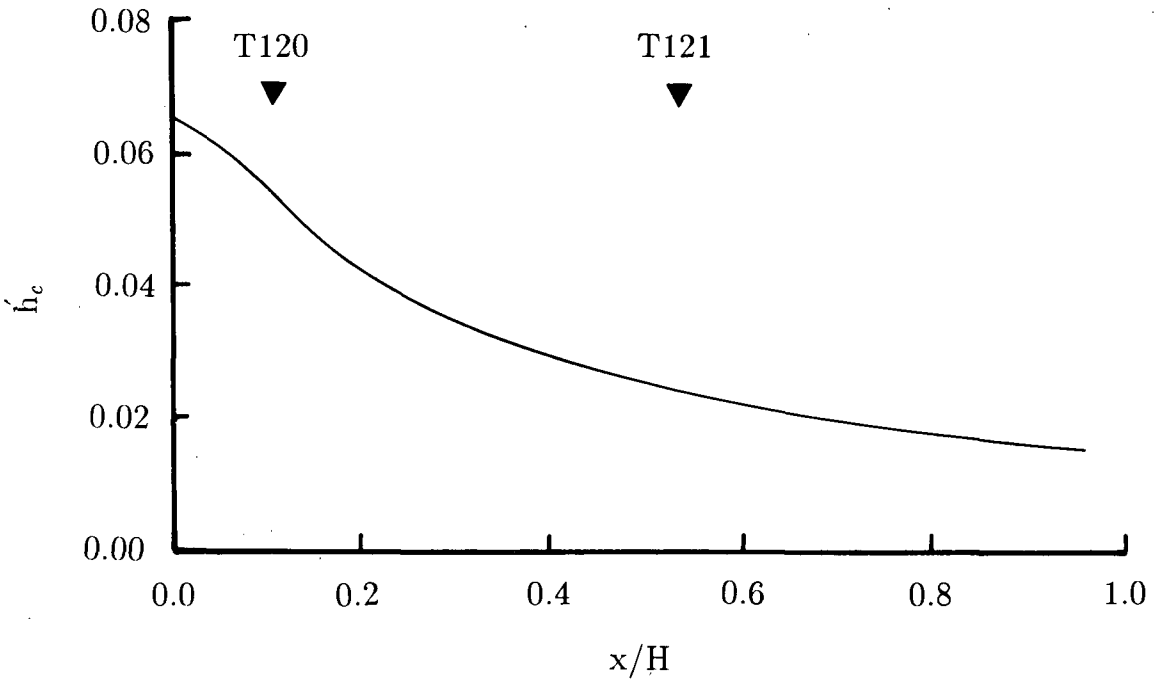

Figure 21. Nondimensional heat transfer coefficient $\acute{h}_c$ *vs* nondimensional wall coordinate X/H. From Sargent.[22]

The magnitude of the actual heat transfer coefficient and the resulting heat flux have been computed for test C1 assuming a cold wall: $\mathcal{H} = 127$ W/m^2-K and $q_c = 8.6$ kW/m^2. The value of q_c is appropriate for the beginning of the transient and will increase with time as the background gas temperature in the vessel increases. Near the end of the burn, this value could be up to 4 times larger. On the other hand, the average heat transfer coefficient and heat flux for test C1 must certainly be less than those values obtained for test C3: $\mathcal{H} = 23$ W/M^2-K and $q_c = 5$ kW/m^2. This indicates that the peak stagnation heat flux and heat transfer coefficient can be up to 5-6 times larger than the average values for tests with low Froude number sources. Using correlations appropriate for jet flames,[24] similar conclusions are reached for those tests.

6 Summary

I have discussed several aspects of the NTS continuous–injection tests and given a brief summary of the data. Key areas mentioned are: mixing during the injection process; the role of convective heat transfer in determining the gas pressure and temperature; experimental determination of the average heat transfer coefficient; the effect of the wall jet and stagnation region on predicting wall temperatures.

The source Froude number has a profound influence on the degree of mixing during the injection process. The various types of ignition behavior can be related to the Froude number and igniter location. The lack of multiple deflagrations and the phenomenon of nonignition can be explained on this basis. Tests using a buoyant plume source probably have a strongly stratified initial hydrogen concentration and a distinct moving front will exist between mixed and unmixed fluid. As the source Froude number increases, the vessel contents become better mixed. Tests using jet–like sources (large source Froude numbers) will exhibit good mixing and a distinct front will not form.

A simple model for the thermodynamics and heat transfer is proposed. This model is solved analytically for an idealized case and the results are used to discuss the test data. Numerical results of a detailed implementation of the model are compared to a single test, C3. This simulation demonstrates that the model can accurately predict gas temperatures and pressures if the convective heat transfer coefficient is chosen correctly. Major conclusions of the model are that the wall-gas temperature difference reaches a constant value after an initial transient and that the total heat flux depends only on the fire power, vessel, and atmosphere heat capacities.

The model is inverted and used to infer average convective heat transfer rates to the vessel. Convective heat transfer is shown to increase with the source momentum or Froude number. A simple momentum conservation analysis is used to deduce the scaling of heat transfer with the jet momentum. Heat transfer coefficients determined by the inverse computation appear to scale as the square root of the jet momentum, in satisfactory agreement with the simple scaling model.

The data are compared to measured and estimated stagnation–point heat transfer rates. These comparisons indicate that the heat transfer rate in the stagnation region can be up to 5 times larger than the average value. Expected variations in heat transfer rate near the stagnation point could account for the observed systematic variation in wall thermocouple measurements.

References

1. R. T. Thompson, R. C. Torok, D. S. Randall, J. S. Sullivan, L. B. Thompson, and J. J. Haugh 1985 "Large–Scale Hydrogen Combustion Experiments" EPRI Report NP-3878 for Research Project 1932-11, Vols. 1 and 2.

2. A. C. Ratzel 1985 *Data Analysis for Premixed Combustion Tests Performed at the Nevada Test Site (NTS)* Sandia National Laboratories Report SAND85-0135, NUREG/CR-4138.

3. W. D. Baines and J. S. Turner 1969 "Turbulent buoyant convection from a source in a confined region" *J. Fluid Mech.* **37**, 51-80.

4. J. S. Turner 1962 "The 'starting plume' in neutral surroundings" *J. Fluid Mech.* **13**, 356-368.

5. J. E. Shepherd, M. R. Baer, and J. C. Cummings 1984 "Fluid Motion Induced by Filling Containers" Bull. Am. Phys. Soc. **29**(9), abstract EF4.

6. P. A. Thompson 1972 **Compressible-Fluid Dynamics**, McGraw–Hill, NY, 41.

7. J. E. Broadwell, W. J. Dahm, and M. D. Mungal 1984 "Blowout of turbulent diffusion flames," *20th Symposium (Intl.) on Combustion*, The Combustion Institute, Pittsburgh, PA, 303-310.

8. E. E. Zukoski, T. Kubota, and B. Cetegen 1980/81 "Entrainment in Fire Plumes," *Fire Safety Journal* **3**, 107-121.

9. H. C. Hottel and A. F. Sarofim 1967 **Radiative Transfer**, McGraw-Hill, 460.

10. D. K. Edwards 1976 "Molecular Gas Band Radiation," in *Advances in Heat Transfer* **12**, Academic Press, NY, NY.

11. R. Siegel and J. R. Howell 1981 **Thermal Radiation Heat Transfer**, 2nd Edition, McGraw-Hill, 567.

12. E. S. Fishburne and H. S. Pergament 1980 "The Dynamics and Radiation Intensity of Large Hydrogen Fires," *17th Symposium (Intl.) on Combustion*, The Combustion Institute, Pittsburgh, PA, 1063-1072.

13. D. Burgess and M. Hertzburg 1974 "Radiation from Pool Fires," in **Heat Transfer in Flames**, Eds. N. H. Afghan and J. M. Beers, Hemisphere, 413-430.

14. K. H. Haskell, W. H. Vandevender, and E. L. Walton 1980, *The SLATEC Mathematical Subprogram Library*, Sandia National Laboratories Report SAND80-2792.

15. R. J. Kee, J. A. Miller, T. H. Jefferson 1980 *CHEMKIN: A General–Purpose, Problem–Independent, Transportable Fortran Chemical Kinetics Code Package* Sandia National Laboratories Report SAND80-8003.

16. S. N. Kempka, A. C. Ratzel, A. W. Reed and J. E. Shepherd 1984 "Post–Combustion Convection in an Intermediate Scale Vessel," in *Proc. of the Joint ANS/ASME Conference on the Design, Construction and Operation of Nuclear Power Plants*, Portland, OR, Aug. 5-7, 1984.

17. A. C. Ratzel and J. E. Shepherd 1985 "Heat Transfer Resulting form Premixed Combustion," in *Heat Transfer in Fire and Combustion Systems* (Eds. C. K Law, Y. Jaluria, W. W. Yuen, and K. Miyasaka), Publication HTD-45 of the ASME, 191-201.

18. A. C. Ratzel, S. N. Kempka, J. E. Shepherd, and A. W. Reed 1985 *SMOKE: A Data Reduction Package for Analysis of Combustion Experiments* Sandia National Laboratories Report SAND83-2657, NUREG/CR-4136.

19. F. M. White 1973 **Viscous Fluid Flow**, McGraw-Hill, 564.

20. L. Y. Cooper 1982 "Convective heat transfer to ceilings above enclosure fires," *19th Symposium (Intl.) on Combustion*, The Combustion Institute, Pittsburgh, PA, 933-999.

21. H-Z. You and G. M. Faeth 1979 "Ceiling heat transfer during fire plume and fire impingement," *Fire and Materials* **3**, 140-147.

22. W. S. Sargent 1983 "Natural convection flows and associated heat transfer processes in room fires," Ph. D. Thesis, California Institute of Technology, Pasadena, CA.

23. C. Dup. Donaldson, R. S. Snedeker, and D. P. Margolis 1971 "A study of free jet impingement. Part 2. Free jet turbulent structure and impingement heat transfer," *J. Fluid Mech.* **45**, 477-512.

24. J. E. Shepherd 1985 "Stagnation–point heat transfer from jet flames," in *Heat Transfer in Fire and Combustion Systems* (Eds. C. K Law, Y. Jaluria, W. W. Yuen, and K. Miyasaka), Publication HTD-45 of the ASME, 173-180.

A Data Plots

This appendix contains plots of selected data from each of the 15 tests. Pressure data only is given for all tests except C3, C8, CS1, and CS5. Gas and wall temperatures and some heat flux data are given for these four tests. The test designation and the instrument identification is given with each plot. Instrumentation locations are given as a function of the (x, y, z) coordinates within the vessel in the table below. The coordinates are defined in Fig. 2 of the main text.

Table A-1. Instrument Locations

Instrument	Location $(x, y, z)^a$
Gas thermocouple (3-mil)	
T101	1,-2,19
T102	-1,-1,1
Gas thermocouple (32-mil)	
T114	9,0,21
T118	20,0,0
Wall thermocouple (32-mil)	
T120	-2,-3,26
T121	-18.4,1,18.4
Heat flux gauge (total)	
H503	1,-2.5,2
Gas pressure transducer	
P102	-5,-5,0

[a]Units are feet.

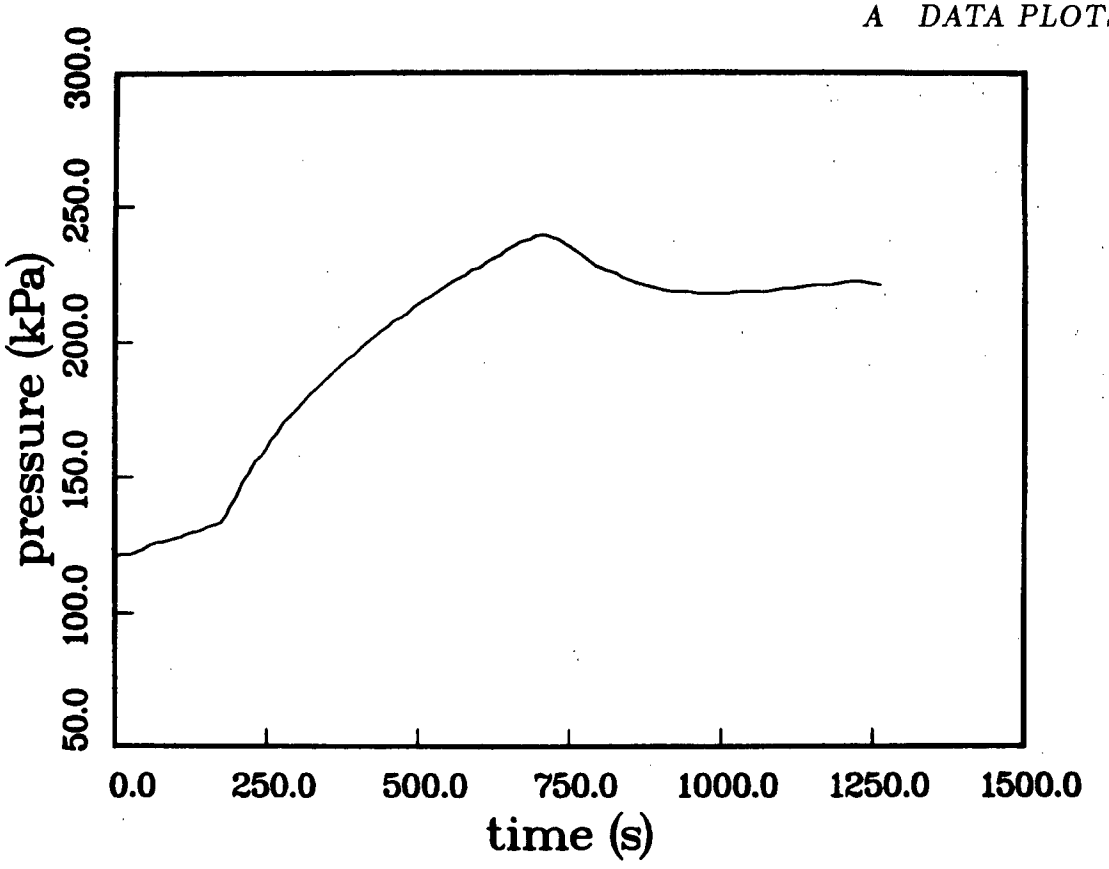

Figure A-1. Test C1, gas pressure P102.

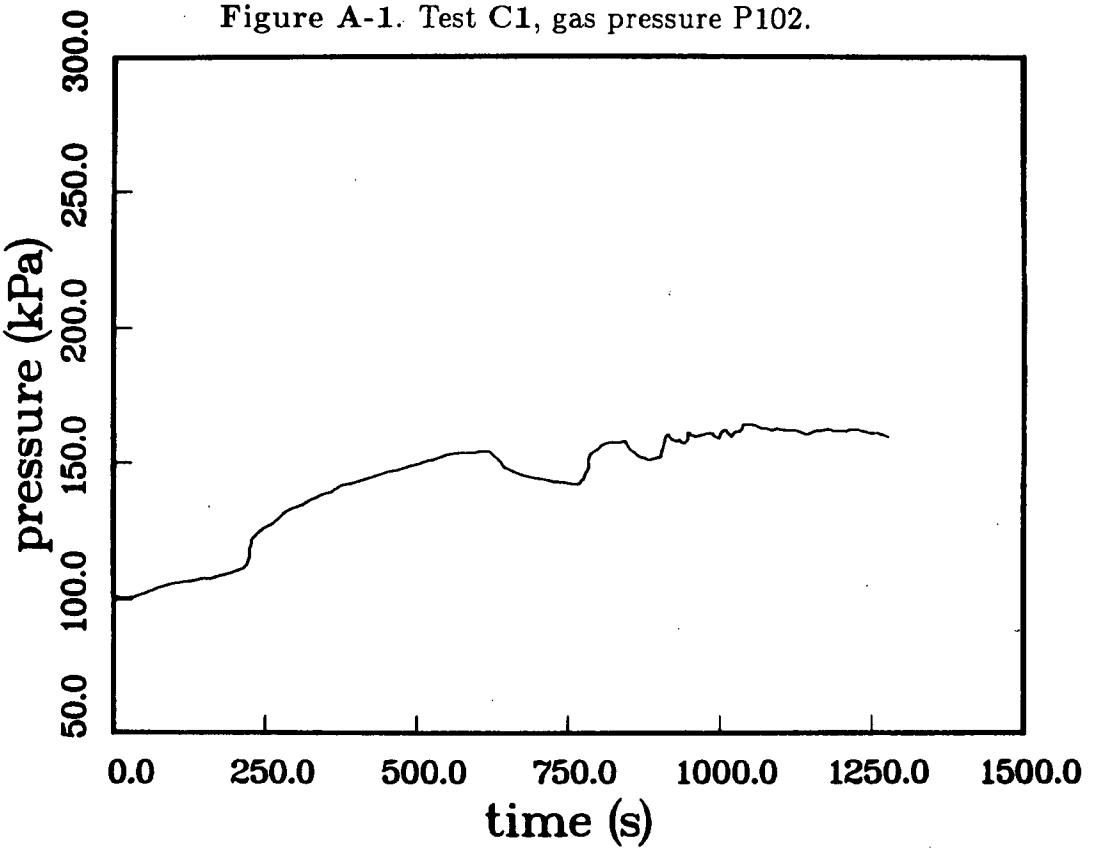

Figure A-2. Test C2, gas pressure P102.

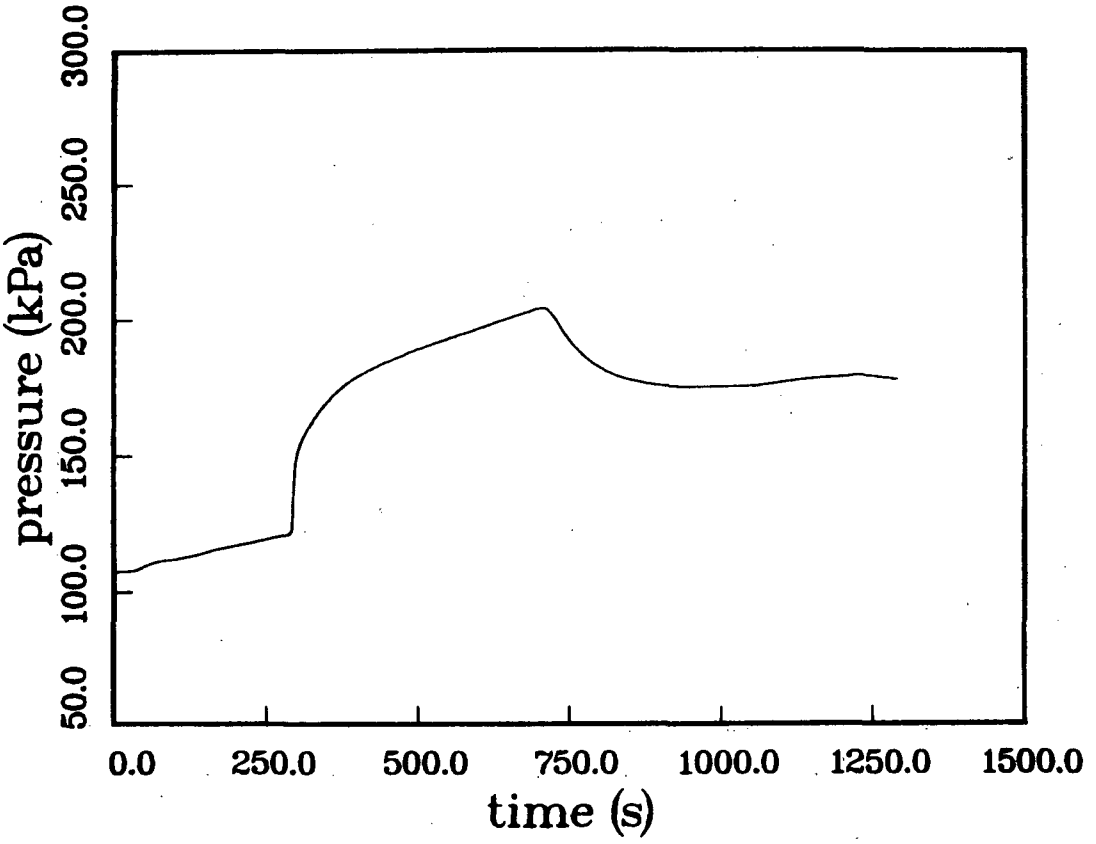

Figure A-3. Test C3, gas pressure P102.

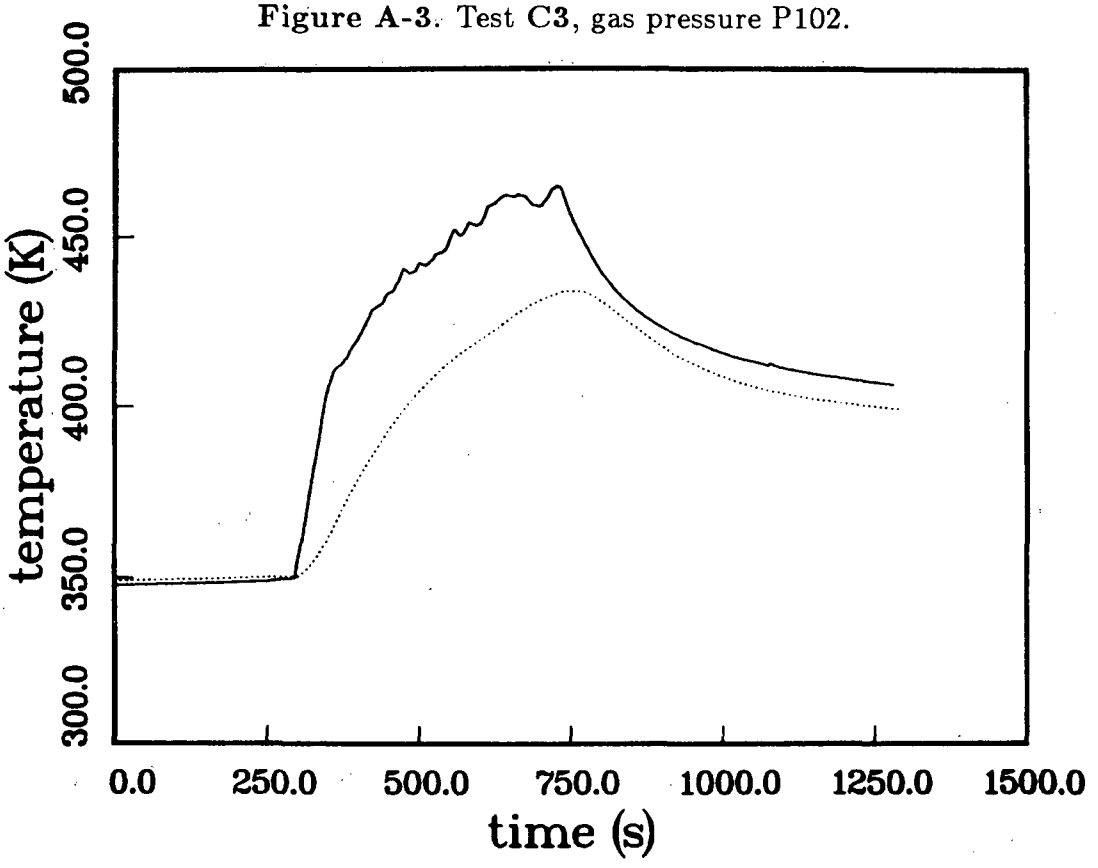

Figure A-4. Test C3, wall temperatures T120, T121.

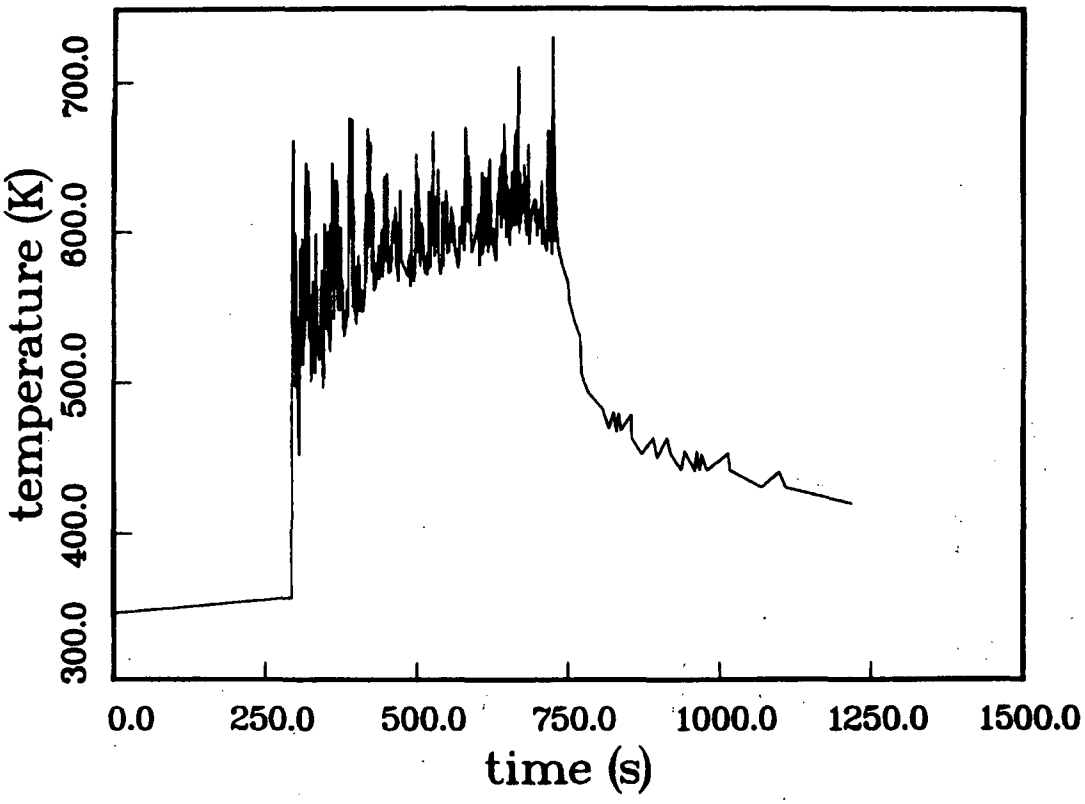

Figure A-5. Test C3, gas temperature T101.

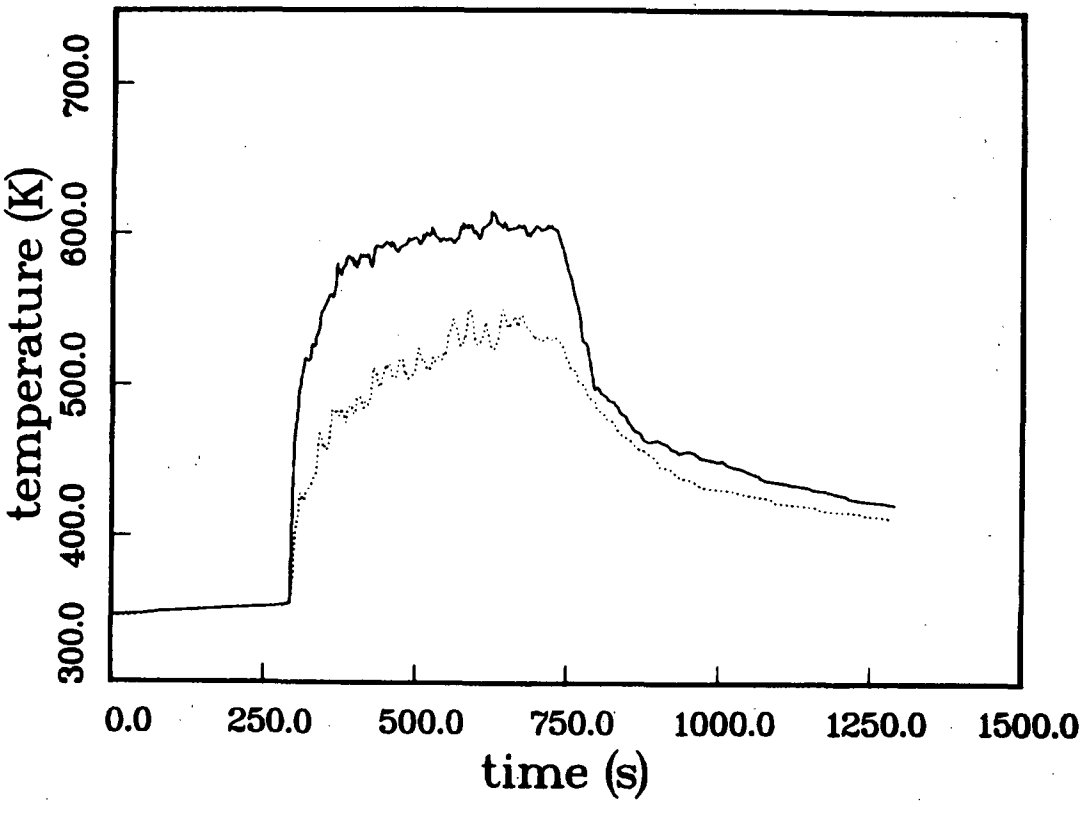

Figure A-6. Test C3, gas temperatures T114, T118.

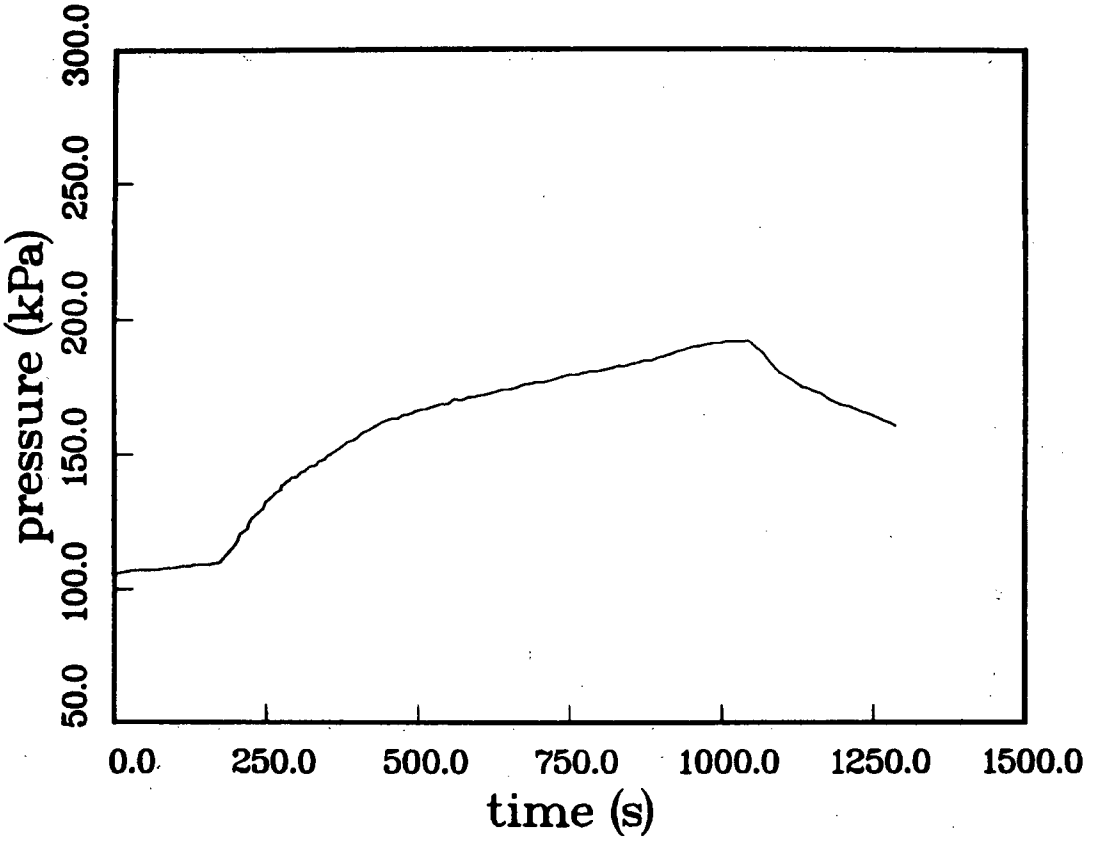

Figure A-7. Test C5, gas pressure P102.

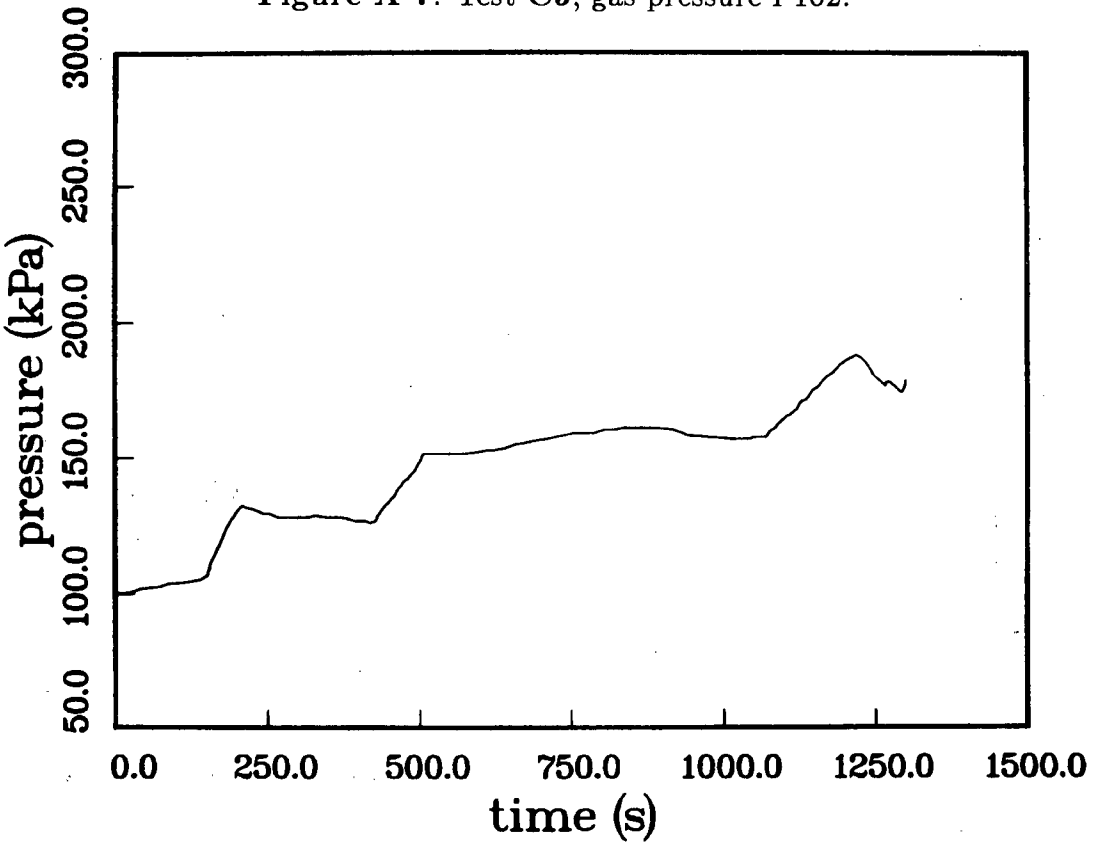

Figure A-8. Test C7, gas pressure P102.

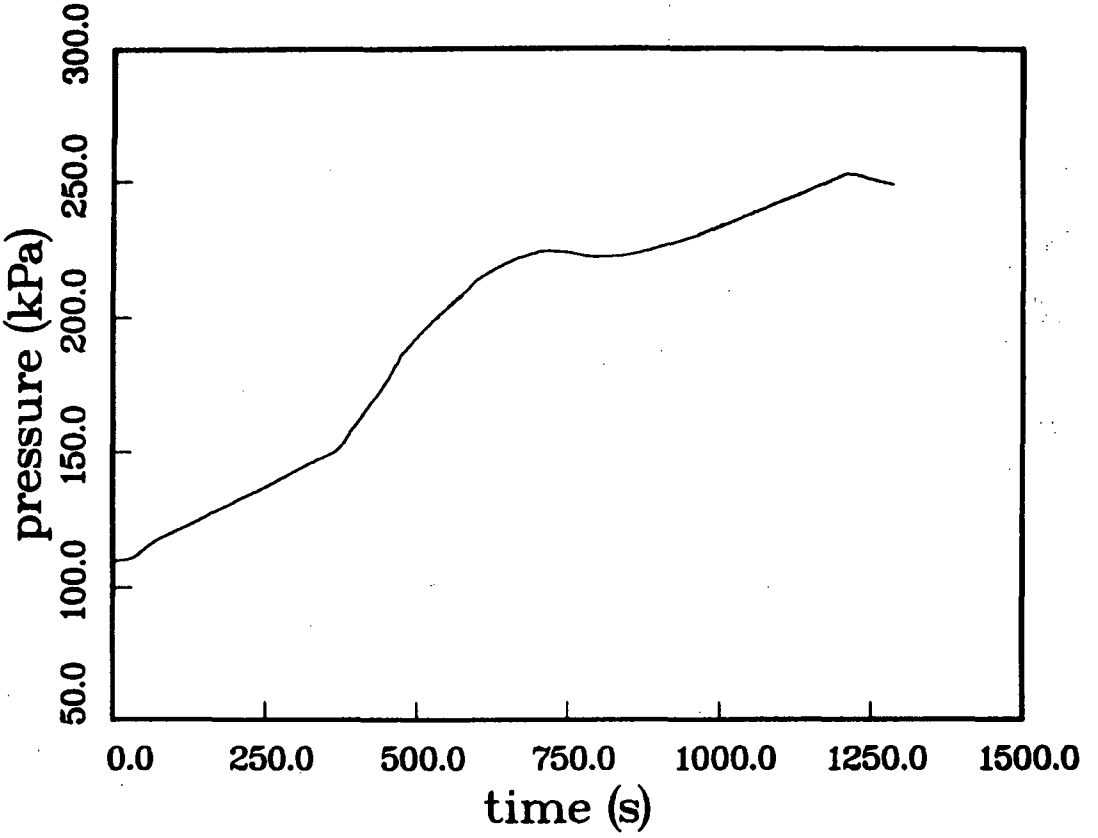

Figure A-9. Test C8, gas pressure P102.

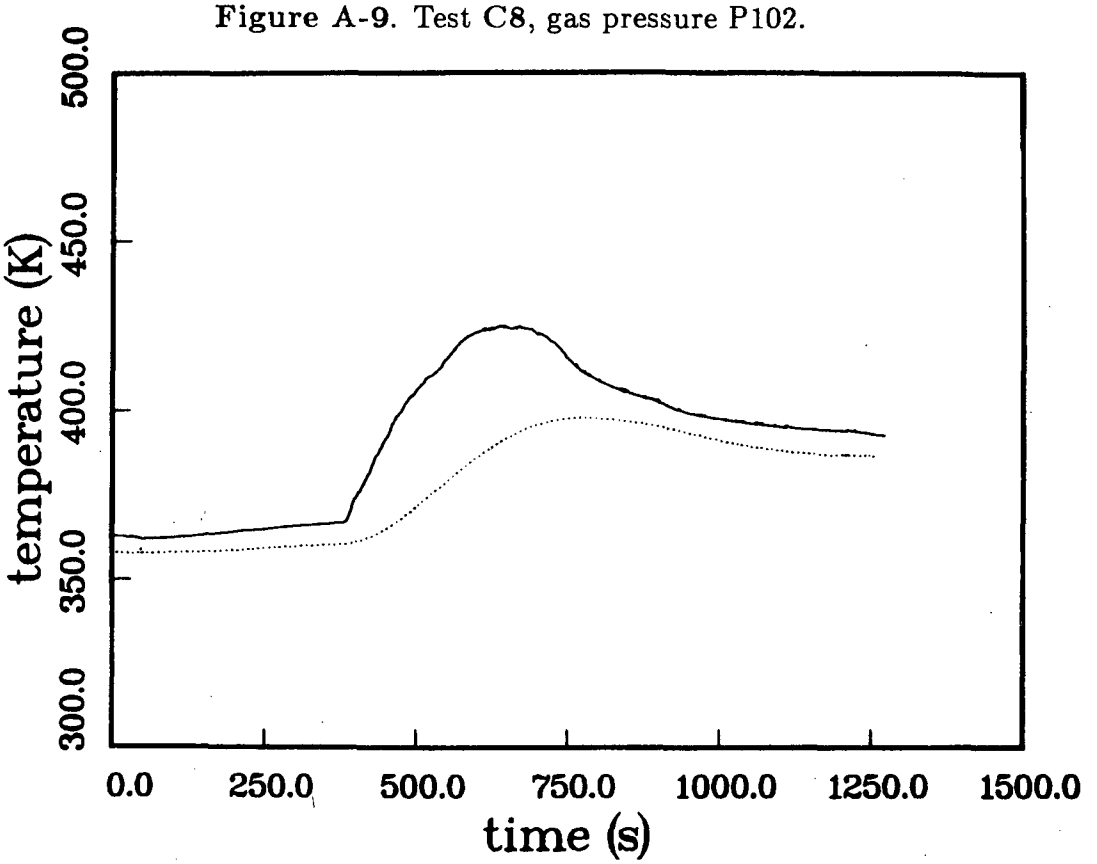

Figure A-10. Test C8, wall temperatures T120, T121.

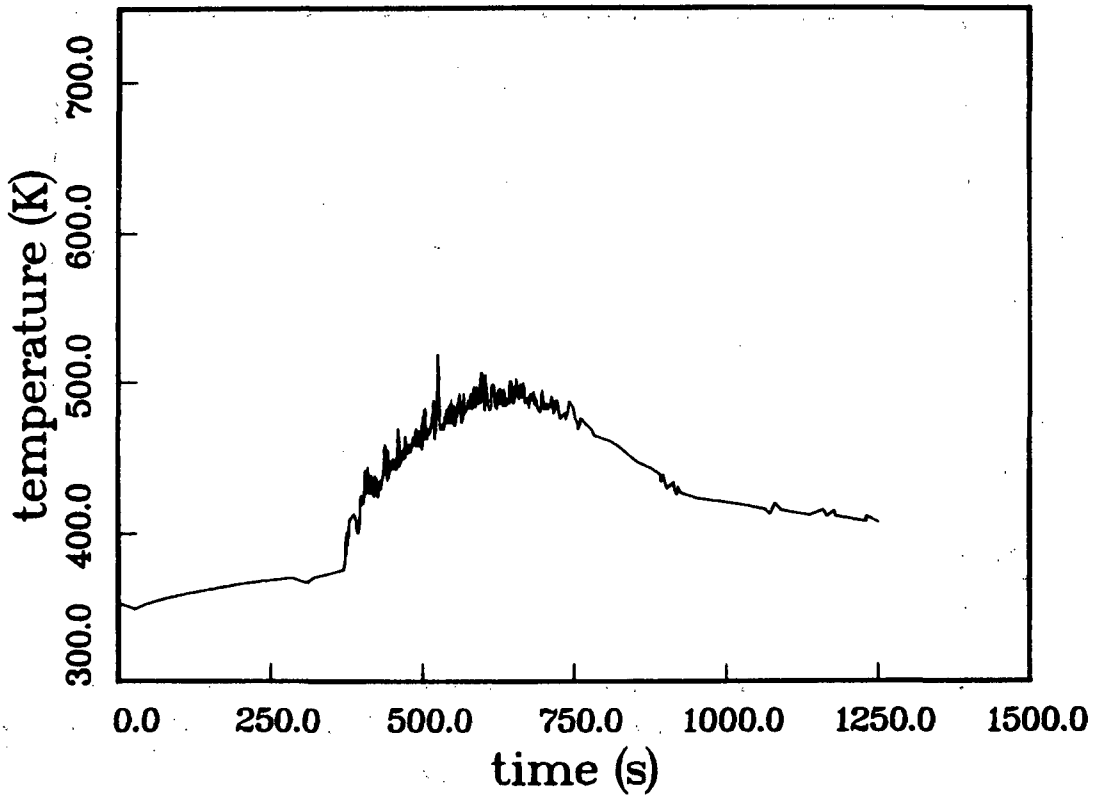

Figure A-11. Test C8, gas temperature T101.

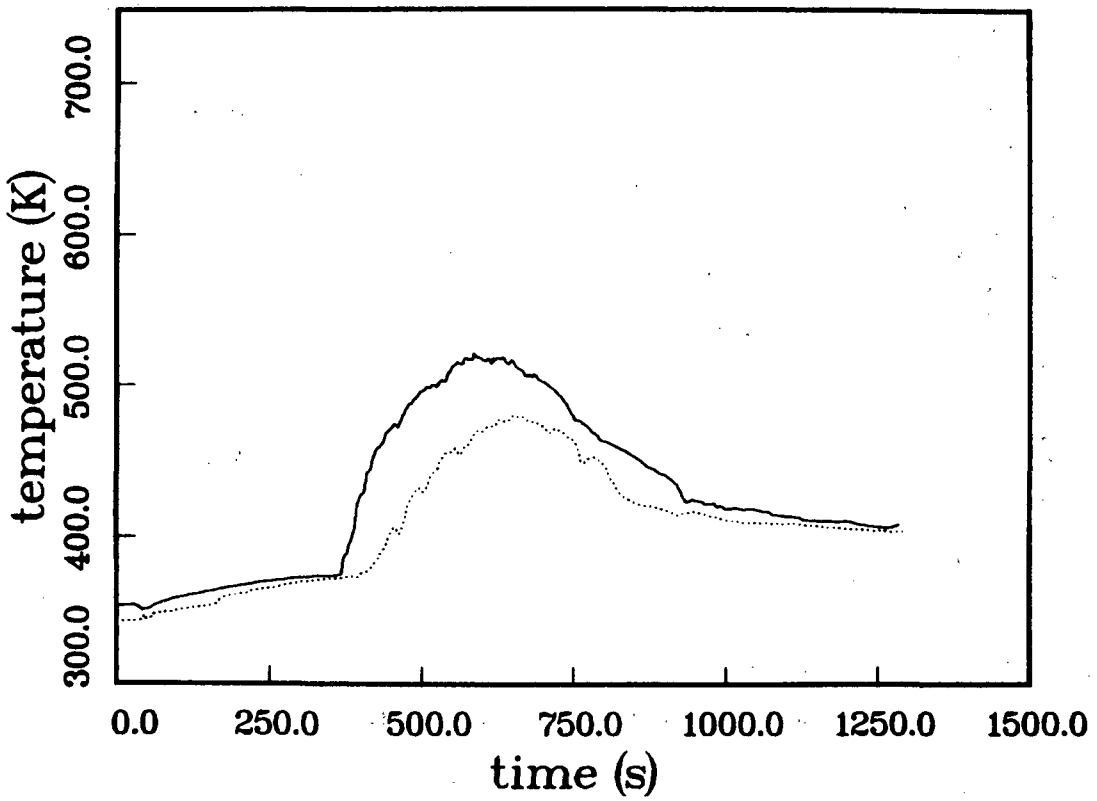

Figure A-12. Test C8, gas temperatures T114, T118.

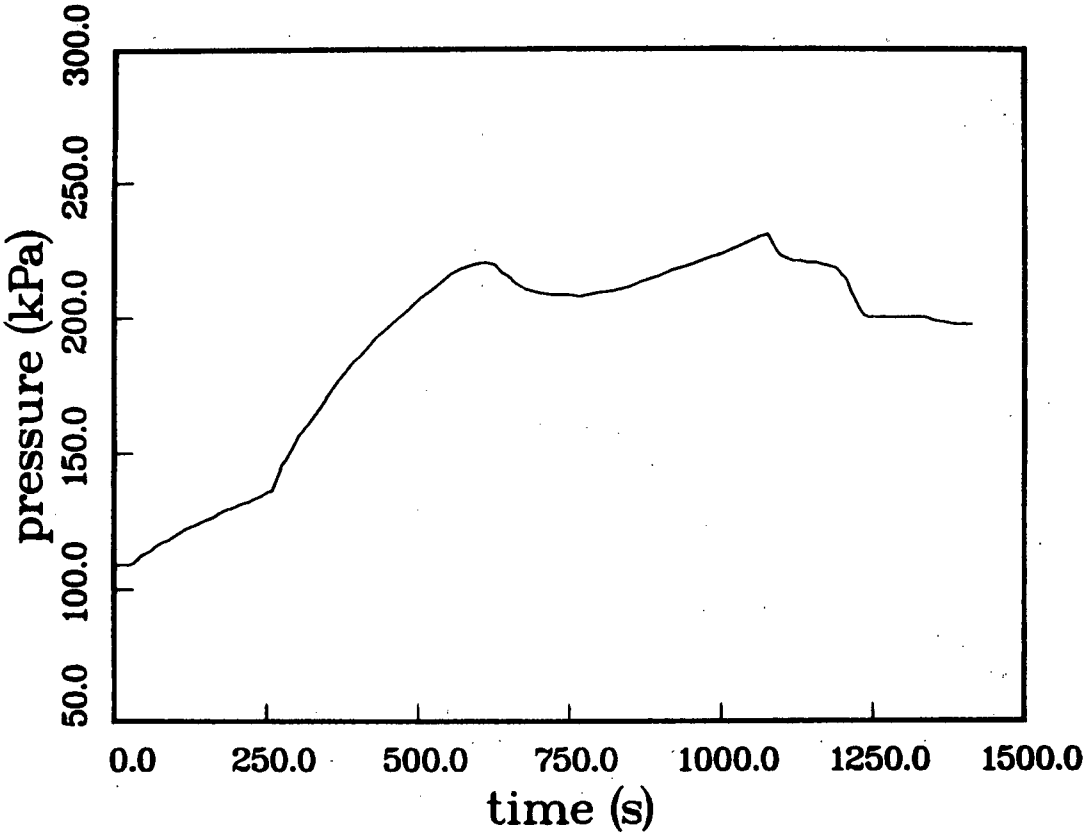

Figure A-13. Test C10, gas pressure P102.

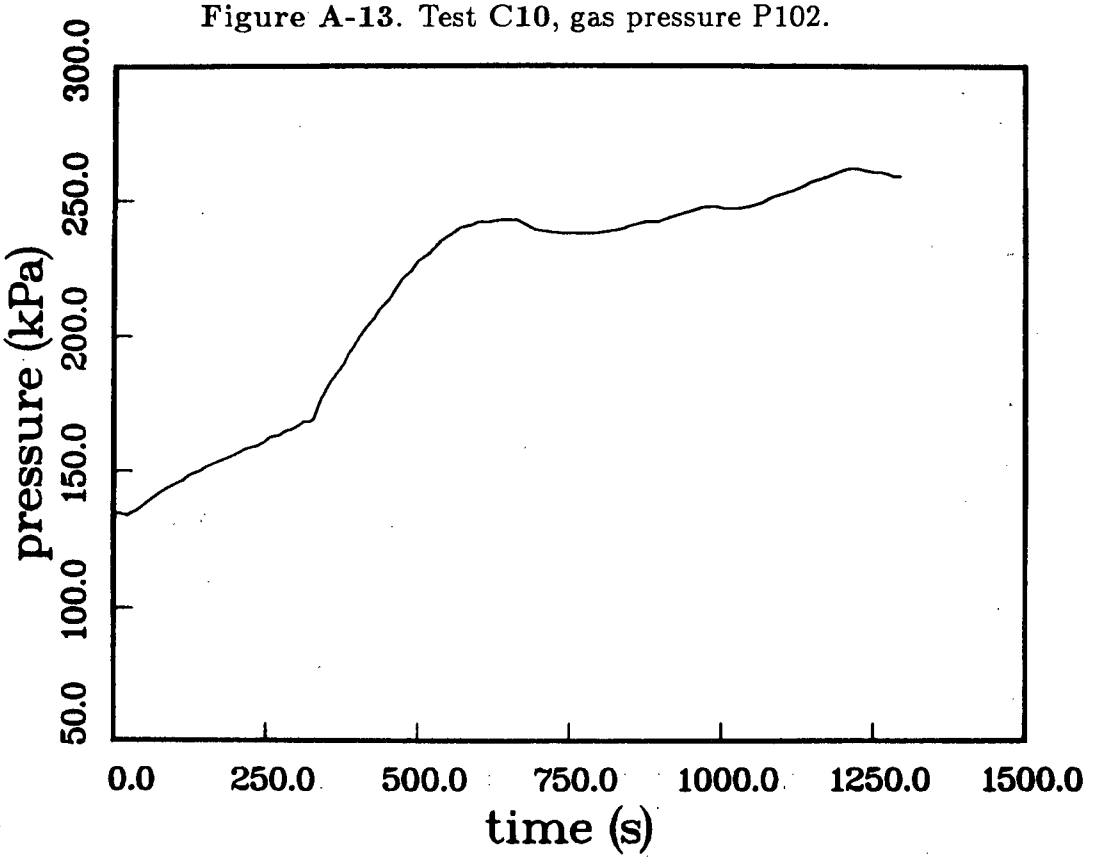

Figure A-14. Test C11, gas pressure P102.

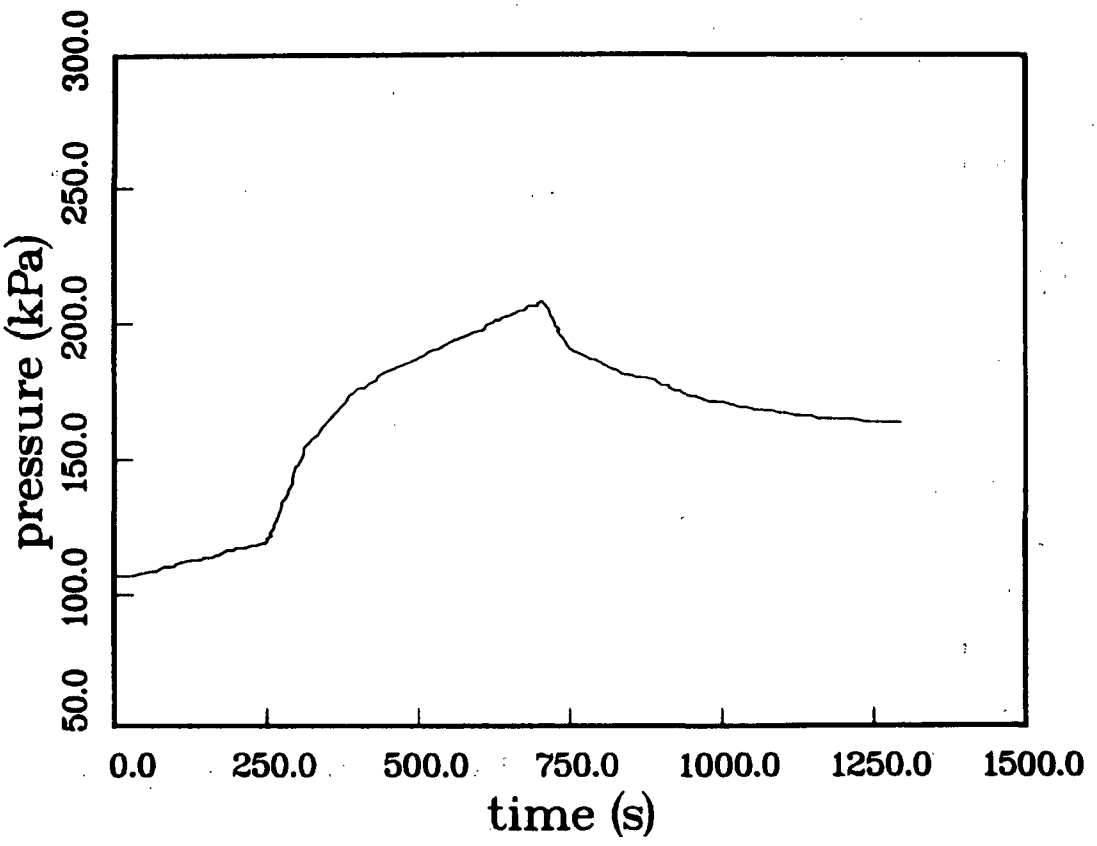

Figure A-15. Test **CN1**, gas pressure P102.

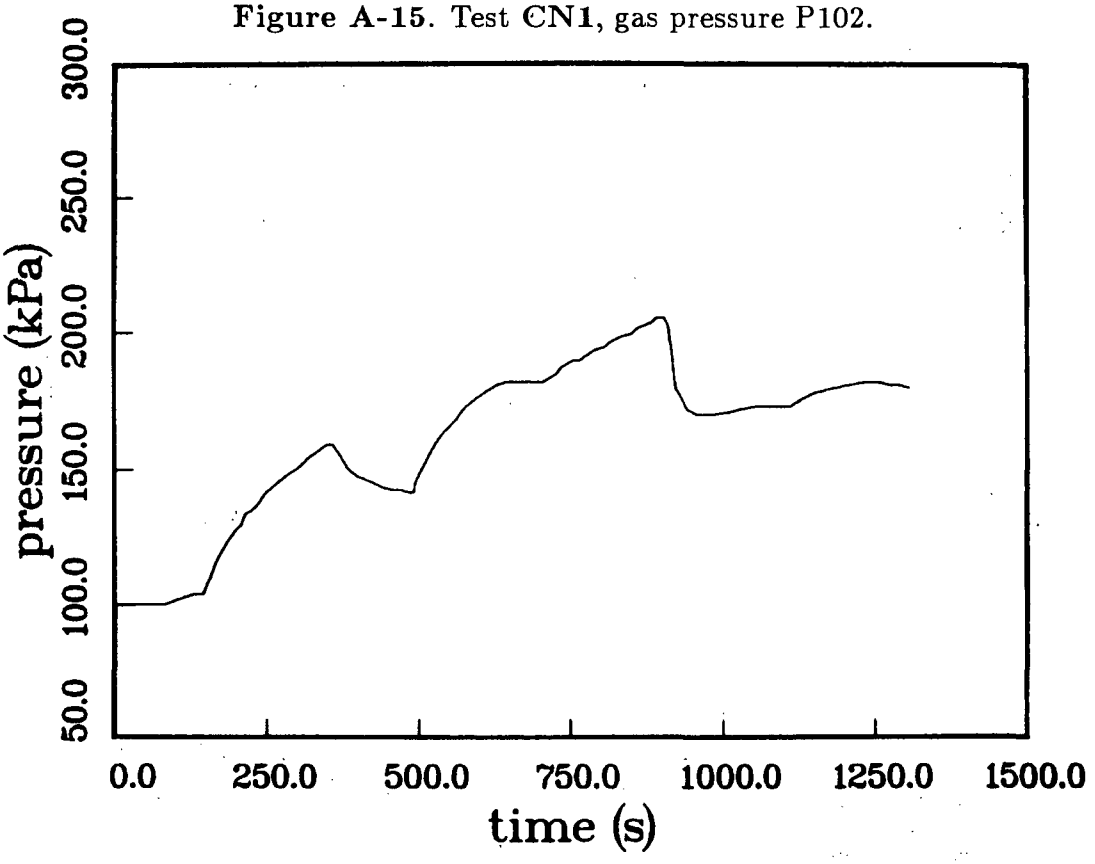

Figure A-16. Test **CN2**, gas pressure P102.

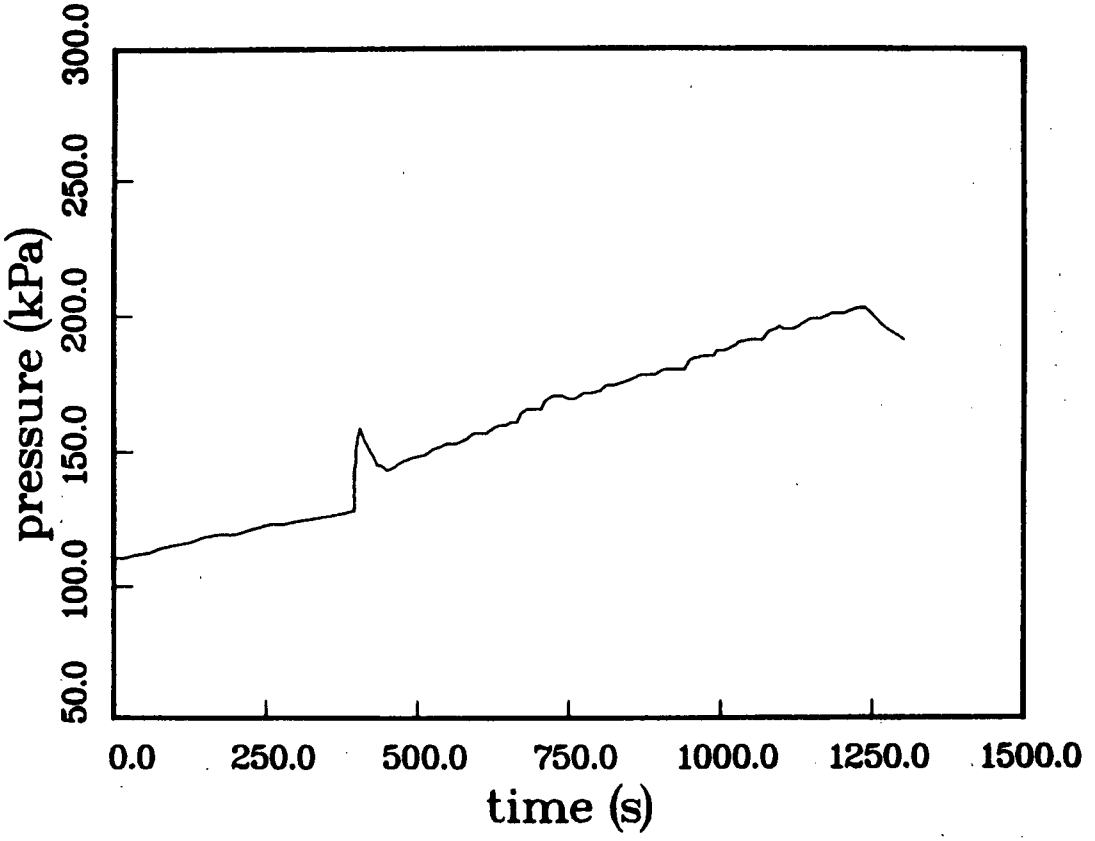

Figure A-17. Test CN3, gas pressure P102.

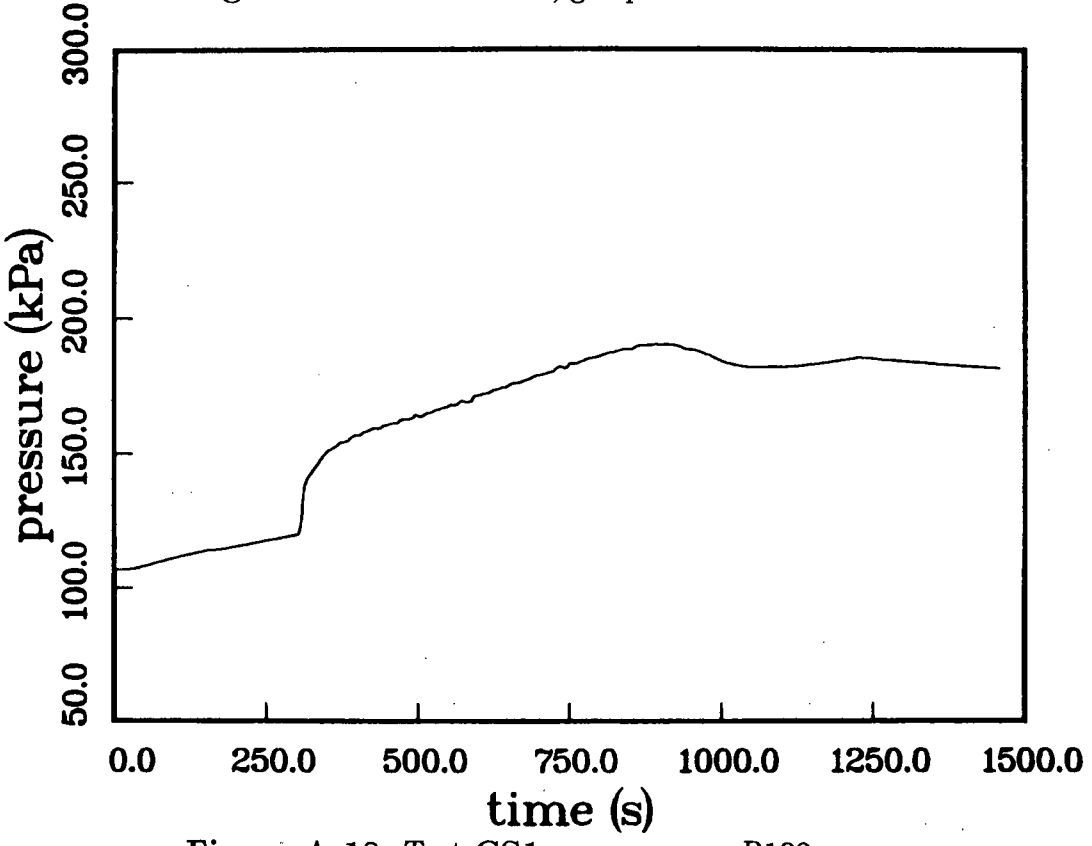

Figure A-18. Test CS1, gas pressure P102.

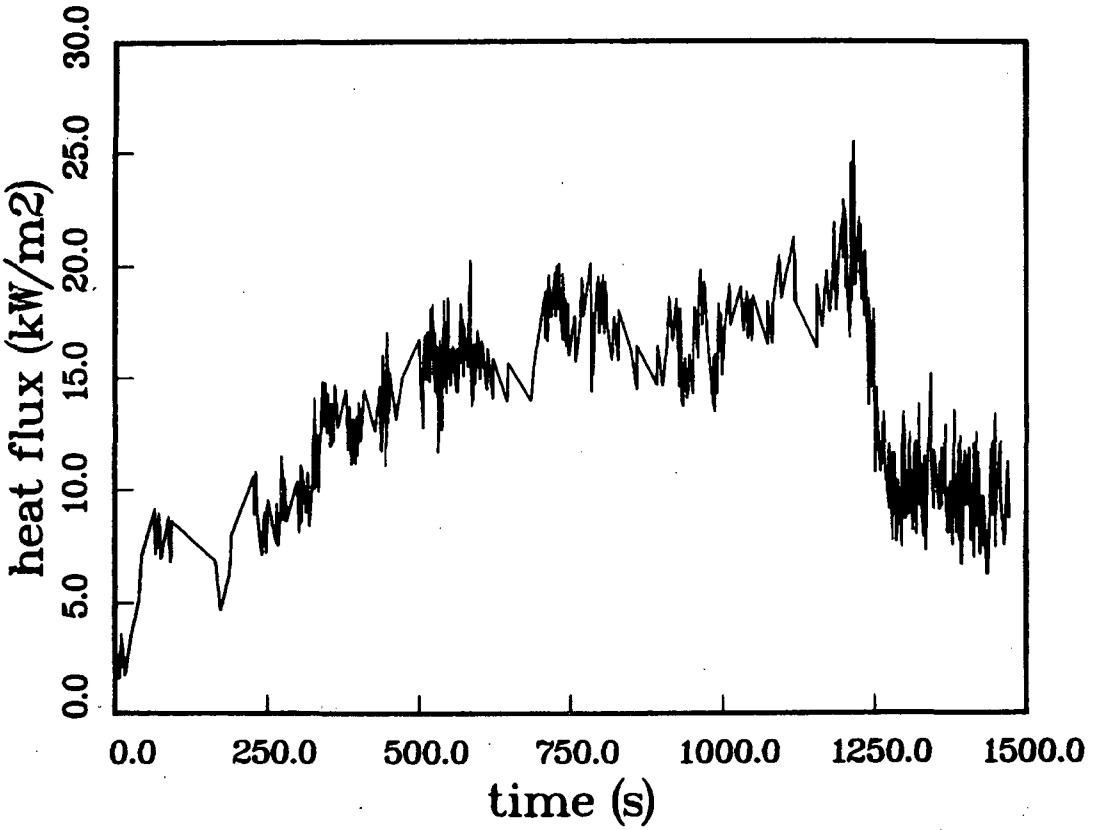

Figure A-19. Test CS1, heat flux H503.

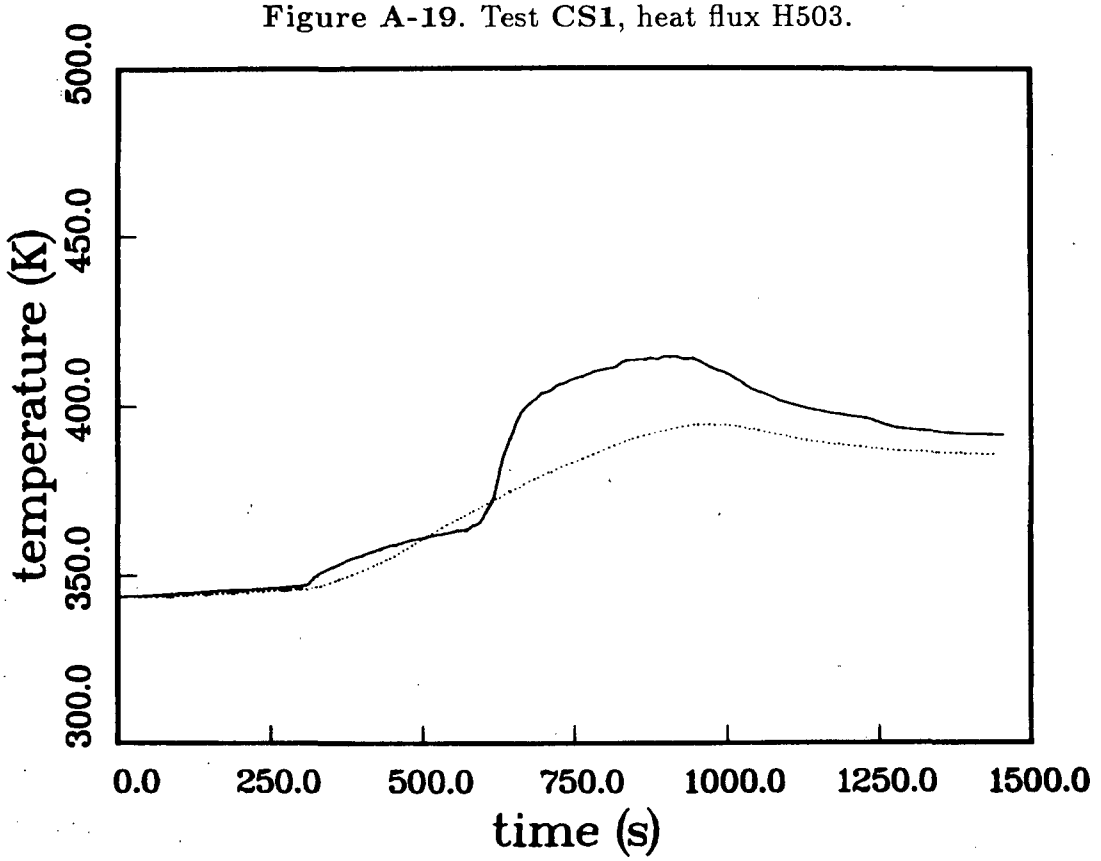

Figure A-20. Test CS1, wall temperatures T120, T121.

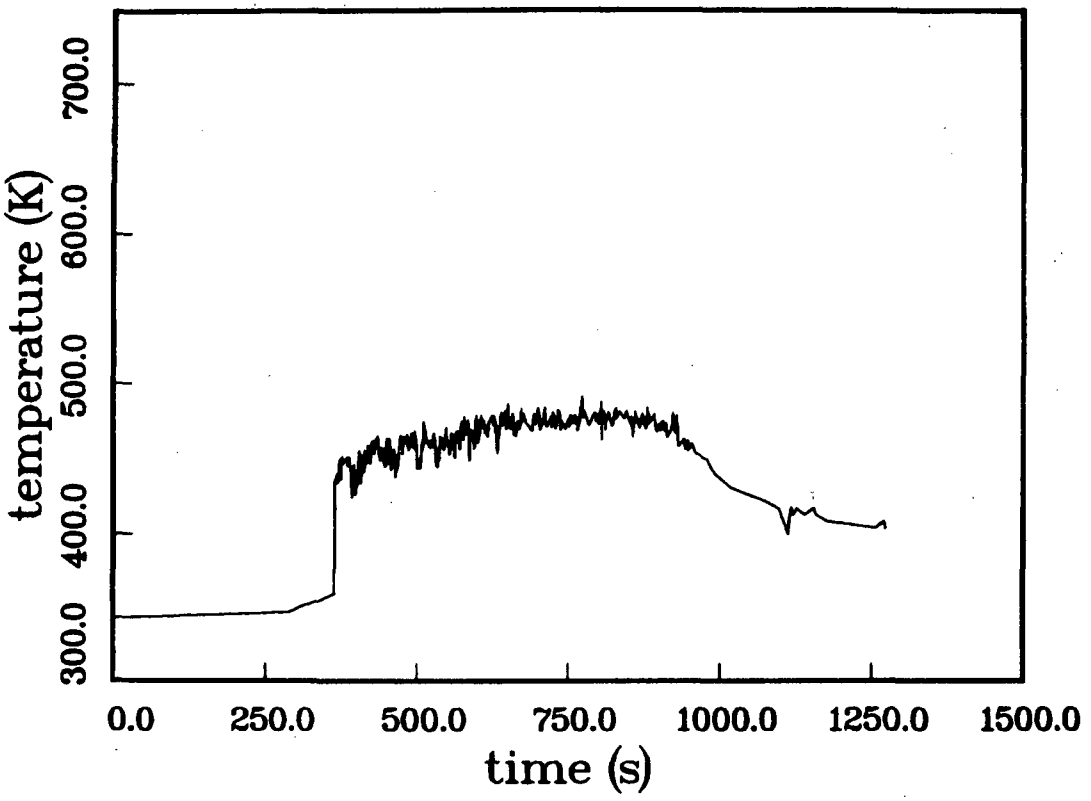

Figure A-21. Test CS1, gas temperature T101.

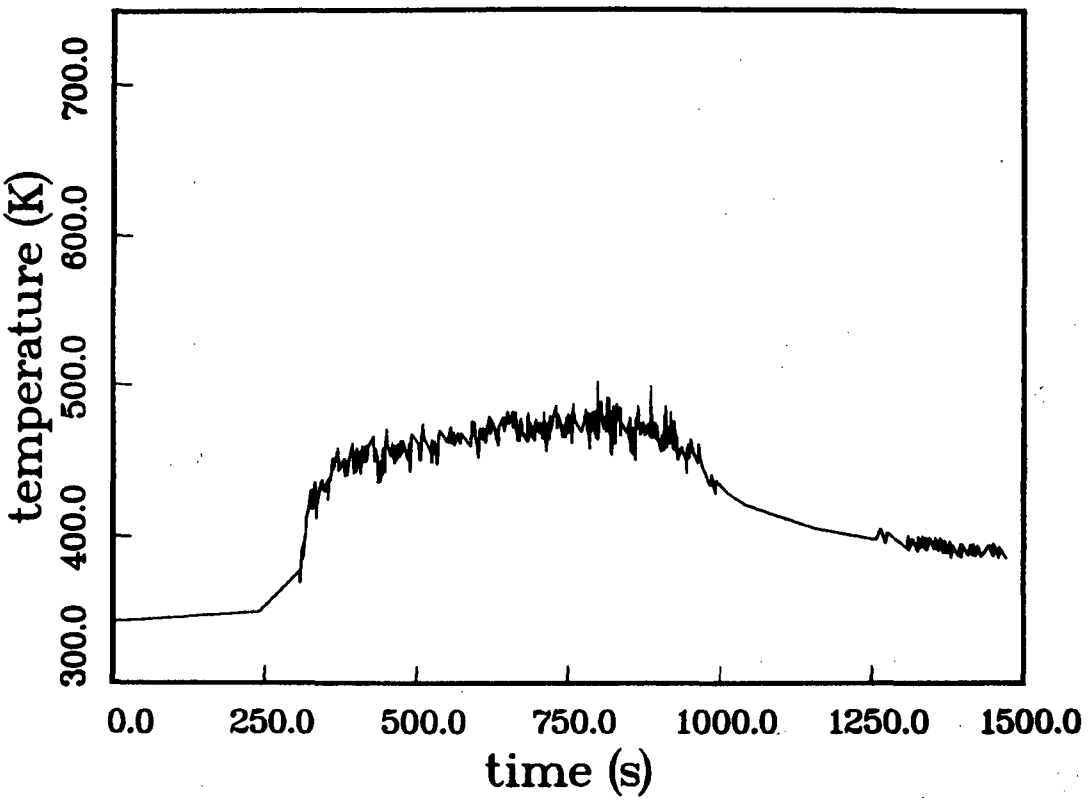

Figure A-22. Test CS1, gas temperature T102.

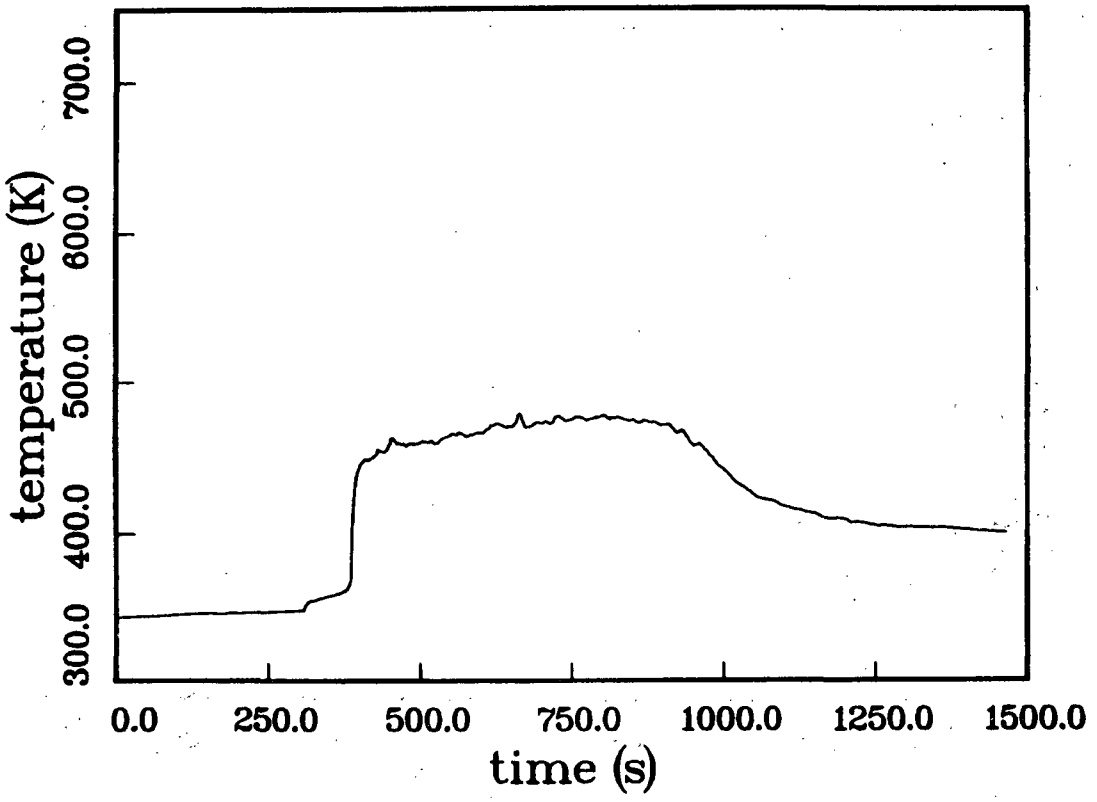

Figure A-23. Test CS1, gas temperature T118.

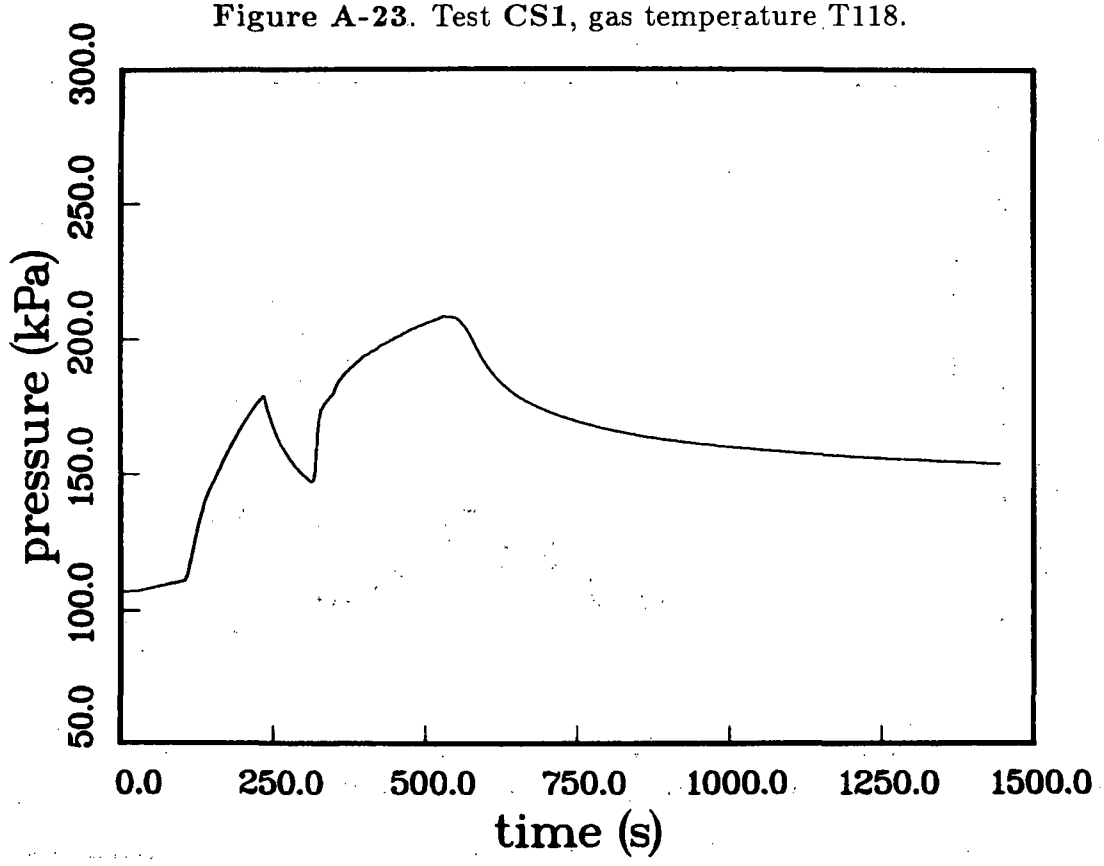

Figure A-24. Test CS2, gas pressure P102.

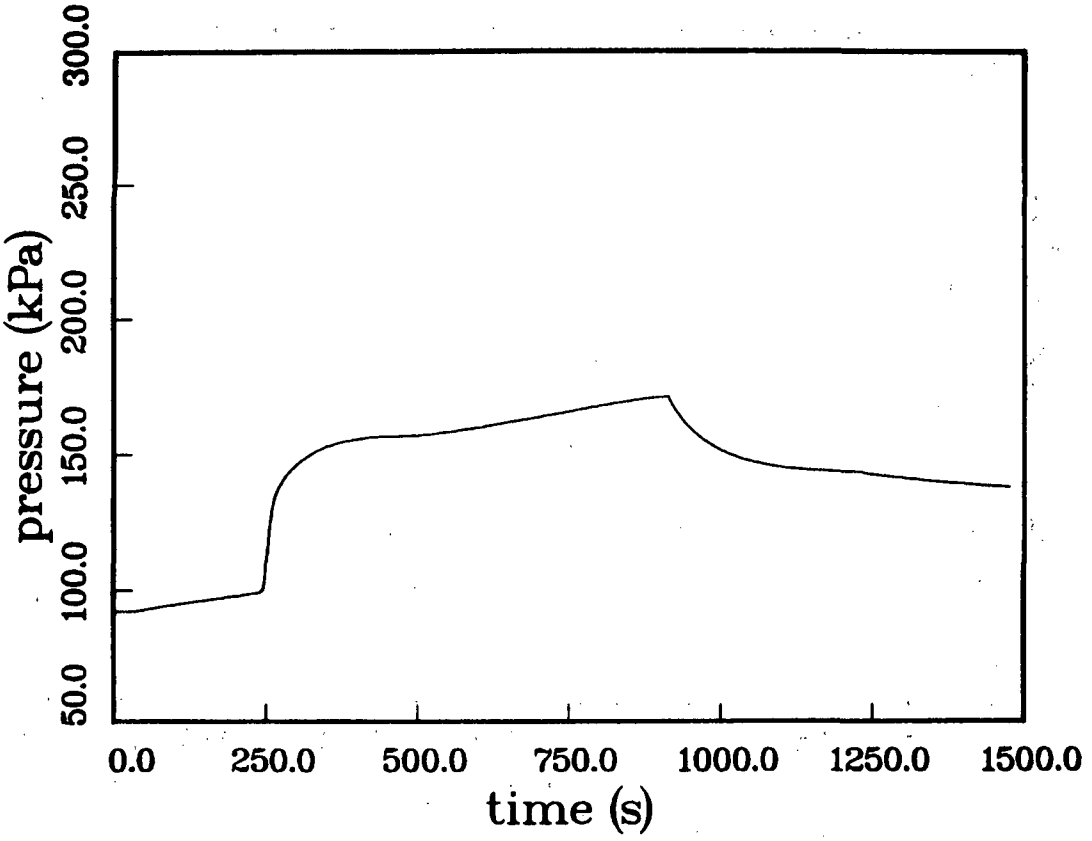

Figure A-25. Test CS5, gas pressure P102.

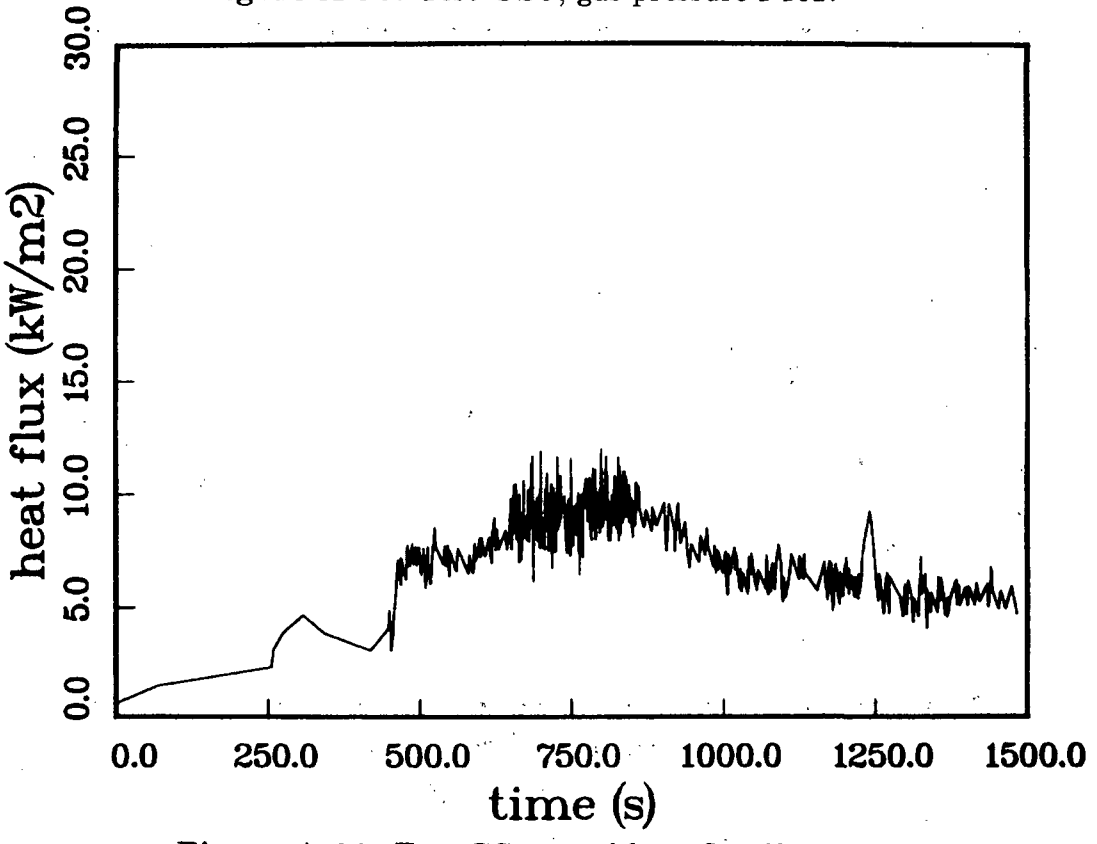

Figure A-26. Test CS5, total heat flux H503.

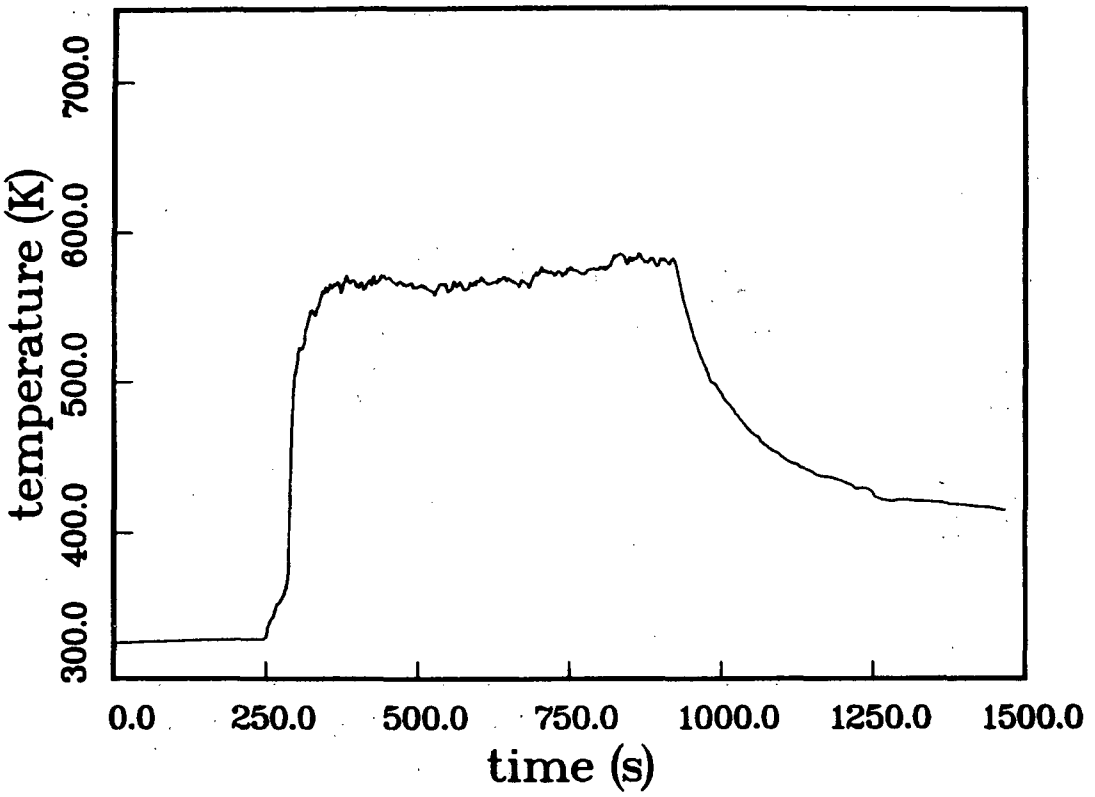

Figure A-27. Test CS5, gas temperature T118.

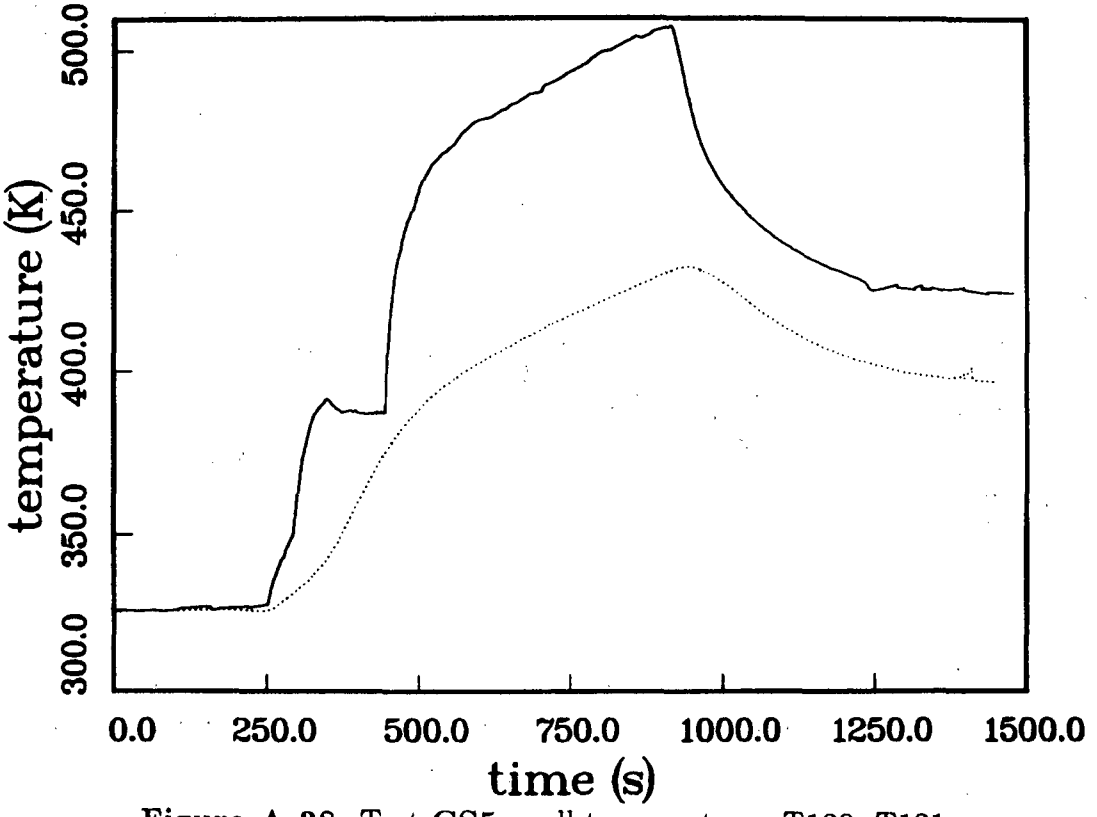

Figure A-28. Test CS5, wall temperatures T120, T121.

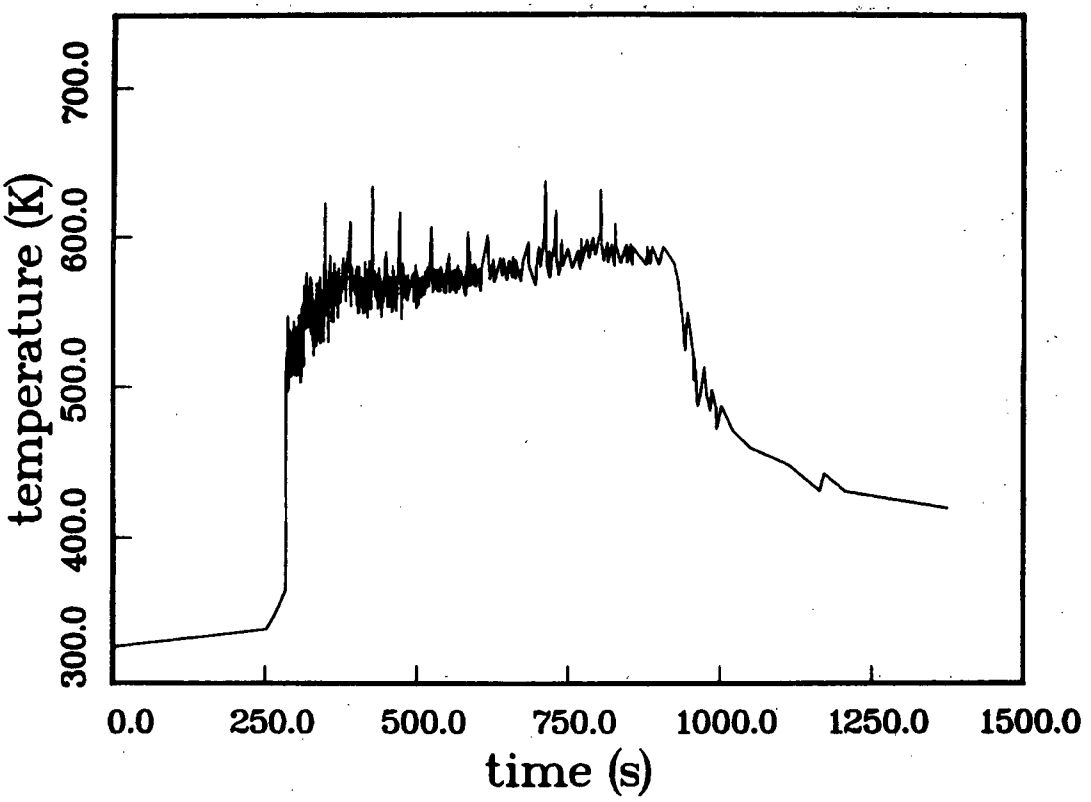

Figure A-29. Test CS5, gas temperature T101.

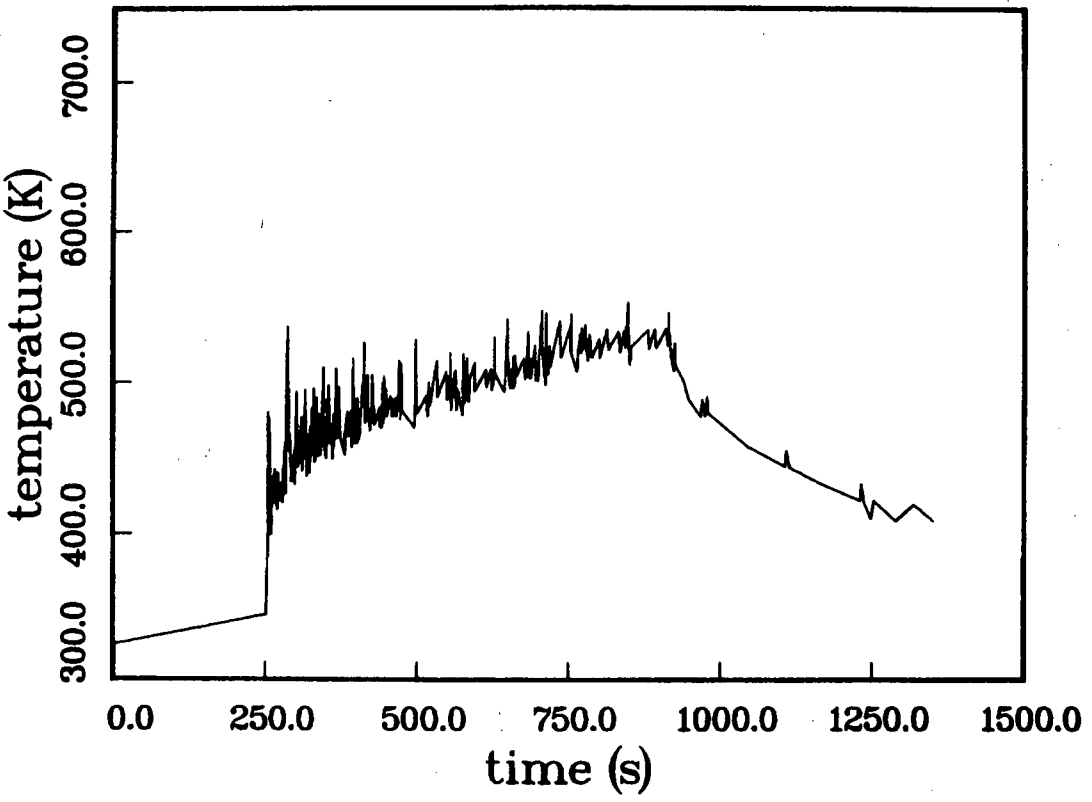

Figure A-30. Test CS5, gas temperature T102.

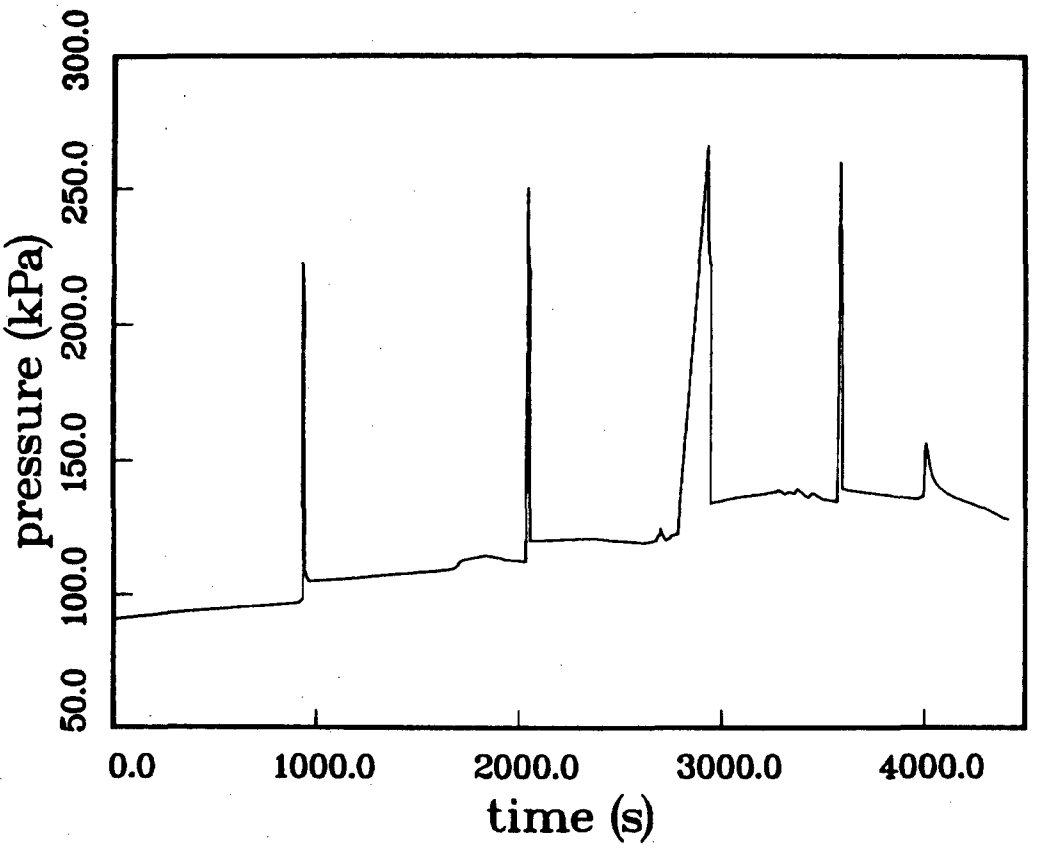

Figure A-31. Test **CS6**, gas pressure P102.

B MOL for Conduction Equation

This appendix describes the solution of the one–dimensional heat transfer problem by the method of lines or MOL. The simple problem that we want to consider is the solution of the conduction equation in a planar geometry of finite extent, *i.e.*, a slab between $x = 0$ and $x = \ell$. To illustrate the method, consider the transient conduction process in a slab with an insulated back boundary and a specified time–dependent flux $q(t)$ at the front surface.

The temperature distribution inside the slab is determined by solving the conduction equation

$$\frac{\partial T}{\partial t} = \kappa \frac{\partial^2 T}{\partial x^2} \qquad (B-1)$$

with boundary conditions

$$-k \left.\frac{\partial T}{\partial x}\right|_{x=o} = q \qquad (B-2)$$

and

$$-k \left.\frac{\partial T}{\partial x}\right|_{x=\ell} = 0. \qquad (B-3)$$

The partial differential equation for the slab temperature is reduced to a set of ordinary differential equations by approximating the spatial derivative by centered second–order differences on a discrete uniform spatial mesh

$$\frac{\partial^2 T_k}{\partial x^2} \approx \frac{T_{k+1} - 2T_k + T_{k-1}}{(\Delta x)^2} \qquad (B-4)$$

where Δx is the mesh spacing. If there are N mesh points then substituting Eq. (20) into the conduction equation results in N ordinary differential equations for the mesh point temperatures T_k.

$$\frac{dT_k}{dt} = \frac{\kappa}{(\Delta x)^2}\left(T_{k+1} - 2T_k + T_{k-1}\right) \qquad (B-5)$$

At the end points, nonphysical mesh points $k = 0$ and $k = N+1$ must be introduced for closure and to implement the boundary conditions. The boundary conditions are incorporated by using the fictitious point outside the domain at each end and evaluating the flux by a centered–difference approximation.

$$\frac{\partial T_k}{\partial x} \approx \frac{T_{k+1} - T_{k-1}}{2\Delta x} \qquad (B-6)$$

Applying this approximation to the insulated end of the slab, $x = \ell$, the boundary condition implies that

$$T_{N+1} = T_{N-1}.$$

At the end of the slab with the specified flux, $x = 0$, the boundary condition implies that

$$T_0 = \frac{2\Delta x}{k} q(t) - T_2$$

Substituting these conditions into the system of equations and setting $\beta = \kappa/(\Delta x)^2$, the final set of equations to be solved are

$$\frac{dT_1}{dt} = \beta \left(\frac{q(t)}{k} - 2T_1 \right)$$

$$\frac{dT_k}{dt} = \beta \left(T_{k+1} - 2T_k + T_{k-1} \right) \quad \text{for} \quad 2 \leq k \leq N-1 \qquad (B-7)$$

$$\frac{dT_N}{dt} = 2\beta \left(T_{N-1} - T_N \right)$$

The reduction of the conduction equation to a set of N ordinary differential equations allows the use of existing subroutine packages to obtain the solution. For parabolic systems such as the heat equation, an implicit predictor–corrector method is the best choice for an algorithm. The time step is automatically determined by the error control procedure within the package. An example of a package that has been successfully used to solve these equations is the routine DEABM of the SLATEC mathematical library.[12]

Distribution:

U. S. Government Printing Office
Receiving Branch (Attn: NRC Stock)
8610 Cherry Lane
Laurel, MD 20707
275 copies for R3

U. S. Bureau of Mines
Pittsburgh Research Center
P. O. Box 18070
Pittsburgh, PA 15236
Attn: M. Hertzberg

U. S. Nuclear Regulatory Commission (7)
Office of Nuclear Regulatory Research
Washington, DC 20555
Attn: G. A. Arlotto
R. T. Curtis
W. S. Farmer
J. T. Larkins
L. C. Shao
K. G. Steyer
P. Worthington

U. S. Nuclear Regulatory Commission (7)
Office of Nuclear Regulatory Research
Washington, DC 20555
Attn: B. S. Burson
C. N. Kelber
C. W. Nilsen
M. Silberberg
J. L. Telford
T. J. Walker
R. W. Wright

U. S. Nuclear Regulatory Commission (5)
Office of Nuclear Reactor Regulation
Washington, DC 20555
Attn: J. K. Long
R. Palla
K. I. Parczewski
G. Quittschreiber
D. D. Yue

U. S. Nuclear Regulatory Commission (7)
Office of Nuclear Reactor Regulation
Washington, DC 20555
Attn: V. Benaroya
W. R. Butler
G. W. Knighton
A. Notafrancesco
T. M. Su
Z. Rosztoczy
C. R. Tinkler

U. S. Department of Energy
Operational Safety Division
Albuquerque Operations Office
P. O. Box 5400
Albuquerque, NM 87185
Attn: J. R. Roeder, Director

Acurex Corporation
485 Clyde Avenue
Mountain View, CA 94042

Applied Sciences Association, Inc.
P. O. Box 2687
Palos Verdes Pen., CA 90274
Attn: D. Swanson

Argonne National Laboratory (4)
9700 South Cass Avenue
Argonne, IL 60439
Attn: H. M. Chung
Dae Cho
R. Anderson
B. Spencer

Astron
2028 Old Middlefield Way
Mountain View, CA 94043
Attn: Ray Torok

Battelle Columbus Laboratory (2)
505 King Avenue
Columbus, OH 43201
Attn: P. Cybulskis
R. Denning

Bechtel Power Corporation
P. O. Box 3965
San Francisco, CA 94119
Attn: R. Tosetti

Bettis Atomic Power Laboratory
P.O. Box 79
W. Miffland, PA 15122
Attn: Kenneth Vogel

Bechtel Power Corporation
15740 Shady Grove Road
Gaithersburg, MD 20877
Attn: D. Ashton

Brookhaven National Laboratory (3)
Upton, NY 11973
Attn: R. A. Bari
T. Pratt
T. Ginsberg

Duke Power Company (2)
P. O. Box 33189
Charlotte, NC 28242
Attn: F. G. Hudson
A. L. Sudduth

EG&G Idaho (2)
Willow Creek Building, W-3
P. O. Box 1625
Idaho Falls, ID 83415
Attn: Server Sadik
R. Hobbins

Electric Power Research Institute (5)
3412 Hillview Avenue
Palo Alto, CA 94303
Attn: J. J. Haugh
B. R. Sehgal
G. Sliter
G. Thomas
R. Vogel

Factory Mutual Research Corporation
P. O. Box 688
Norwood, MA 02062
Attn: R. Zalosh

Fauske & Associates
627 Executive Drive
Willowbrook, IL 60521
Attn: R. Henry

General Electric Company
175 Curtner Avneue
Mail Code N 1C157
San Jose, CA 92125
Attn: K. W. Holtzclaw

General Physics Corporation
1000 Century Plaza
Columbia, MD 21044
Attn: Chester Kupiec

Knolls Atomic Power Laboratory (2)
Box 1072
Schenectady, NY 12309
Attn: R. L. Matthews
A. Kausch

Los Alamos National Laboratory (4)
P. O. Box 1663
Los Alamos, NM 87545
Attn: R. Gido
J. C. Mark
G. Schott
J. Travis

University of Michigan
Department of Aerospace Engineering
Ann Arbor, MI 47109
Attn: Martin Sichel

Mississippi Power & Light
P. O. Box 1640
Jackson, MS 39205
Attn: S. H. Hobbs

Northwestern University
Chemical Engineering Department
Evanston, ILL 60201
Attn: Prof. S. G. Bankoff

Power Authority State of NY (2)
10 Columbus Circle
New York, NY 10019
Attn: R. E. Deem
S. S. Iyer

Dr. Roger Strehlow
505 South Pine Street
Champaign, IL 61820

Thompson Associates
639 Massachusetts Avenue
Third Floor
Cmabridge, MA 02139
Attn: Timothy Woolf

UCLA
Nuclear Energy Laboratory
405 Hilgard Avenue
Los Angeles, CA 90024
Attn: I. Catton

University of California
at Santa Barbara
Chem. & Nuc. Eng. Department
Santa Barbara, CA 93106
Attn: T. G. Theofanous

University of Wisconsin
Nuclear Engineering Department
1500 Johnson Drive
Madison, WI 53706
Attn: M. L. Corradini

Westinghouse Corporation (3)
P. O. Box 355
Pittsburgh, PA 15230
Attn: N. Liparulo
J. Olhoeft
V. Srinivas

Westinghouse Hanford Company (3)
P. O. Box 1970
Richland, WA 99532
Attn: G. R. Bloom
L. Muhlstein
R. D. Peak

Australian Atomic Energy Commission
Private Mail Bag
Sutherland, NSW 2232
AUSTRALIA
Attn: John W. Connolly

Dir. of Research, Science & Educ.
CEC
Rue De La Loi 200
1049 Brussels
BELGIUM
Attn: B. Tolley

AEC, Ltd. (2)
Whiteshell Nuclear Research Est.
Pinawa, Manitoba
CANADA
Attn: D. Liu
H. Tamm

McGill University
315 Querbes
Outremont, Quebec
CANADA H2V 3W1
Attn: John H. S. Lee

ENEA (2)
Rome, ITALY
Attn: P. L. Ficara
G. Petrangeli

Battelle Institut E. V. (2)
Am Roemerhof 35
6000 Frankfurt am Main 90
FEDERAL REPUBLIC OF GERMANY
Attn: Dr. Werner Baukal
Dr. Guenter Lauger

Gesellschaft fur Reaktorsikerheit (2)
(GRS mbH)
8046 Garching
FEDERAL REPUBLIC OF GERMANY
Attn: M. Buerger
H. Unger

Kernforschungszentrum Karlsruhe (2)
Postfach 3640
75 Karlsruhe
FEDERAL REPUBLIC OF GERMANY
Attn: Dr. S. Hagen
Dr. J. P. Hosemann

Kraftwerk Union
Hammerbacherstrasse 12 & 14
Postfach 3220
D-8520 Erlangen 2
FEDERAL REPUBLIC OF GERMANY
Attn: Dr. H. Karwat

Japan Atomic Energy Research Institute
Tokai Research Establishment
Nuclear Safety Research Center Division
of Nuclear Safety Research
Tokai, IBARAKI, 319-11
JAPAN
Attn: Dr. Kunihisa Soda

Rensselaer Polytechnic Institute (10)
Dept. of Mechanical Engineering,
Aeronautical Engineering, & Mechanics
Ricketts 104
Troy, NY 12180-3590
Attn: Dr. J. E. Shepherd

Swedish State Power Board
El-Och Vaermeteknik
SWEDEN
Attn: Eric Ahlstroem

AERE Harwell (2)
Didcot
Oxfordshire OX11 ORA
UNITED KINGDOM
Attn: J. Gittus, AETB
J. R. Matthews, TPD

Berkeley Nuclear Laboratory
Berkeley GL 139PB
Gloucestershire
UNITED KINGDOM
Attn: J. E. Antill

British Nuclear Fuels, Ltd.
Building 396
Springfield Works
Salwick, Preston
Lancs
UNITED KINGDOM
Attn: W. G. Cunliffe

National Nuclear Corp., Ltd.
Cambridge Road
Whetestone, Leicester, LE83LH
UNITED KINGDOM
Attn: R. May

Simon Engineering Laboratory (2)
University of Manchester
M139PL
UNITED KINGDOM
Attn: Prof. W. B. Hall
S. Garnett

UKAEA Safety &
Reliability Directorate (3)
Wigshaw Lane, Culcheth
Warrington WA34NE
Cheshire
UNITED KINGDOM
Attn: J. G. Collier
S. F. Hall
J. H. Gittus

UKAEA AEE Winfrith (3)
Dorchester
Dorset DT2 8DH
UNITED KINGDOM
Attn: A. J. Briggs
R. Potter
A. J. Wickett

University of Pisa (2)
Pisa
ITALY
Attn: Prof. F. Fineschi
M. Carcassi

Internal Distribution:

1131 W. B. Benedick
1500 W. Herrmann
1510 J. W. Nunziato
1512 J. C. Cummings
1512 M. R. Baer
1513 D. W. Larson
1513 S. N. Kempka
1513 A. C. Ratzel
1520 C. W. Peterson
1530 L. W. Davison
1540 W. C. Luth
1550 R. C. Maydew
3141 S. A. Landenberger (5)
3151 W. L. Garner
6400 D. J. McCloskey
6410 N. R. Ortiz
6412 A. L. Camp
6413 E. D. Gorham-Bergeron
6415 F. E. Haskin
6415 S. E. Dingman
6416 R. M. Cranwell
6418 J. E. Kelly
6420 J. V. Walker
6421 P. S. Pickard
6422 D. A. Powers
6423 K. O. Reil
6425 W. J. Camp
6427 M. Berman (5)
6427 D. F. Beck
6427 B. W. Marshall, Jr.
6427 L. S. Nelson
6427 M. P. Sherman
6427 S. E. Slezak
6427 D. Stamps
6427 S. R. Tieszen
6427 C. C. Wong
6427 G. Shaw (15)
6429 K. D. Bergeron
6440 D. A. Dahlgren
6442 W. A. von Riesemann
6447 M. P. Bohn
6447 D. B. King
8024 P. W. Dean
8200 R. J. Detry
8300 P. L. Mattern
8357 R. J. Carling
8400 R. C. Wayne
8523 K. D. Marx
8523 B. R. Sanders

NRC FORM 335 (2-84) NRCM 1102, 3201, 3202

U.S. NUCLEAR REGULATORY COMMISSION

BIBLIOGRAPHIC DATA SHEET

SEE INSTRUCTIONS ON THE REVERSE.

1. REPORT NUMBER (Assigned by TIDC, add Vol. No., if any)

NUREG/CR-4534

2. TITLE AND SUBTITLE

Analysis of Diffusion Flame Tests

3. LEAVE BLANK

4. DATE REPORT COMPLETED

MONTH	YEAR
7	86

5. AUTHOR(S)

Joseph E. Shepherd

6. DATE REPORT ISSUED

MONTH	YEAR
8	87

7. PERFORMING ORGANIZATION NAME AND MAILING ADDRESS (Include Zip Code)

Sandia National Laboratories
Org. 1512
P.O. Box 5800
Albuquerque, NM 87185

8. PROJECT/TASK/WORK UNIT NUMBER

9. FIN OR GRANT NUMBER

A1246, A1336

10. SPONSORING ORGANIZATION NAME AND MAILING ADDRESS (Include Zip Code)

Division of Reactor Accident Analysis
Division of Engineering
Office of Nuclear Regulatory Research
U. S. Nuclear Regulatory Commission
Washington, D.C. 20555

11a. TYPE OF REPORT

Technical

b. PERIOD COVERED (Inclusive dates)

12. SUPPLEMENTARY NOTES

13. ABSTRACT (200 words or less)

This report discusses the results and analysis of hydrogen diffusion flame tests conducted at the Nevada Test Site by EPRI and the U. S. NRC. Those tests were designed to simulate the effects of hydrogen combustion inside a nuclear power plant containment following a degraded-core accident. Test initial conditions and sample data plots are given for 16 tests. Mixing and ignition phenomena are discussed in terms of the source parameters and igniter location. A simple model is developed for simulating the heat transfer and computing convective heat transfer coefficients for experimental pressure measurements. Convective heat transfer coefficients are reported for four tests. The effect of stagnation-point heat transfer is estimated.

14. DOCUMENT ANALYSIS – a. KEYWORDS/DESCRIPTORS

data analysis, continuous injection combustion experiments, diffusion flame, NTS hydrogen dewar

b. IDENTIFIERS/OPEN-ENDED TERMS

15. AVAILABILITY STATEMENT

unlimited

16. SECURITY CLASSIFICATION

(This page)

unclassified

(This report)

unclassified

17. NUMBER OF PAGES

18. PRICE

Org.	Bldg.	Name	Rec'd by	Org.	Bldg.	Name	Rec'd by

Sandia National Laboratories